

Distributed Cooling in Cryogenics with Miniaturized Fluid Circuits

Von der Fakultät Maschinenwesen

der

Technischen Universität Dresden

zur

Erlangung des akademischen Grades

Doktoringenieur (Dr.-Ing.)

angenommene Dissertation

Dipl.-Ing. Grohmann, Steffen
geb. am 21.10.1968 in Dresden

Tag der Einreichung: 16.09.2003

Tag der Verteidigung: 03.02.2004

Gutachter: Prof.Dr.sc.techn. H. Quack
Prof.Dr.-Ing.habil. J. Huhn
Dr.techn. T.O. Niinikoski

Prof.Dr.-Ing.habil. G. Will
Vorsitzender der Promotionskommission

ACKNOWLEDGMENTS

The idea for the Ph.D. thesis presented in this document developed in discussions with Dr.techn. Tapio Niinikoski, co-spokesperson of the CERN RD39 Collaboration, who later became my supervisor in the framework of the *Doctoral Student Programme* at CERN in the years 2000 to 2003. The outcome of the project has been largely influenced by his experience, his support and his advise, for which I would like to express my deep gratitude. I am also most grateful to my supervisor at the Technical University of Dresden, Prof.Dr.sc.techn. Hans Quack, for his suggestions and for fruitful discussions, which had a strong effect on the interpretation of the experimental results. Prof.Dr.-Ing.habil. Jörg Huhn, Technical University of Dresden, I would like to thank for providing a reviewers report. Further, I wish to thank the group leader of the CERN ST-CV group Mats Wilhelmsson for his strong support, and for giving me the opportunity to carry out this thesis in his group.

The project would not have been possible without the enthusiastic support of Dr.rer.nat. habil. Ralf Herzog, head of the Institute für Luft- und Kältetechnik gGmbH (ILK Dresden), and Prof.-Ing. Eberhard Wobst, head of the Refrigeration and Low Temperature Division in the same institute, for which I wish to express my sincere thankfulness. In this context I would also like to thank Dr. Axel Lindner and Dr. Klaus Ehret, both DESY Hamburg, for their interest and for the funding provided by the BMBF research project 05 ESOXL1.

The development of the prototype cryogenic micropump was done in tight collaboration with the company HNP Mikrosysteme GmbH, Germany. I am most grateful for the contributions of Dr. Gerald Vögele, Dr. Thomas Weisener, and Frank Giese, who have invested large efforts and personal commitment. The innovative spirit and the way of cooperation experienced here may be difficult to find in larger companies.

A number of people at CERN were involved in the project. I am very grateful to Jean-Michel Rieubland and to his colleagues for their hospitality and their support in the CERN cryolab. I would also like to thank Dr. Serge Mathot for his support on vacuum brazing and the related design, Noel Mezin for discussions on fabrication technologies, Nicolas Buil and Laurent Deparis for the processing of numerous manufacturing requests, and Michel Bosteels and Pierre Feraudet for their help in constructing the compressor unit. Dr. Jürgen Süß (Danfoss AS) I wish to thank for fruitful discussions on the compressor design and operation. Gudrun Jesse and Rene Matet I would like to thank for the microscopy analyses and the preparation of samples, and Dr. Stefano Sgobba for interesting discussions on materials. My thanks also go to Serge Forel for providing the cleanroom facilities, to Dr. Rene Brun for his support on the ROOT program package,

and to Izabella Wichrowska-Polok for helping with StarCD simulations. I further wish to acknowledge the contributions of Dr. Jean-Marie Le Goff, Dr. Marilena Streit-Bianchi, and Gerd Seefeld (ILK Dresden) for processing the patent proposals, and I want to thank Wolfgang Sussek (ILK Dresden) for the administrative support.

I am very grateful for the contributions of Moritz Kuhn, Thomas Eisel and Georg Nüßle, who participated in the experiments and in the construction of the experimental setup. Special thanks go to Blanca Perea Solano, with whom I have shared a great time of collaboration. I would like to thank her for keeping up the spirits, as well as for contributing the thermal dilatation measurements and the ANSYS simulations.

I very much appreciated to work in the ST-CV group at CERN, and I want to thank all my colleagues for the pleasant atmosphere.

CONTENTS

<i>Acknowledgments</i>	iii
<i>Nomenclature</i>	vii
<i>Abstract</i>	ix
<i>1 Introduction</i>	1
<i>2 Cooling Distribution in Cryogenics</i>	7
2.1 Methods of Cooling Distribution	7
2.2 Fluid Circuits for Convective Cooling	8
2.3 Scaling of Heat Transfer and Flow Parameters	14
2.4 Scope of System Development and Experimental Investigations	16
<i>3 Development of a Cryogenic Micropump</i>	18
3.1 Pumping Principles	18
3.2 Prototype Design of a Cryogenic Micropump	21
3.3 Testing and Experimental Results	26
3.4 Conclusions from the Micropump Development	30
<i>4 Heat Transfer in Microtubes</i>	31
4.1 Theoretical Background and Literature Survey	31
4.2 Experimental Set-up	34
4.3 Concept of Heat Transfer Measurement in Microtubes	36
4.4 Characteristic Dimensions in Rough Tubes	43
4.5 Experimental Program and Data Analysis	47
<i>5 Experimental Results on Heat Transfer in Microtubes</i>	54
5.1 Single-phase Heat Transfer	54
5.2 Conclusions from Single-phase Heat Transfer Measurements	59
5.3 Flow-boiling/Convective Boiling Heat Transfer	60
5.4 Nucleate Boiling	61
5.5 Critical Boiling Conditions	72
5.6 Stability of Flow-boiling	73
5.7 Design of Miniature Evaporator Heat Exchangers	76

<i>6</i>	<i>Design Principles and Applications for Miniaturized Cryogenic Fluid Circuits . .</i>	<i>79</i>
6.1	Circuit Layout with a Cryogenic Micropump	79
6.2	Design of the Compressor Unit	82
6.3	Potential Applications	83
<i>7</i>	<i>Conclusions</i>	<i>87</i>
7.1	Summary	87
7.2	Proposals for Future Research and Development	91
	<i>Appendix</i>	<i>93</i>
<i>A</i>	<i>Algorithms for Scaling of Heat Transfer and Flow Parameters</i>	<i>95</i>
<i>B</i>	<i>Algorithms for Fitting Heat Transfer Data</i>	<i>100</i>
B.1	Fitting Algorithm for Single-phase Heat Transfer Data	100
B.2	Fitting Algorithm for Flow Boiling Heat Transfer Data	104
<i>C</i>	<i>Experimental Data of Heat Transfer Measurements</i>	<i>112</i>
	<i>Bibliography</i>	<i>119</i>

NOMENCLATURE

Symbols

A	m^2	Area
c_p	J/kg K	Specific Heat
d	m	Diameter
g	m/s^2	Acceleration due to Gravity
h	J/kg	Specific Enthalpy
k	$\text{W/m}^2\text{K}$	Overall Heat Transfer Coefficient
L	m	Length
\mathcal{L}	m	Laplace Constant
m	kg	Mass
\dot{m}	kg/s	Mass Flow
\dot{M}	$\text{kg/m}^2\text{s}$	Mass Flux
M	kg/kmol	Molar Mass
n	min^{-1}	Number of Revolutions
p	$\text{Pa}; \text{bar}$	Pressure
P	m	Perimeter
\dot{q}	W/m^2	Heat Flux
\dot{Q}	W	Heat Flow
r	m	Radius
r_d	-	Relative Roughness Parameter
R	K/W	Thermal Resistance
R_a	m	Arithmetic Mean Roughness
T	K	Temperature
u	m/s	Circumferential Velocity
V	m^3	Volume
\dot{V}	m^3/s	Volume Flow
w	m/s	Velocity (Absolute)
x	-	Fluid Quality
Nu	-	Nusselt Number
Pr	-	Prandtl Number
Re	-	Reynolds Number
α	$\text{W/m}^2\text{K}$	Heat Transfer Coefficient
β	-	Linear Dimension Factor
Δ	-	Difference

Symbols (Continued)

ϵ	-	Relative Roughness
η	Pa s	Dynamic Viscosity
λ	W/m K	Thermal Conductivity
ξ	-	Friction Coefficient
ρ	kg/m ³	Density
σ	N/m	Surface Tension

Subscripts

0	Reference Value	lam	At Laminar Flow
2p	Two-phase	n	Normal Boiling Point
∞	Far-field Value	nb	Nucleate Boiling
c	At the Critical Point	onb	Onset of Nucleate Boiling
c	Cross-sectional	out	Outlet
c	Convection	p	At Constant Pressure
crit	Critical Value	rel	Relative
d	Related to the Diameter	s	Saturation
d	Displacement	th	Theoretical
eff	Effective	tr	At the Triple Point
fl	Fluid	turb	At Turbulent Flow
in	Inlet	v	Vapor Phase
l	Liquid Phase	w	At the Wetted Surface
L	Related to the Length	z	At the Location z

Superscripts

*	Reduced
*	Momentary, Preliminary

Abbreviations

ASIC	Application-Specific Integrated Circuit
CFC	Carbon-Fiber Compound
CMOS	Complementary Metal-Oxide Semiconductor
CMS	Compact Muon Solenoid
HTC	Heat Transfer Coefficient
HTSC	High-temperature Superconductor
IHX	Internal Heat Exchanger
LHC	Large Hadron Collider
RF	Radio Frequency
RMS	Root Mean Square
R&D	Research and Development
SEM	Scanning Electron Microscopy
SQUID	Superconducting Quantum Interferometer Device

ABSTRACT

Miniaturized fluid circuits with two-phase flow and active circulation of the coolant enable medium-power cryogenic cooling distribution over large distances with low losses, and yield the best performance and the highest degree of integration in a device. Such circuits are particularly suited to compensate the limitations of regenerative cryocoolers due to the restricted spatial availability of their cooling power. The system development described in this thesis comprises the circuit layout and control, and the design of major circuit components. A prototype cryogenic micropump was developed for circulating the fluid, compatible with cooling powers of about 10 W to 100 W, and capable of producing pressure heads of several bar. A circuit configuration with a room-temperature compressor is a technical alternative, and was built with off-the-shelf components. Extensive experimental investigations on heat transfer in microtubes were conducted with argon at about 120 K, using microtubes of 250 μm and 500 μm inner diameter. The results in single-phase heat transfer revealed no fundamental differences between microtubes and macrotubes. The enhancement of heat transfer compared to conventional correlations was attributed to the increased influence of roughness, and modeled with a newly defined relative roughness parameter. In nucleate boiling heat transfer, an extension of the diameter dependence in the VDI Heat Atlas correlation for vertical tubes was proposed, which becomes effective when the tube diameter is in the range of bubble departure diameters from the wall. Concerning critical boiling conditions, the phenomenon of thermal runaway caused by local dryout is discussed. The stability of evaporative microtube cooling was proven by experiments. Miniaturized cryogenic fluid circuits were developed to meet the requirements of low-temperature tracking detectors in High Energy Physics. The technical solution is independent of the operating temperature, and may prove particularly advantageous for future generations of pixel detectors. Other potential applications are found in the field of superconductor technology, especially in cooling of superconductive magnet bearings, motors, and current limiters.

1 INTRODUCTION

Distributed Cryogenic Cooling with Miniaturized Fluid Circuits

Distributed cooling is required in a number of cryogenic applications, such as low-temperature tracking detectors and superconductive magnet bearings. This thesis describes the development of miniaturized cryogenic¹ fluid circuits, which are especially suited for distributing the cooling power of regenerative cryocoolers. The thesis starts from the conceptual design of such circuits, and it contains the development of major circuit components, as well as extensive experimental investigations related to the heat exchanger design.

Active circulation of the coolant and two-phase heat transfer yield the best performance and the highest degree of integration in a cryogenic device. The fluid can be circulated by either a low-temperature pump, or by a room-temperature compressor. Both technical options are covered in form of a prototype development of a cryogenic micropump, and by the construction of a compressor unit made of standard components.

Experiments on single-phase and flow-boiling heat transfer in microtubes are a fundamental part of the thesis. This includes the development of a suitable measuring concept, studies on the enhancement of surface effects due to roughness, and the verification and extension of conventional heat transfer correlations.

Microtube fluid circuits enable medium-power cryogenic cooling distribution over relatively large distances with low losses, while providing an ideal mechanical and acoustic decoupling of heat sources from the heat sink. The mechanical and the spatial impact on the device are minimized, the temperature gradients are reduced by direct cooling, and additional material normally needed for heat spreading can be eliminated. The need of such systems for cooling of low-temperature tracking detectors gave the motivation to start the project in the framework of the RD39 collaboration at CERN, which is briefly introduced below.

RD39 Collaboration at CERN

CERN, the European Organization for Nuclear Research, is presently constructing the Large Hadron Collider (LHC), which will produce collisions of 7 TeV protons in 4 interaction points at a design luminosity of $10^{34} \text{ cm}^{-2} \text{ s}^{-1}$. The detectors for particle tracking

¹ Cryogenic temperatures are defined somewhat arbitrary as a range of $T \leq 100 \text{ K}$. In this thesis, the term *cryogenic* is used in a wider sense, including also temperatures up to 130 K. This is justified by the use of cryogenic coolants, such as argon, and by the application of cryogenic design principles and technologies.

built around the collision points are exposed each 25 ns to several hundred secondary particles issued from about 20 head-on collisions. After upgrade, the luminosity and the fluence of particles through the trackers will be about 10 times higher. Already at the design luminosity the inner layers of the trackers receive doses in the range of 200 kGy at 10 cm radius from the collision point, entailing serious radiation damage of the silicon sensors and their front-end readout electronics. Radiation induced defects in silicon cause a large temperature-dependent reverse leakage current and an increase of the full-depletion potential, and lead to thermal instability and increased noise unless the temperature is reduced to about -10°C .

The RD39 collaboration [12] develops new detector techniques for trackers, which meet the goals set by the requirements of the LHC after its luminosity upgrade to $10^{35} \text{ cm}^{-2}\text{s}^{-1}$. To reach this luminosity, proton bunches will have to collide with 5 ns to 12.5 ns intervals, yielding 150 to 400 collisions and 1000 to 2400 charged tracks per bunch-crossing interval in the central part of the tracker. Such track and vertex densities require a very fine segmentation of the detectors, which increases the number of output channels. At the same time, the spatial resolution becomes more and more dominated by the material contribution, requiring detector modules of reduced thickness. The speed of the charge signal and of the electronics are also important questions. Major goals of RD39 are therefore:

- to improve the radiation hardness of present state-of-the-art silicon detectors by a factor of 10 or more,
- to develop segmented silicon detectors with faster signal and higher signal-to-noise ratio, and
- to develop low-mass cryogenic systems and low-temperature electronics for experiments in High Energy Physics.

The main improvement in radiation hardness, in terms of the increase of Charge Collection Efficiency (CCE), is obtained by manipulating the charge state of radiation induced deep defect levels and by changing the properties of radiation induced traps, using such tools as the temperature of the detector and the injection of charge by a forward biased junction or by light. The CCE has a broad maximum at a temperature of around 130 K due to the Lazarus effect [11].

Low-temperature operation yields important side benefits. The mobility of the charge carriers grows, speeding up the charge transit time and increasing the current signal. The leakage currents are strongly reduced, which eliminates the noise due to the sensor current. The combination of these, together with the lower noise of CMOS readout circuits at low temperature, yield both faster signals and higher signal-to-noise ratio. The bandwidth and switching speed of CMOS circuits are increased at low temperatures, offering a method to increase the readout speed.

Luminosity Measurement at the LHC

One application for cryogenic tracking detectors developed by RD39 are detectors for luminosity measurement at the LHC. These detectors, to be mounted in so-called Roman Pots, will be used for tracking the protons of forward elastic scattering events. The luminosity-independent measurement of the total cross section proposed in [44] requires the simultaneous measurement of the event rates due to the total and the forward elastic cross sections. This technique is based on the optical theorem and on the extrapolation of the forward elastic scattering amplitude to zero momentum transfer. The accuracy of the experimental total cross section depends critically on how small momentum transfer can be observed, because the functional form of the extrapolation is not known from theory, and because the ratio of the real and the imaginary parts of the amplitude can only be estimated from the data at these very small momentum transfer. This ratio contributes to about 5% to the magnitude of the total cross section, and if it is not measured, it causes a systematic uncertainty of 5% in the results. As the goal of the accuracy is better than 5%, it is obvious that the closest approach to the beam is desirable in the experiment. This requires an edgeless detector, which has no dead material on its side facing the beam, apart from a thin metallic window providing vacuum and RF isolation between the machine and the detector.

The by-product of the luminosity-independent measurement of the total cross section is the measurement of the luminosity itself, and the calibration of the simpler monitoring devices and techniques, which can be operated up to the maximum luminosity of the LHC.

Figure 1.1 shows the locations of Roman Pot stations in about 100 m to 200 m distance from the interaction point 5 (IP5) of the LHC machine, on each downstream beam pipe. The layout of a Roman Pot station is shown in Figure 1.2, consisting of two Roman Pots that are separated by several meters. Each pot has two vertically symmetric vacuum chambers, which can be moved towards the beam. The closest approach of the detectors in the pots to the beam is less than $20\sigma_y$, where σ_y is the vertical gaussian half-height (about 0.1 mm) of the beam at the detector.

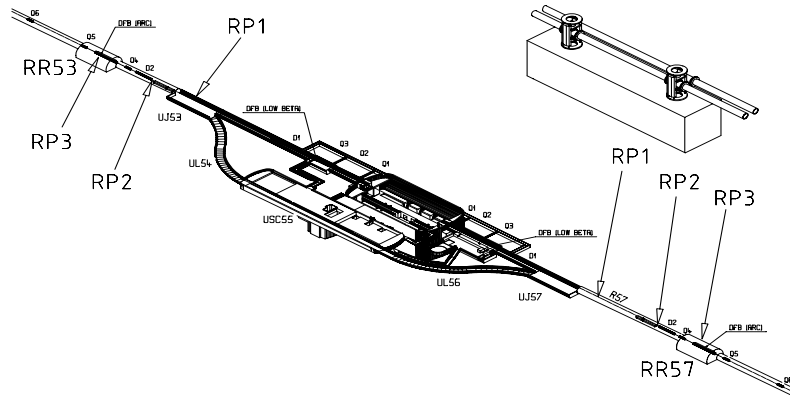


Figure 1.1: Location of Roman Pot Stations for Luminosity Measurement in the LHC [44]

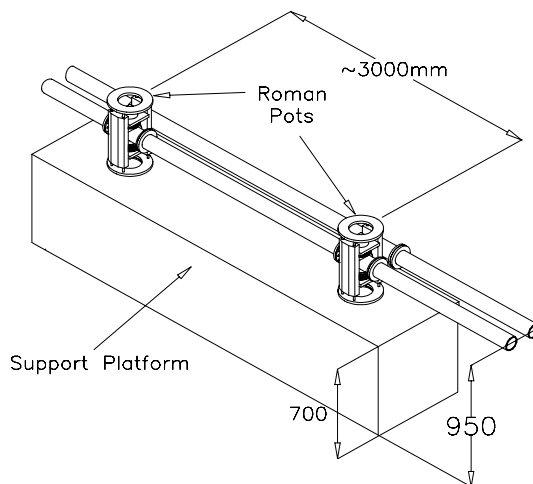


Figure 1.2: Layout of a Roman Pot Station [44]

Edgeless Silicon Microstrip Detector Modules

For such Roman Pots RD39 develops tracker modules with edgeless silicon detectors, which are sensitive to minimum ionizing particles traversing the sensor at its physical edge near the beam. This excludes the use of a guard ring at that edge, and requires very small surface current. The operation of the sensor at about 130 K therefore solves the problem of edge sensitivity, while at the same time providing the best radiation hardness. The electrical and transient current characterization of edgeless silicon detectors diced through the p^+ implant was demonstrated in [50], and the characterization of the edge sensitivity with a high energy beam is discussed in [59].

The beam spot at the detector during forward elastic scattering measurement is about 0.1 mm. A 10 times better spatial resolution requires two or more detector planes with crossed microstrips, and a strip pitch of $50\text{ }\mu\text{m}$ when using analog readout and interpolation based on charge sharing between the strips. A detector surface of $3 \times 3\text{ cm}$ then yields 600 strips per plane. The CMS CMOS chip APV25 is considered for readout, which has been proven to work at cryogenic temperatures [12]. The APV25 is a 128 channel front-end readout ASIC, with each channel dissipating 2.31 mW. The overall heat dissipation of a double-sided module with one vertical and one horizontal strip plane is then about 3 W. The heat dissipation of the sensor itself is negligible due to the small bulk leakage current at 130 K operating temperature.

The mechanical design of a detector half module is shown in Figure 1.3. Silicon is a very good heat spreader at low temperatures, with a thermal conductivity of about 7 W/cm K at 130 K. It is therefore also used as a constructional material, which yields low temperature gradients in the module. Moreover, the ideal match with the silicon sensor in terms of thermal dilatation avoids the generation of thermal stress or deformation during cooldown.

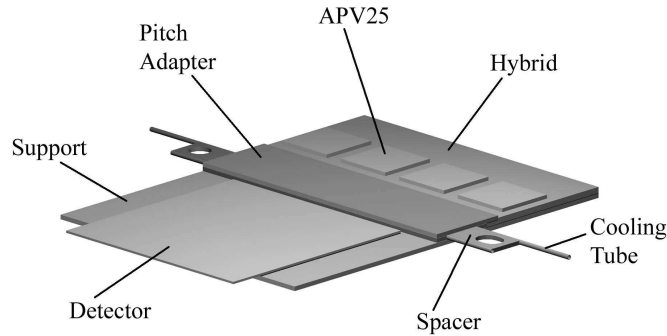


Figure 1.3: Mechanical Design of a Detector Half Module [59]

The silicon detector, the silicon pitch adapter and the aluminum oxide hybrid circuit² are glued with epoxy on the silicon support. A CuNi cooling tube is embedded in a CFC spacer under the pitch adapter. The spacer absorbs thermal stress by elastic deformation of the thin-wall cooling tube, caused by the difference in thermal dilatation between the metallic tube and the silicon. The spacer also contains holes for fixing and aligning the module on a support structure in the Roman Pots. The location of the cooling tube guarantees direct cooling of the readout electronics, which is the main source of heat, and it provides a good thermal isolation of the detector. A detailed description of the thermal and the mechanical design, the assembly, and the testing of the detector modules is given in [59].

Cooling Technologies for Roman Pot Detectors

A detector array in a Roman Pot station consists of minimum 4 double-sided detector modules, each having a heat dissipation of 3 W at 130 K. The location of the Roman Pot stations far from the service cavern in the LHC tunnel clearly excludes a central supply of cooling for all Roman Pot stations. On the other hand, individual cooling of each module with a small cryocooler attached to the vacuum chambers of the Roman Pots is not considered for economical reasons³, and because the precision mechanics to move the Roman Pot chambers close to the beam would not tolerate any vibration.

The concept of one autonomous cooling system for each Roman Pot station was therefore chosen, located on the central platform between the two pots. Taking into account the heat leakage in the transfer lines and in the various vacuum chambers, the overall heat load per cooling system amounts to about 20 W at 130 K.

² The hybrid circuit combines different technologies, such as wire-bonded ASICs, surface-mounted integrated circuits, and other surface-mounted components. It is planned to be processed in silicon in future.

³ The prize of each of 4 small cryocoolers would be as high as the prize of one larger cryocooler for 4 modules.

Figure 1.4 gives an overview on the efficiencies of state-of-the-art cryocoolers at 80 K. It is shown that Stirling and Stirling-type pulse tube cryocoolers have the best efficiency, superior to mixed-gas Joule-Thomson cycles or Turbo-Brayton machines. The latter two recuperative systems have the advantage that a pressure gradient is available to distribute the working fluid to evaporator heat exchangers in the detector modules, whereas regenerative cryocoolers work in a closed gas cycle and provide their cooling power at a relatively small interface. However, Joule-Thomson and Brayton cycles require a large high-pressure for the heat rejection to the ambience, and there are no off-the-shelf compressors in the capacity range of interest. Regenerative cryocoolers, on the other hand, are available in a wide capacity range, and were therefore foreseen to provide the cooling power in the Roman Pot stations.

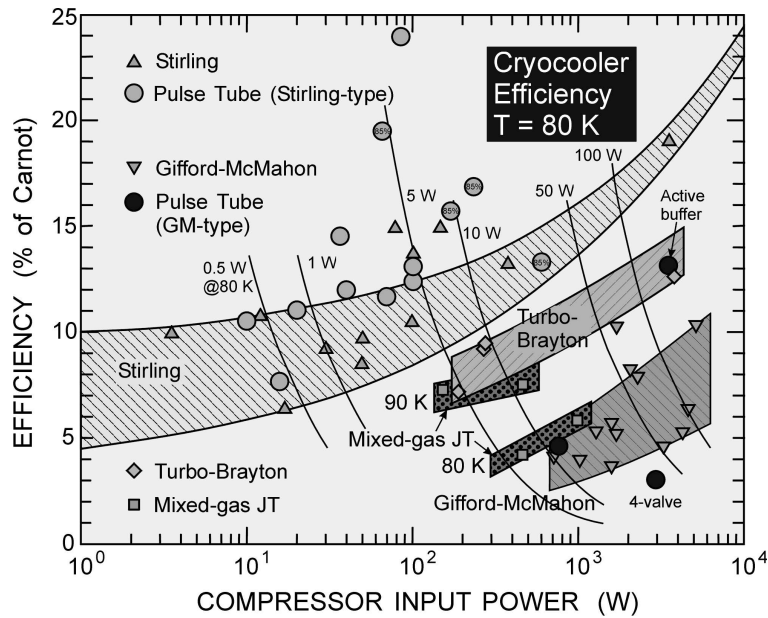


Figure 1.4: Efficiencies of Various Types of Cryocoolers at 80 K [40]

To profit from the efficiency of Stirling and Stirling-type pulse tube cryocoolers, it is essential to have an efficient cooling distribution system between the cold finger of the cryocooler and the heat sources. Miniaturized cryogenic fluid circuits are the key to compensate the limitations of regenerative cryocoolers in terms of cooling distribution in the range of medium cooling power. The development of such circuits is described in the subsequent Sections.

2 COOLING DISTRIBUTION IN CRYOGENICS

2.1 *Methods of Cooling Distribution*

Distributed cooling with high efficiency and low spatial and mechanical impact is required in a number of cryogenic applications. Using regenerative cryocoolers such as Stirling, Gifford-McMahon and pulse tube cryocoolers as a cold source, cooling distribution is needed due to the restricted spatial availability of their cooling power at the small contact surface of the cold finger. In most cryogenic applications it is not possible to attach sensors or electronic devices directly to the cold finger, which is vibrating during operation. It is therefore necessary to establish an efficient thermal connection between the heat source (the application) and the heat sink (the cold finger of the cryocooler). The purpose of such a connection is:

- to absorb the heat load from the application, and to meet its thermal requirements,
- to ensure mechanical and acoustic decoupling of the heat source from the heat sink, and
- to minimize the impact and visibility of the cooling system in the application.

A general overview of cooling distribution methods from the cold finger of a cryocooler is shown in Figure 2.1, grouped by the basic heat transfer principles of conduction, convection and radiation. Thermal radiation usually only contributes to the cooling power of a cryogenic device as a parasitic heat load. Apart from certain space applications, thermal radiation is normally not used for active heat transfer in cooling of cryogenic devices.

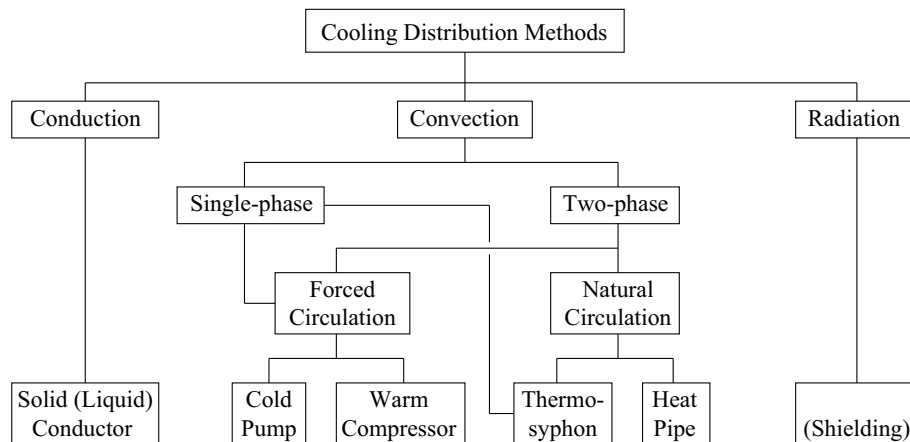


Figure 2.1: Methods of Cooling Distribution

Thermal conduction, on the other hand, is widely applied for cooling of individual sensors. This method, however, is limited to low-power applications of typically $\dot{Q} \leq 1 \text{ W}$, and to short distances between heat sinks and heat sources. This can be illustrated with a simple example:

Transferring the heat load of $\dot{Q} = 1 \text{ W}$ with high-conductivity oxygen-free copper braid of $A_c = 1 \text{ cm}^2$ cross-sectional area and $\lambda = 400 \text{ W/m K}$ thermal conductivity over a distance of $L = 1 \text{ m}$ yields a temperature difference of

$$\Delta T = \dot{Q} \frac{L}{\lambda A_c} = 25 \text{ K} . \quad (2.1)$$

The mass of such a connection is $m = 0.9 \text{ kg}$ (copper density $\rho_{\text{Cu}} = 9 \text{ g/cm}^3$).

A special case of conduction is cooling distribution with superfluid helium, which has an apparent thermal conductivity many orders of magnitude larger than liquids or even high-conductivity solids [81]. Cooling with superfluid helium is not discussed in this document, as it concerns only applications cooled below the λ transition temperature of 2.176 K.

In medium-power cryogenic applications, heat must be absorbed in either comparatively large components, or a number of distant consumers with small heat dissipation is to be cooled with a single heat sink. Typical applications are superconductive magnet bearings, current limiters and power transformers, as well as detector arrays in High Energy Physics. Convective cooling distribution is needed in these applications to limit the temperature gradients and the mass contribution.

2.2 Fluid Circuits for Convective Cooling

Fluid circuits can be designed with single-phase liquid flow or two-phase flow. Pure vapor cooling is not very attractive, as the capacity flux $\dot{C} = \dot{m} \cdot c_p$ and the heat transfer coefficient α are low. Two-phase cooling systems use the latent heat of the working fluid, and therefore require much lower mass flow rates compared to single-phase liquid systems. In addition, temperature profiles in devices are more uniform due to the constant evaporating temperature, and due to very high heat transfer coefficients. Evaporative cooling is therefore the preferable concept.

Table 2.1 gives an overview of cryogenic working fluids suitable for evaporative cooling at temperatures between the triple point temperature T_{tr} and the critical temperature T_c . The specific volume flow rate to absorb 1 W cooling power is in the same range for all the fluids, except for hydrogen and helium that have a lower latent heat.

In general, it is favorable to operate two-phase systems at high pressure. Advantages compared to low-pressure operation are:

- a smaller two-phase pressure drop due to the higher vapor density (lower vapor velocity),
- a smaller (even negligible) saturation temperature shift in heat exchangers caused by the pressure drop, and

- an easier distribution of two-phase flow due to the smaller liquid/vapor density ratio.

In addition, there is a higher margin to control deviating operating conditions (heat load and temperature), which is limited in systems that are designed for operation close to ambient pressure. It is also important to point out that high pressure operation is not equivalent to high risk, as the volume of miniature cryogenic fluid circuits is very small (risk = pressure \times volume).

Table 2.1: Working Fluids for Evaporative Cooling at Low Temperatures

Fluid name	M [g/mol]	T_{tr} [K]	T_c [K]	T_n [K]	\dot{V}_{rel}^1 [ml/min]
Perfluoromethane (CF ₄)	88.01	89.4	227.5	145.2	0.27
Krypton (Kr)	83.80	115.8	209.4	119.8	0.23
Methane (CH ₄)	16.04	90.7	190.6	111.7	0.28
Oxygen (O ₂)	32.00	54.4	154.6	90.2	0.25
Argon (Ar)	39.95	83.8	150.9	87.3	0.27
Nitrogen (N ₂)	28.01	63.2	126.2	77.3	0.37
Neon (Ne)	20.18	24.6	44.4	27.1	0.58
Hydrogen (H ₂)	2.02	13.8	32.9	20.3	1.90
Helium (He)	4.00	2.18	5.20	4.22	23.2

The cooling system development in this work was stimulated by the need of cooling silicon detector arrays, which require sensor temperatures around 130 K. The most suitable working fluid for this application is argon with a system pressure of 15 bar at a fluid saturation temperature of 124 K. Concepts for the circuit layout can be grouped in passive systems with natural circulation, and active systems with forced circulation. Different technical solutions are described below.

Heat Pipe and Thermosiphon

Heat pipes are two-phase fluid systems with natural circulation. The operating principle is illustrated in Figure 2.2a. Heat pipes consist of a sealed pipe filled with a specific working fluid. The heat load is absorbed at the hot end (the evaporator), where the vapor pressure p is high. The cold end (the condenser) is connected to the heat sink (the cryocooler), yielding a lower vapor pressure p_c and a vapor flow from the evaporator to the condenser. A wick installed along the heat pipe returns the condensed liquid back to the evaporator, drawn by capillary forces.

The fluid in thermosiphons is driven by gravity and density differences. Figure 2.2b shows a two-phase² cryogenic thermosiphon that is used for low-noise cooling of HTSC SQUID sensors [9]. The working fluid is liquefied in the condenser, which is connected to the heat

¹ Flow rate per Watt cooling power; saturated liquid at the normal boiling point; dry evaporation.

² In principle, thermosiphons can also be operated with single-phase flow, as in domestic heating systems with natural circulation.

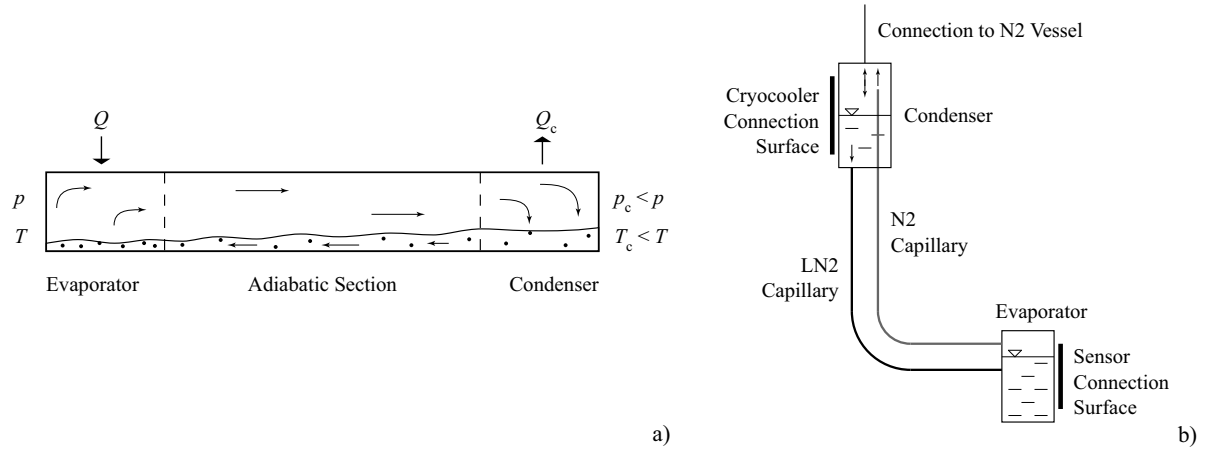


Figure 2.2: Circuit Schemes of Cooling Distribution Systems with Natural Circulation a) Heat Pipe [49]; b) Thermosiphon [9]

sink and installed at a certain height difference above the evaporator. There, the heat load from the sensor is absorbed by the evaporating fluid, and the vapor is driven back to the condenser by the pressure head of the liquid column.

Table 2.2: Advantages and Disadvantages of Fluid Circuits with Natural Circulation

Advantages	Disadvantages
<ul style="list-style-type: none"> - Simple and inexpensive solution. - No moving components. - Very efficient heat transfer when optimized for a specific application. 	<ul style="list-style-type: none"> - No capacity control. - Poor heat transfer during cooldown. - Changed operating conditions are only tolerated within small margins. - The construction height of thermosiphons limits pressure head and orientation.

Advantages and disadvantages of both systems are listed in Table 2.2. Although being an ideal solution in many applications, the cooling power density and flexibility of passive fluid circuits is somewhat limited. Cryogenic applications with a high power density, and which accept only a very low impact of the cooling system therefore require fluid circuits with forced circulation. These circuits can be operated with either single-phase or two-phase flow. The two technical options are circuits with a warm (room-temperature) compressor, and circuits with a cryogenic liquid pump.

Fluid Circuit with a Warm Compressor

The scheme of a fluid circuit with a warm compressor and the thermodynamical cycle in the $\lg(p)$ - h -diagram for argon are shown in Figure 2.3. The circuit consists of a cold part and a warm part, which are connected through an internal heat exchanger (IHX). Room-temperature argon is sucked by the compressor at (1), which performs the work w to compress the fluid to (2). A finned air cooler cools the gas to (3), rejecting the specific heat q_a to ambience. The super-heated gas is then cooled and partially condensed to (4) in the counterflow internal heat exchanger, where heat is exchanged with the return flow from (6) to (1). A condenser/receiver is connected to the heat sink of the system (the cryocooler) that absorbs the specific heat q_c , condensing and sub-cooling the fluid to (5). The specific heat $q = h_6 - h_5$ is absorbed in the evaporator heat exchanger that is integrated in the application.

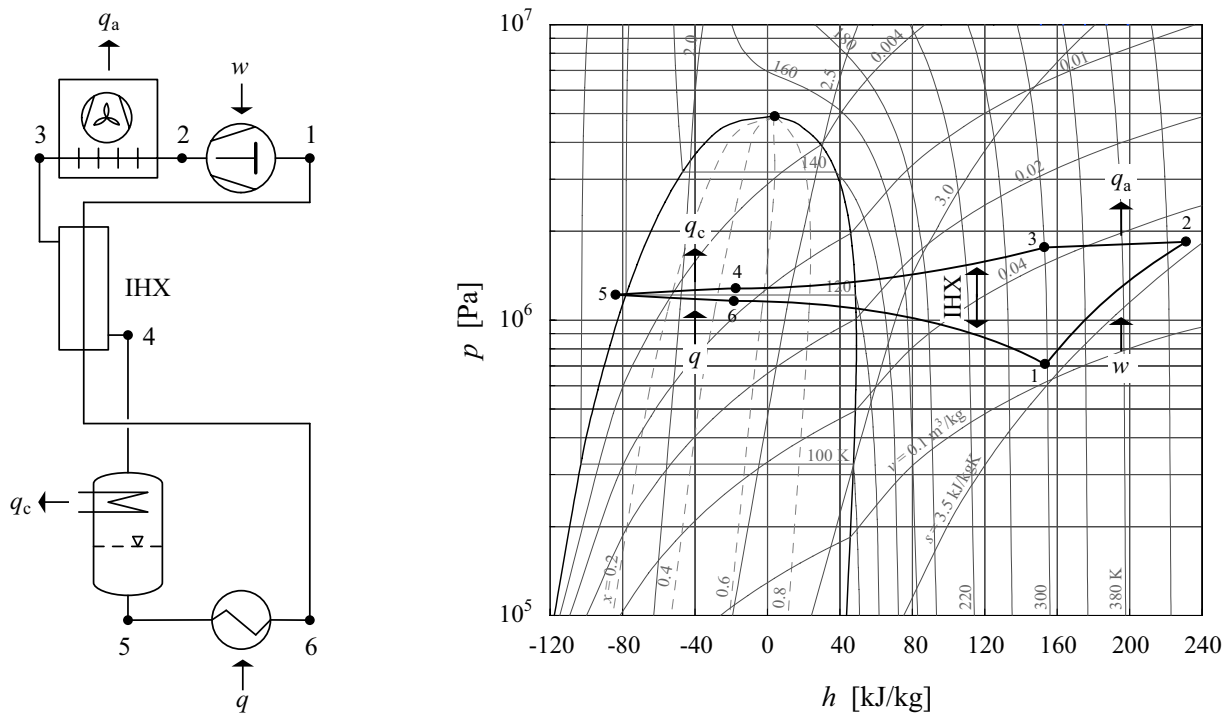


Figure 2.3: Warm Compressor Circuit Scheme and Cycle in the $\lg(p)$ - h -Diagram for Argon

Two points are important for the design and operation of warm compressor circuits:

- The pressure drop in the cold section between (4) and (6) must be sufficiently high. If it is too low, there will hardly be heat exchange between the condenser and the evaporator part of the IHX, as there is no ΔT .
- A certain operating range of minimum and maximum pressure ratio has to be ensured for the compressor. The minimum pressure ratio is determined by the compressor type, and especially by the design of the discharge valve. The maximum pressure ratio is determined by the maximum outlet temperature, which is determined by the

thermal stability of the compressor oil. Design and operation of the compressor unit are discussed in more detail in Section 6.

Table 2.3: Advantages and Disadvantages of Circuits with a Warm Compressor

Advantages	Disadvantages
<ul style="list-style-type: none"> - Inexpensive solution, requiring only off-the-shelf components. - High power density (high degree of miniaturization), as pressure drops of several bar can be accepted in the heat exchangers. 	<ul style="list-style-type: none"> - An efficient filtering system for oil and water removal is needed, which requires maintenance³. - Operation and capacity (mass flow) control are comparatively complicated.

Fluid Circuit with a Cold Pump

The concept of a fluid circuit with a cryogenic liquid pump⁴ is shown in Figure 2.4. The

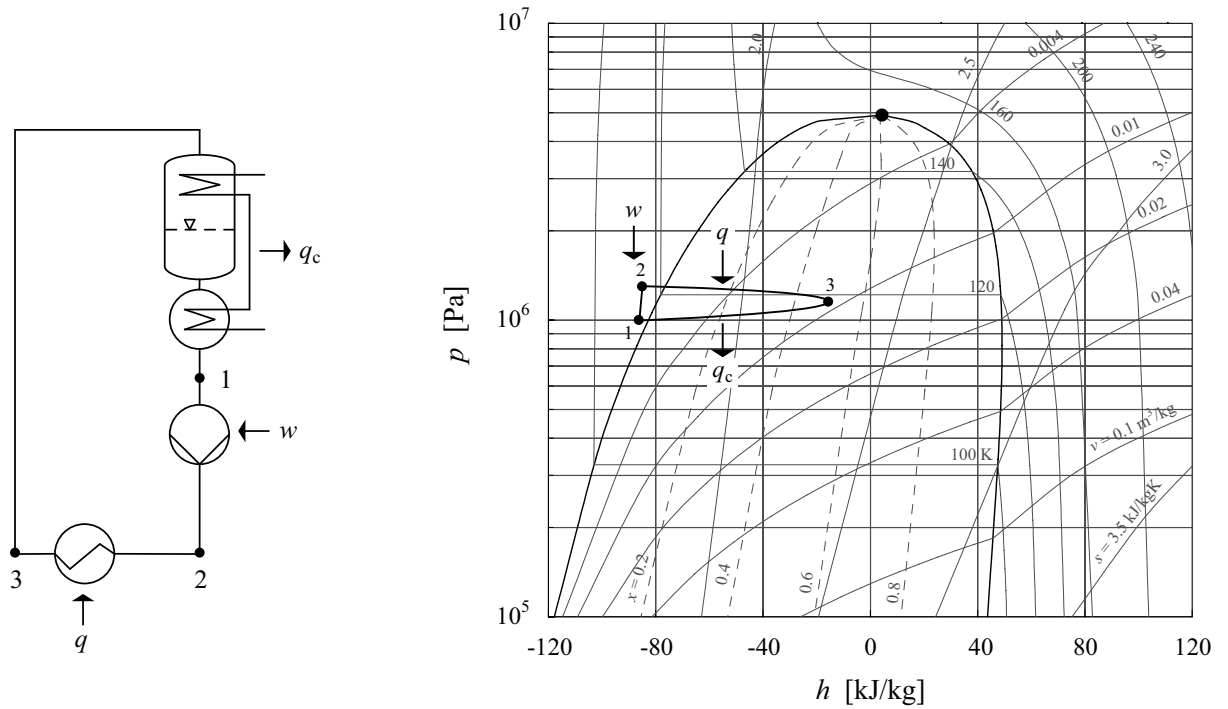


Figure 2.4: Cold Pump Circuit Scheme and Cycle in the $\lg(p)$ - h -Diagram for Argon

³ The filtering system can be designed in such a way that the service interval meets that of the cryocooler.

⁴ The term *cryogenic (liquid) pump* should not be confused with the term *cryopump*, which is a cryocooler used in ultra-high vacuum applications for removing condensable gases.

entire distribution circuit is at low temperature. The pump primes sub-cooled liquid from (1) and generates a pressure head to (2), which is equivalent to the pressure drop in the circuit. The work w to produce the pressure head is negligible compared to the specific heat q that is available for absorbing the heat in the application. The fluid is re-condensed and sub-cooled in a thermal interface that is connected to the heat sink. Flooded systems, which is the equivalent term in refrigeration engineering, are usually operated with a circulation rate of around 2. This means that only 50 % of the liquid is evaporated to avoid dryout conditions in the evaporator.

Table 2.4: Advantages and Disadvantages of Flooded Systems with a Cold Pump

Advantages	Disadvantages
<ul style="list-style-type: none"> - Compact, oil-free and entirely cold circuit. - High power density. - Simple operation and capacity control. 	<ul style="list-style-type: none"> - Cryogenic liquid pumps are not commercially available in the range of medium cooling power.

The specific volume flow rates of less than 1 ml/(min W) listed in Table 2.1 illustrate that cryogenic liquid pumps must be miniaturized. An example of such a development is shown in Figure 2.5, consisting of a miniaturized cold pump body and a room-temperature diaphragm pump. The diaphragm pump generates an oscillating under- and over-pressure in the LN₂ pressure chamber, which makes the suction and pressure ball valves open and close. The performance of this pump is limited by leakage through the ball valves to a pressure head of around 3 m. A new prototype development of a cryogenic micropump was therefore initiated, which is described in Section 3.

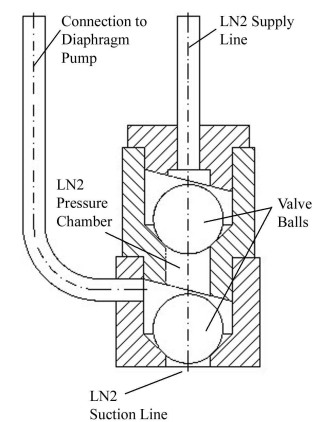
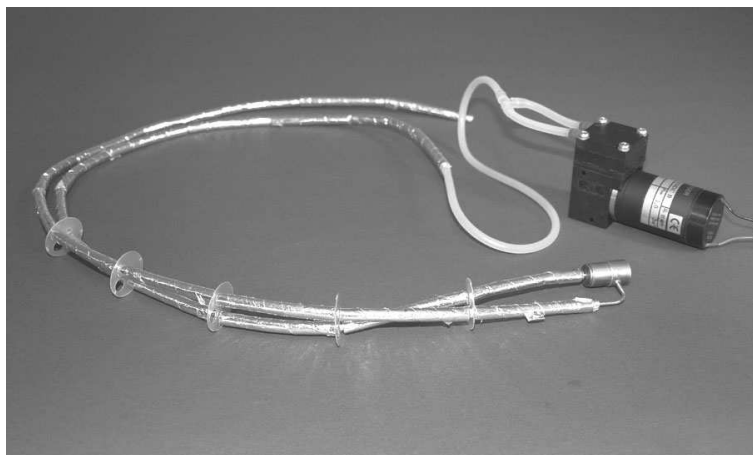


Figure 2.5: Miniaturized Cryogenic Fluid Pump According to [70]

2.3 Scaling of Heat Transfer and Flow Parameters

This Section discusses how heat transfer and flow parameters scale with geometric dimensions. The scaling is related to the linear dimension variable β of a system, representing e. g. the diameter d and the length L of a flow channel in a heat exchanger. Assuming proportional scaling, the area scales with β^2 and the volume with β^3 . It follows directly that the ratio area-to-volume increases for small systems. This is a central issue in miniaturization, since all surface related effects (such as roughness) are enhanced [14]. The enhancements can contribute positively (heat transfer) or negatively (flow friction) to the performance of a system.

When technical solutions are to be compared, one has to fix one or several reference conditions. Various conditions may be relevant depending on the application and the proposed technical solutions. For instance, one may fix

- the power density, i. e. the space in a device occupied by the heat exchanger,
- the pressure drop in a fluid system, when only a certain pressure head is available,
- the temperature difference in heat exchangers, when the cold source temperature is limited,
- or e. g. the heat exchanger surface.

Appendix A contains the algorithms for calculating scaling parameters in single-phase laminar, single-phase turbulent, and two-phase flow. The results for the reference condition of fixed pressure drops are summarized in Table 2.5.

Table 2.5: Scaling of Heat Transfer and Flow Parameters at Constant Pressure Drop

Parameter	Laminar Flow	Smooth Turbulent Flow	Rough ⁵ Turbulent Flow	Two-phase ⁶ Flow
Velocity w	β	$\beta^{1/7}$	1	$\beta^{0.2}$
Reynolds Number Re	β^2	$\beta^{8/7}$	β	$\beta^{1.2}$
Cooling Power \dot{Q}	β^3	$\beta^{15/7}$	β^2	$\beta^{2.2}$
Power Density \dot{Q}/V	1	$\beta^{-6/7}$	β^{-1}	$\beta^{-0.8}$
Heat Flux \dot{Q}/A_w	β	$\beta^{1/7}$	1	$\beta^{0.2}$
Heat Transfer Coefficient α	β^{-1}	$\beta^{-0.6/7}$	$\beta^{-0.2}$	$\beta^{-0.3}$
Temperature Difference \dot{q}/α	β^2	$\beta^{1.6/7}$	$\beta^{0.2}$	$\beta^{0.1}$

The scaling parameters in Table 2.5 can only be evaluated column by column, as there is no quantitative information between different flow regimes. For example, $\beta = 0.5$ in laminar flow relates to a flow channel with half the diameter d and half the length L

⁵ Only valid for a constant relative roughness ϵ .

⁶ Only valid for smooth tubes.

compared to a reference heat exchanger. The mass flow \dot{m} and the cooling power \dot{Q} are eight times smaller at a constant pressure drop, yielding the same power density $\dot{Q}/V = 1$. The heat transfer coefficient α is twice as high, and the temperature difference $\Delta T = \dot{q}/\alpha$ between the fluid and the wall is reduced to 1/4 compared to the reference heat exchanger. In contrast to laminar flow, small turbulent and two-phase systems allow for higher power densities at constant pressure drop compared to large systems operated in the same flow regime. However, absolute and relative roughnesses play important roles, which may yield a reversed behavior in certain cases.

The question whether heat exchangers shall be designed for laminar, turbulent, or two-phase flow depends on how much pressure drop can be afforded. An available pressure head should always be exhausted for heat exchange, favoring turbulent and two-phase flow conditions if pressure drop permits.

Another question in a given application is whether to design a heat exchanger with a single flow path, or with parallel flow channels. If the length L and the cooling power \dot{Q} of the heat exchanger are fixed by geometric constraints and performance requirements of the application, Eq. (A.2) to (A.4) and Eq. (A.10) yield for laminar flow

$$d_n = \sqrt[4]{\frac{d^4}{n}}. \quad (2.2)$$

d_n is the diameter of each of the n parallel channels, and d the diameter of the single flow path.

The plot of Eq. (2.2) in Figure 2.6 illustrates that the potential for reducing the diameter (or heat exchanger thickness) by adding parallel channels at constant power, pressure drop and flow length is limited⁷. The diameter d_n of each of 4 parallel channels can be reduced

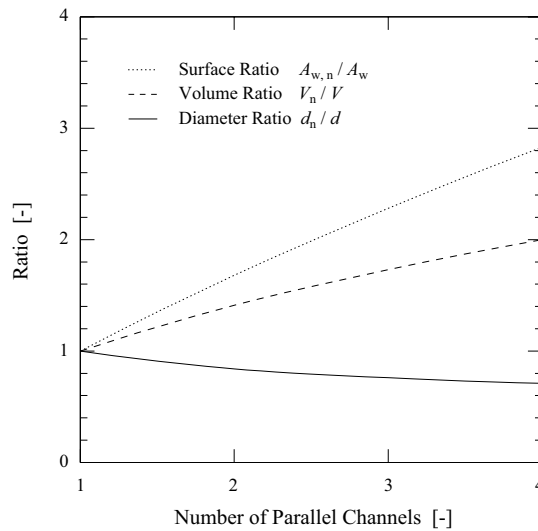


Figure 2.6: Parallel Channels vs. Single Flow Path for \dot{Q} , L , $\Delta p = \text{const.}$ in Laminar Flow

⁷ The application of Eq. (A.14) for smooth turbulent flow yields similar results.

to only 71 % of one single channel. However, the heat exchanger volume is increased by a factor 2, and the heat exchanger surface by a factor 2.83. At the same time, the heat transfer coefficient increases by a factor 1.41 (β^{-1} in Table 2.5). The major advantage of parallel channels is therefore the strong reduction of temperature gradients (in case of single-phase flow), and the possibility of power upgrade at constant channel diameter d . If the diameter is to be reduced in order to increase the power density, higher pressure heads are generally needed. This will usually imply a change of flow regimes from laminar to turbulent flow.

In two-phase flow the reduction of temperature gradients with parallel channels is not evident, as the heat transfer coefficient strongly depends on the heat flux. In addition, maldistribution and flow instabilities are critical issues. This will be discussed in Section 5.6.

2.4 Scope of System Development and Experimental Investigations

The scope of the cooling system development was determined by the requirements of cryogenic tracking detector arrays for High Energy Physics, which are in particular:

- closed circuits with autonomous operation,
- maintenance intervals in the order of 1–2 years,
- cooling power of about 10–100 W at temperatures around 100 K,
- distances between the cold source and the consumers in the range of meters,
- minimized impact and mass contribution of the cooling system in the detectors.

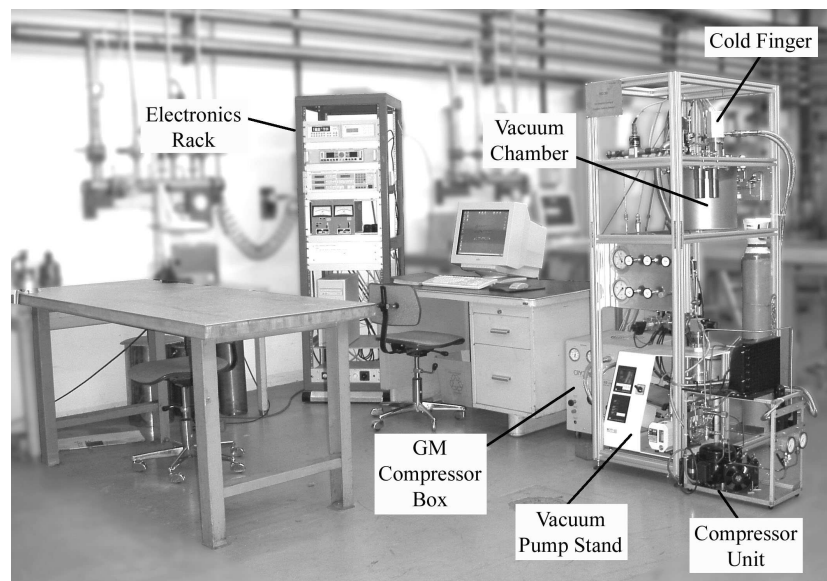


Figure 2.7: Test Stand for Miniature Cryogenic Fluid Circuits

These requirements can be met with miniaturized fluid circuits, which are linked to a central cryocooler, and which are operated with forced circulation. R&D activities in the project were focused on basic design issues, as such circuits are not state-of-the-art. Both alternative technical solutions of a warm compressor and a cold pump were taken into account. The prototype development of a miniature cryogenic fluid pump is explained in Section 3. Fundamental studies on heat transfer in microtubes are discussed in Section 4 and Section 5. The results are essential for the design of evaporator heat exchangers that are integrated in the detector modules. Design issues for the layout of miniaturized cryogenic fluid circuits, the design of circuit components, and the circuit control are covered in Section 6.

Figure 2.7 shows the test stand built to carry out various experiments. The cooling rack contains a vacuum pump stand, a vacuum chamber, a compressor unit, and some gas handling components. The cooling power was provided by a Gifford-McMahon cryocooler. Miniature cryogenic fluid circuits were linked to the cold finger inside the vacuum chamber.

3 DEVELOPMENT OF A CRYOGENIC MICROPUMP

3.1 *Pumping Principles*

Cryogenic micropumps suitable for cooling distribution with miniature cryogenic fluid circuits are not yet commercially available. Basic requirements on their performance are:

- operation at low (cryogenic) temperatures,
- low flow rates in the order of 1–100 ml/min,
- pressure heads in the order of 1–5 bar with low-viscosity fluids,
- low self-heating.

These requirements restrict the choice of pumping principles, which are summarized in Table 3.1.

Volumetric Pumps

Volumetric pumps are divided into reciprocating pumps and multiple-piston rotary pumps. Reciprocating pumps require suction and pressure valves. These valves are certainly the most critical components in miniaturized cryogenic pumps, prone to leakage and malfunction¹.

Advantages of multiple-piston rotary pumps compared to reciprocating pumps are pump cylinders without valves, and rotating pump pistons that eliminate free mass forces and momenta. From the large number of multiple-piston rotary pump types, gear pumps have been successfully miniaturized for various room-temperature applications. Their suitability for cryogenic applications is therefore investigated in more detail.

All volumetric pumps have a pulsating flow, caused by the periodical increase/decrease of displacement volumes. The flow pulsation of gear pumps can be very low, as the pulsation frequency depends on the number of displacement volumes per revolution, and the amplitude on the difference between the largest and the smallest volume.

The theoretical volume flow rate \dot{V}_{th} of gear pumps is given as [2]

$$\dot{V}_{th} = V_d \cdot n , \quad (3.1)$$

¹ The performance of the pump that was shown in Figure 2.5 is mainly limited by the ball valves [70].

Table 3.1: General Classification of Pumps

Group	Volumetric Pumps		Hydrodynamic Pumps	Other Pumps
Type	<ul style="list-style-type: none"> - Reciprocating Pumps <ul style="list-style-type: none"> · Piston Pumps · Diaphragm Pumps 	<ul style="list-style-type: none"> - Multiple-Piston Rotary Pumps <ul style="list-style-type: none"> · Gear Pumps · Screw Pumps · Worm-type Pumps · Vane Pumps · ... 	<ul style="list-style-type: none"> - Centrifugal Pumps - Peripheral Pumps 	<ul style="list-style-type: none"> - Jet Pumps - Air-lift Pumps - Electromagnetic Pumps - ...
Principle	<p>Oscillating piston or diaphragm in a pump cylinder, which is connected to the suction and pressure line through valves that operate synchronously with the reciprocating speed.</p>	<p>One or several rotating rigid or elastic displacement elements that form an increasing displacement volume on the suction side, and a decreasing volume on the pressure side.</p>	<p>Dynamic energy transfer from the rotor to the fluid. Partial transformation of dynamic energy into static energy (pressure) in the downstream diffuser, or in the spiral casing.</p>	<p>No classical features of a pump, such as an oscillating or rotating fluid flow in a closed pump casing.</p>
Features	<ul style="list-style-type: none"> - Small volume flow rates - Generation of high pressure - Pulsation depending on displacer design - Self-priming 		<ul style="list-style-type: none"> - Large volume flow rates - Low pressure head - No pulsation - Usually not self-priming 	<ul style="list-style-type: none"> - Type-dependent

where V_d is the displacement volume per revolution, and n is the number of revolutions. The effective volume flow

$$\dot{V} = \dot{V}_{th} - \sum \dot{V}_{loss} \quad (3.2)$$

is reduced by the sum of internal volume flow losses [2], [63]

$$\sum \dot{V}_{loss} = K_1 \frac{\Delta p}{\eta^{(1-x_1)}} + K_2 n + (K_3 - K_4 \eta^{x_2}) . \quad (3.3)$$

The first term in Eq. (3.3) signifies losses through the gaps between the rotors and the pump casing as a result of differential pressure. The dependence on the number of revolutions is taken into account in the second term. The third term describes reduced engagement losses with increasing viscosity, which are caused by the flank clearance between the rotors. $K_1 \dots K_4$ are geometric parameters, and x_1 and x_2 are parameters that describe the flow conditions in the gaps. These parameters are determined by experiments.

Eq. (3.3) illustrates that the performance of gear pumps is strongly influenced by internal clearances. The minimization of these clearances is particularly important for the operation with low-viscosity fluids, such as all the cryogenic fluids.

Hydrodynamic Pumps

Low-temperature hydrodynamic pumps are used in large-scale cryogenic applications, such as superconductor cooling loops, liquid transfer, aerospace and LNG applications. The smallest pumps on the market have flow rates about three orders of magnitude higher than required in miniature cryogenic fluid circuits [6]. The largest hydrodynamic pumps may be those developed for cryogenic fuel delivery in rockets, e. g. for the Space Shuttle. LH2 pumps for the Ariane 5 launcher have mass flow rates of 55 kg/s at a pressure head of 210 bar [18]. Liquid Helium pumps currently under development for the LHC produce a pressure head of 400 mbar at a mass flow rate of 1.2 kg/s.

The theoretical differential pressure $\Delta p_{th\infty}$ under the conditions of incompressible, frictionless, blade-congruent² flow is given as [2]

$$\Delta p_{th\infty} = \rho (u_2 w_{2u} - u_1 w_{1u}) . \quad (3.4)$$

ρ	fluid density
u	circumferential velocity
w	absolute velocity of the fluid
index 1	directly after entering the blade wheel
index 2	directly before leaving the blade wheel
index u	circumferential component

From Eq. (3.4) it is clear that hydrodynamic pumps are not suited for miniaturization, as the pressure head scales with the blade wheel's diameter and its rotational speed. In addition, the hydraulic efficiency of miniature hydraulic pumps can be expected low as a result of increased surface friction effects.

² Number of blades = ∞ , thickness of blades = 0, flow follows exactly the path of the blades.

Other Pumps

The performance of pumps that are classified in Table 3.1 under the group of *Other Pumps* is often comparable to that of fluid circuits with natural circulation. Although such pumps may work fine in certain cryogenic applications, they do not have the potential for circuits with high cooling power density.

3.2 Prototype Design of a Cryogenic Micropump

The conclusion from Section 3.1 is that multiple-piston rotary pumps, and especially gear pumps, have the best potential to meet the requirements of pumps for miniature cryogenic fluid circuits. Important design issues for such pumps are discussed at the example of a prototype development, which is based on *micro annular gear pumps* that are commercially available for room-temperature applications [33].

Design of the Pump Body

The pumping principle of such micro annular gear pumps is shown in Figure 3.1a. The internal rotor and the annular external rotor have offset axes, and form a system of several pumping chambers. During rotation of the rotors around their individual axes, the pumping chambers increase in volume in the area of the kidney-shaped inlet, and decrease in volume in the kidney-shaped outlet area. Thus, a practically pulse-free volume flow is generated between the suction side and the delivery side at rotor velocities up to $n = 6000 \text{ min}^{-1}$.

The term *micro* relates to the dimensions and the precision of the key components, and

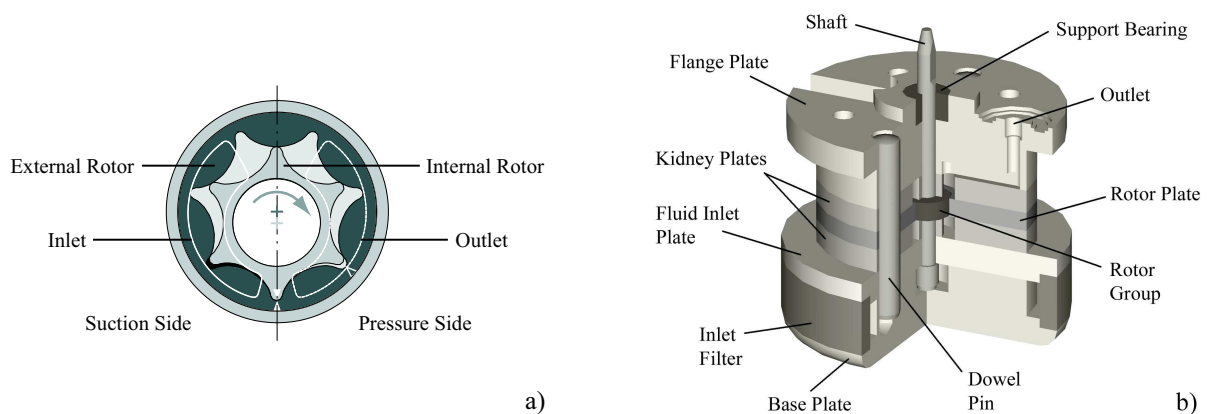


Figure 3.1: a) Principle of Micro Annular Gear Pumps Produced by *HNP Mikrosysteme GmbH* [33]; b) Prototype Design of the Cryogenic Micropump Body

their production by micro-machining technologies. Positional and shape tolerances are within a few microns, which is needed to generate sufficient pressure head in consequence of Eq. (3.3). The *HNP* pump type *mzr-4600* [33] was selected as a basis for the development. Features of this pump are:

- External rotor diameter: $d = 5 \text{ mm}$
- Displacement volume per revolution: $V_d = 12 \mu\text{l}$
- Performance with water at room-temperature: $\Delta p_{\text{max,H}_2\text{O}} = 35 \text{ bar}$ at $\dot{V}_{\text{H}_2\text{O}} = 20 \text{ ml/min}$
- Theoretical performance with Ar at 120 K: $\Delta p_{\text{max,th,Ar}} = 5 \text{ bar}$ at $\dot{V}_{\text{th,Ar}} = 20 \text{ ml/min}$

The prototype design of the cryogenic micropump body is shown in Figure 3.1b. The pump body is made of a precision group that is almost identical with the *HNP* pump *mzr-4600*, and of peripheral components that are specially designed for cryogenic application. The precision group consists of the two rotors, the shaft, two kidney plates and a rotor plate. The two kidney plates sandwich the rotor plate, which serves as bearing for the external rotor. The internal rotor is fixed on the shaft, which is supported by two plain bearings in the kidney plates. The three plates of the precision group are aligned with dowel pins. In the periphery, an inlet sinter filter is clamped between the base plate and the fluid inlet plate. The filtered fluid is collected in a circular duct, and guided to the inlet in the lower kidney plate. The fluid leaves the rotor group on the pressure side opposite the inlet through the outlet opening in the upper kidney plate, which is connected to the outlet duct in the flange plate. The support bearing in the flange plate has a relatively large clearance, serving only to absorb vibrations from the motor drive. The pump body is fixed with bolts to a hermetic pump enclosure, which is shown in Figure 3.4.

An important design issue in the pump body is the shaft bearings, which are exposed to friction and wear. The load on the bearings is generated by dynamic imbalances of the shaft and the internal rotor, and by radial forces due to the differential pressure. The required positional precision of a few microns is achieved with plain bearings. The tribological design of the bearings is a complex topic, involving material science and surface physics³. General rules related to the design of the bearings in the precision group can be summarized as follows [8]:

- Material:
All components of the precision group are made of tungsten carbide (WC) that is sintered with a metallic binder. Such exceptionally hard materials are called *cermets*, and exhibit largely metallic characteristics (increased toughness, ductility and shock resistance compared to pure hard metals). Cermets are often used in cutting tools, drawing dies, forming-die inserts, punches and other tools.
- Friction and Wear:
Friction arises due to adhesion and deformation.
The adhesive component can be reduced by reducing the real area of contact. Hexagonal metals such as WC have a low number of slip planes, a high Young's modulus,

³ A detailed discussion and comprehensive overview on tribology can be found in the book of *Bhushan* [8].

hardness and lack of ductility, and therefore exhibit a low real area of contact. On the other hand, similar metal pairs with non-hexagonal structures exhibit high adhesion and are therefore prone to metallic bonding. Like planes in contact with like planes exhibit higher adhesive bonding forces than dissimilar crystallographic planes of the same material in contact with itself. The lowest adhesion force is found in high atomic density and low free surface energy planes.

The deformation component is a function of the relative hardness, the surface roughness, and the probability of wear particles trapped between the surfaces. Deformation is reduced by reducing the roughness, and by material pairs with equal hardness.

The WC-WC material pair of shaft and bearing with a very high surface quality consequently exhibits low friction and very high wear resistance.

- Lubrication and Interface Cooling:

Similar or dissimilar ceramic or hard metal pairs can be used even under dry sliding conditions, exhibiting moderate friction but maximum wear resistance. The bearings in the pump body are lubricated with the cryogenic fluid. The low shear strength liquid film reduces the adhesive strength between the surfaces, and the S-shaped fluid flow through the the lower and the upper kidney plate absorbs the frictional heat generated in the bearings.

The tribological concept of the pump body design has been proven to work by long-term operation of *HNP* micro annular gear pumps with non-lubricating fluids. There are no fundamental differences between friction and wear at room temperature, and in cryogenic applications.

Another essential design issue is thermal dilatation. The problem is that the thermal contraction of the components during cooldown from 300 K to 100 K exceeds the tolerances and clearances needed for operation. This can only be solved if

- all components are made of the same material, or of materials with similar thermal dilatation,
- and if all components stay in place relative to each other.

A completely homogeneous material composition of the pump body cannot be realized due to practical and economical reasons, as the hardness of WC excludes conventional machining methods. The components in the periphery of the precision group are therefore made of a machinable material. Several alloys were tested to match the thermal dilatation of WC. Selected results of material investigations are shown in Figure 3.2.

The integral thermal dilatation of tungsten carbide between 293 K and 100 K is a factor 4.2 lower compared to 316 stainless steel. INVAR⁴, on the other hand, has almost zero thermal dilatation due to a reversible austenite-martensite transformation. The Fe-Ni alloy found with the closest match to WC has a nickel content of 42 %. Material properties, however, can vary considerably with the exact composition and the thermal treatment.

The match in thermal dilatation between the precision group and the adjacent components is essential to reduce thermal stress and the risk of displacement during cooldown.

⁴ Fe-Ni alloy with 36 % Ni.

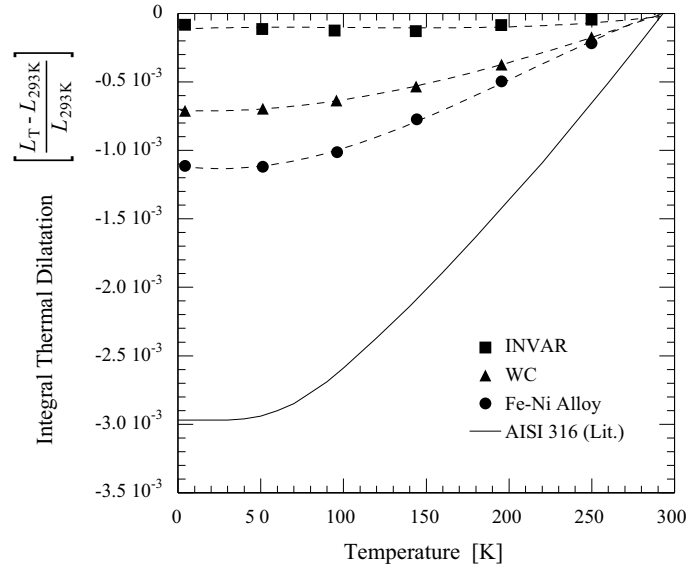


Figure 3.2: Thermal Dilatation of Materials Used in the Micropump Body

Design of the Hermetic Pump Enclosure

The hermetic pump enclosure shown in Figure 3.4 is divided into three sections. The cryogenic section contains the pump body and the fluid connections. The warm section contains the motor drive, and the middle section encloses the extension shaft. The long thin-wall middle section is designed for a maximum heat leak of 0.5 W at a temperature difference of 200 K.

In the cold section, the pump body is fixed with bolts to the lower flange of the shaft enclosure. The inlet port leads directly into the cavity between the pump body and the pump enclosure. The pump and shaft enclosures are sealed with a new type of metallic



Figure 3.3: Images of the Cryogenic Micropump a) Rotor Image [33]; b) Prototype

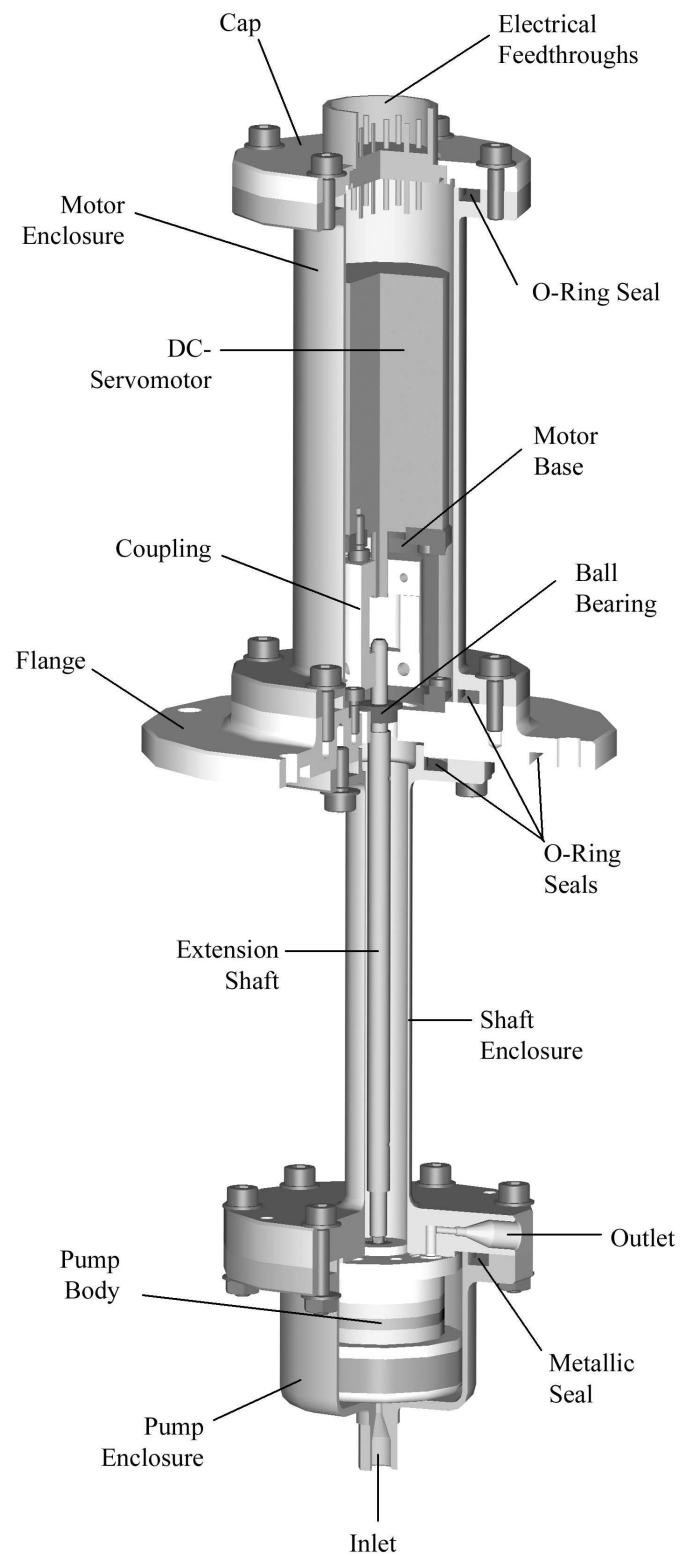


Figure 3.4: Prototype Design of the Cryogenic Micropump

seal⁵. Miniature metallic connectors⁶ for the suction and pressure line were successfully tested for cryogenic application down to 4 K. On the warm side, the shaft enclosure is fixed to a flange, which is used to install the lower part of the cryogenic micropump in a vacuum insulated vessel. A DC-servomotor is fixed on top of the flange through a motor base. A motor enclosure is also connected to the flange and closed with a cap that contains hermetic electrical feedthroughs for the motor drive. All warm flange connections are sealed with elastomer O-ring seals.

The entire internal volume is interconnected and exposed to the suction side pressure. The pump enclosure is heat sunk to the cryocooler. This heat sink is needed to pre-cool the pump body and to condense the fluid before start-up, as well as to absorb the frictional heat from the bearings. During operation the pump body is fully submerged in sub-cooled liquid. A second heat sink is placed at the lower end of the thin-wall shaft enclosure, absorbing the heat leak from the warm section. This heat sink is designed in such a way that the liquid level is higher than the support bearing in the pump body. Above the liquid level the fluid is in gaseous state, and its temperature rises upwards. Around the motor the gaseous working fluid transports the heat losses from the motor to the motor enclosure. The pump enclosure is designed for a maximum operating pressure of 25 bar.

The radial and angular alignment of the pump body, the shaft enclosure, the flange, the motor base and the motor is ensured by precision fits. The extension shaft is form-interlocked with the shaft of the pump body, and connected to the motor through a flexible beam coupling. The extension shaft is supported by a ball bearing in the flange.

3.3 Testing and Experimental Results

Experimental Set-up

The circuit layout for testing the cryogenic micropump is shown in Figure 3.5. The circuit is installed in a vacuum chamber that is operated under 10^{-6} mbar insulating vacuum. The working fluid is circulated in a closed loop, designed for a maximum operating pressure of 25 bar. A thermal interface is attached to the cold finger of a cryocooler, producing sub-cooled liquid⁷. The sub-cooled liquid is primed by the micropump and circulated in the loop. Due to the lack of a low-temperature flowmeter, the mass flow is warmed up in an internal heat exchanger and measured in the gaseous state at room temperature. A metering valve is used to regulate the differential pressure in the circuit. The instrumentation is identical with the one explained in Section 4.2.

⁵ Ultra-FlexTM seals produced by *Garlock* require a fixation momentum of only 20 N/mm, which is similar to that of Indium seals [21].

⁶ Ferrule-type connectors with a knife-like design similar to the principle of cryogenic metal seals, normally used in high-pressure liquid chromatography [77].

⁷ Design and operation of the thermal interface is explained in Section 4.2.

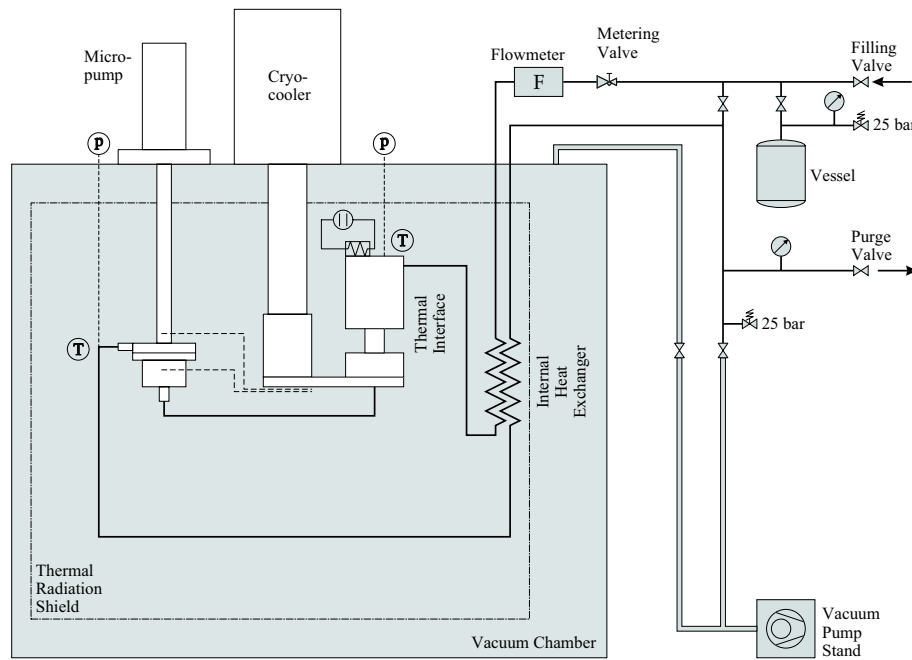


Figure 3.5: Circuit Layout for Testing the Cryogenic Micropump

Performance Tests

The experimental results shown in Figure 3.6 and Figure 3.7 were obtained with a first prototype. Differences compared to the design of the prototype presented in Section 3.2 will be discussed at the end of this Section.

Figure 3.6a shows performance data with argon at a saturation temperature of 110 K with around 5 K sub-cooling. Data are recorded in a time interval of 10 s. The pressure head reaches from about 600 mbar at a pump speed of 2000 min^{-1} to almost 3 bar at a pump speed of 6000 min^{-1} . The slight variations of the pressure head at constant pump speeds result from manipulating the metering valve in order to keep the flow rate around 100 mg/s (5.2 ml/min). The self-heating data shown in Figure 3.6b represent the shaft power calculated from the measured motor current. The data are somewhat conservative as part of the shaft power goes into the room-temperature ball bearing. Although the measurement is not very accurate and taking into account a potential for further reduction of internal friction, the results show that the cryogenic micropump is well suited for systems with cooling powers of $\geq 10 \text{ W}$.

The data in Figure 3.7a show the micropump operation over a period of 5 h. Data are recorded in a time interval of 5 s at a fluid temperature of 95 K. A low uniform motor current of $180 \pm 20 \text{ mA}$ indicates an undisturbed operation. On the other hand, Figure 3.7b contains data where the micropump was contaminated with solid particles. The current peaks signify short blockages of the rotors. After about 3 h of operation the micropump failed completely due to the jamming of the rotors. These results gave reason for reviewing the micropump design and integrating an inlet filter.

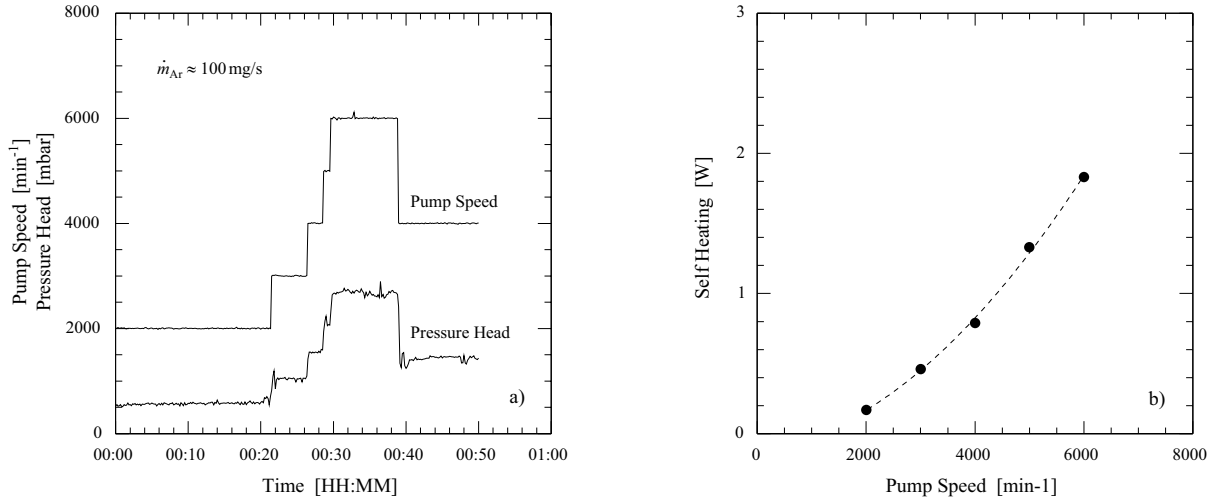


Figure 3.6: Performance of the Cryogenic Micropump

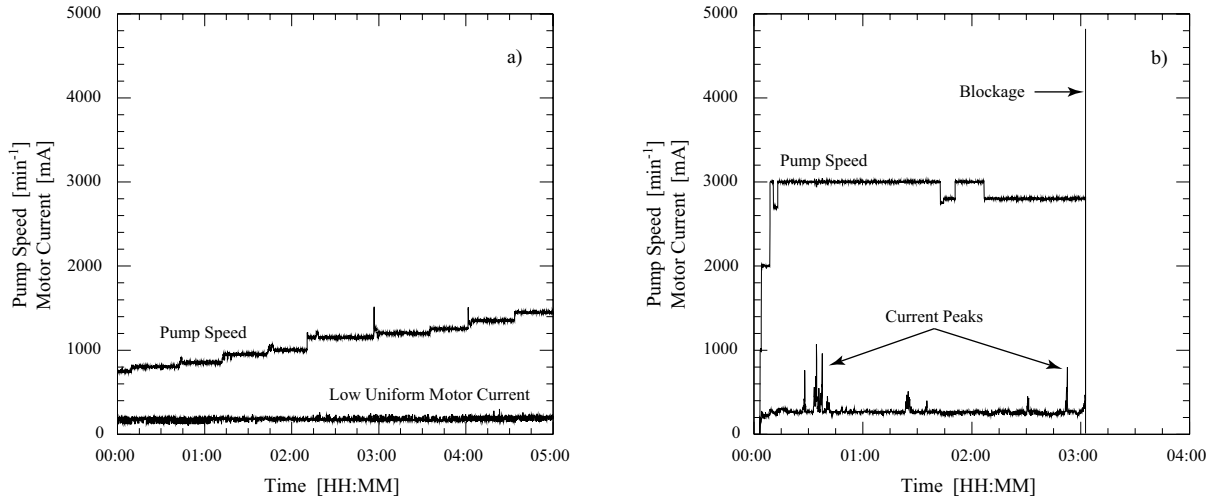


Figure 3.7: Operation of the Cryogenic Micropump

Unfortunately, the operation and performance achieved with the first prototype could not be reproduced with the new prototype design, which is the one presented in Section 3.2. Despite numerous efforts and experiments, this prototype always failed after a few seconds of operation due to severe mechanical problems. Impurities from fabrication and other reasons were considered but did not solve the problem.

As no final solution could be found within the frame of the project, the failure probability of design modifications is evaluated in Table 3.2. The last experiment was carried out with the original precision group from the first prototype, which was already operated for several hours (Figure 3.7). These components are therefore excluded from causing the failure.

Table 3.2: Design Modifications between the First and the Second Micropump Prototype

Component	Prototype 1	Prototype 2	Failure Probability
Inlet/outlet	Solder connector	Metallic connectors	/
Metallic seal	Indium seal	Ultra-flex TM seal	/
Coupling	Metal bellows coupling	Flexible beam coupling	/
Extension shaft	Solid, machined	Precision tube with welded journals	⊖
Flow direction	U-shaped	S-shaped	⊖
Inlet filter	None	Sinter filter ring sealed with Indium gasket	⊖
Base plate	Symmetric	Symmetric	⊖
	SST 316	Fe-Ni alloy	⊖
Fluid inlet plate	Slightly asymmetric	Slightly asymmetric	⊖
	SST 316	Fe-Ni alloy	⊖
Flange plate	Symmetric	Slightly asymmetric due to the outlet	⊖
	SST 316	Fe-Ni alloy	⊖
Dowel pins	SST 316	WC	⊖
Fixation bolts	4 of the same length	2 long and 2 short bolts, diagonally arranged	⊙
Support bearing	SST ball bearing	WC plain bearing	⊕
Failure indicators: / no influence ⊖ unlikely ⊙ possible ⊕ likely			

The general design principle for the pump body is to have as little thermal stress as possible in order to avoid displacement and deformation during cooldown. The material change in the periphery of the precision group from SST to the Fe-Ni alloy is certainly a big improvement and unlikely to cause the failure (see Figure 3.2). Slight asymmetries due to the inlet and outlet ports should also have little impact. Different lengths of the fixation bolts are a possible reason, as they shrink stronger than the plates and may develop asymmetric stress. The change of the support bearing, however, is more likely to cause the failure.

The symptoms from the last test clearly indicate a mechanical problem, i. e. misalignment of the precision bearings in the kidney plates and the support bearing after cooldown. As all components were successfully tested individually, the reason of failure is most likely found in the *sum of tolerances*. This problem did probably not appear with the first prototype design, because the tolerance of the support (ball) bearing was considerably larger. The following solution is therefore proposed:

- higher precision of the positional and shape tolerances of the dowel pin and support bearing holes in the flange plate,
- positioning of the dowel pins closer to the shaft, and

- increase of the support plain bearing tolerance, or installation of a ball bearing.

From experience one has to state that this failure reason is somewhat hypothetical, and there is no certainty that the proposed measures will solve the problem. An additional measure could be to increase the alignment forces in the pump body using INVAR as material for the dowel pins. This, however, contradicts the principle of thermal stress minimization.

3.4 Conclusions from the Micropump Development

The operating principle of a volumetric cryogenic micropump has been proven to work, and the measured performance data of the prototype meet the requirements for miniature cryogenic fluids circuits. If suitable conditions are provided for the pump body, there is no objective reason to believe that such a cryogenic micropump is less reliable than a room-temperature micro annular gear pump.

However, to guarantee suitable operating conditions at cryogenic temperatures is highly demanding. The development has revealed the difficulty of implementing idealized design rules in a real device. Handling of micron tolerances at room-temperature mechanics already requires sophisticated fabrication technologies. Even if the proposed design modifications are successful, thorough and costly control of fabrication and assembly will be required to ensure reliable operation.

Cryogenic micropumps may be used together with cryocoolers in future cryogenic applications that have tight spatial constraints, and which require low energy consumption of the cooling system. On the other hand, fluid circuits with a warm compressor are a suitable alternative in less restricted applications. Such systems require more space and consume more energy, but can be built with inexpensive off-the-shelf components.

4 HEAT TRANSFER IN MICROTUBES

4.1 Theoretical Background and Literature Survey

Heat Transfer in Single-phase Laminar Flow

Heat transfer at internal laminar flow in circular tubes can be calculated theoretically in case of fully developed velocity and temperature profiles, which was already pointed out in Section 2.3. At uniform surface heat flux, the Nusselt number Nu_∞ is a constant independent of Re and Pr . The solution of the energy equation gives

$$Nu_\infty = 4.364 \quad \text{at} \quad \dot{q} = \text{constant} , \quad (4.1)$$

and the approximation of the temperature profile in case of constant wall temperature yields

$$Nu_\infty = 3.656 \quad \text{at} \quad T_w = \text{constant} . \quad (4.2)$$

Modeling of the entry region gives one solution for the *thermal entry length problem*, where the velocity profile is fully developed, and a second solution for the *combined entry length problem*, where the temperature and velocity profiles develop simultaneously [34]. A number of correlations were developed, as the numerical solutions are complicated. The following correlation given in [20] represents a general form to describe the mean heat transfer, containing an entry term and the constant Nu_∞ for the developed region:

$$\overline{Nu} = \left[\left(\frac{a}{1-n} \left(\frac{Re Pr d}{L} \right)^n \right)^3 + Nu_\infty^3 \right]^{\frac{1}{3}} K_T . \quad (4.3)$$

For hydrodynamically developed flow, which is the case if the tube length before the heated section is longer than the hydrodynamic entry length $L_{E,h} = 0.05 Re d$, the coefficients have values of

$$\begin{array}{llll} \dot{q} = \text{const.}: & Nu_\infty = 4.364 & a = 1.1 & n = 0.35 \\ T_w = \text{const.}: & Nu_\infty = 3.656 & a = 0.89 & n = 0.35. \end{array}$$

The factor K_T considers the temperature dependence of fluid properties, and assumes values of

$$K_T = \left(\frac{\eta}{\eta_w} \right)^{0.14} \quad \text{for liquids, and} \quad K_T = 1 \quad \text{for gases.}$$

Recent literature on laminar heat transfer in microtubes is partially contradictory. For example, both *Qu et al.* [64] and *Rahman* [65] investigated heat transfer characteristics

in silicon microchannels. *Rahman* measured higher Nusselt numbers than classical correlations predict. *Qu* and his colleagues, on the other hand, found generally lower Nusselt numbers compared to numerical simulations. Both authors, however, conclude that the surface roughness is responsible for the deviations from classical models, which are made for hydraulically smooth tubes.

Heat Transfer in Single-phase Turbulent Flow

Heat transfer in turbulent flow can be modeled with the *Dittus* and *Boelter* equation, which gives in case of fluid heating [84]

$$Nu = 0.0243 Re^{0.8} Pr^{0.4} . \quad (4.4)$$

The correlation is valid for fully turbulent conditions of $Re > 10^4$. In the transition region of $2300 < Re < 10^4$, the *Hausen*-type equation of the form [20]

$$Nu = H_0 (Re^{H_1} - H_2) Pr^{0.4} \left[1 + \left(\frac{d}{L} \right)^{\frac{2}{3}} \right] K_T \quad (4.5)$$

is more precise. The coefficients and the parameter K_T have values of

$$\begin{aligned} \text{Gases } (0.5 \leq Pr \leq 1.5): \quad & H_0 = 0.0214 \quad H_1 = 0.8 \quad H_2 = 100 \quad K_T = 1 \\ \text{Liquids } (1.5 \leq Pr \leq 500): \quad & H_0 = 0.012 \quad H_1 = 0.87 \quad H_2 = 280 \quad K_T = \left(\frac{\eta}{\eta_w} \right)^{0.11} . \end{aligned}$$

Eq. (4.5) was first developed by *Hausen* [29], and improved later by *Gnielinski* [24].

It has been reported by various authors that turbulent heat transfer in microtubes is superior to the predictions made with these correlations. *Adams* et al. [3], [4] compared his experimental data with results from *Yu* et al. [86]. He correlated increasing deviations towards smaller tube diameters and proposed an enhancement factor for the *Gnielinski* equation. The effect of roughness, however, was not studied in detail.

Critical Reynolds numbers lower than $Re_{\text{crit}} = 2300$ for flow transition from laminar to turbulent flow have been reported by a number of authors [79], [57]. A general theory or model is not yet available. *Tso* [76], however, proposed a correlation based on the Brinkman number.

Flow-boiling Heat Transfer

Flow-boiling in circular tubes describes heat transfer mechanisms between a heated tube wall and a saturated fluid, which gains enthalpy and quality while flowing through the tube with forced convection. Flow-boiling is a complex process that comprises different boiling *regimes* and boiling *conditions*.

Flow-boiling *regimes* are distinguished as [83]

- *subcooled boiling*, in which the heat transfer coefficient increases as the bulk subcooled liquid approaches the saturation temperature;

- *nucleate boiling*, in which the heat transfer coefficient is nearly constant;
- *convective boiling*, in which the heat transfer coefficient increases with the fluid quality; and
- *post-burnout heat transfer*, in which the heat transfer gradually decreases to merge into a single-phase vapor forced convection regime.

Another important aspect of flow-boiling are *critical boiling conditions*, where the wall temperature can rapidly raise at just a slight increase of the heat load. Critical boiling conditions can have two distinctive forms:

- *Film boiling / departure from nucleate boiling* can occur at low quality (continuous liquid phase). At a critical heat flux a vapor layer is formed that separates the liquid from the heated surface. Heat transfer is strongly reduced due to the poor thermal conductivity of the vapor.
- *Dryout / burnout* occurs at high qualities, when the remaining liquid film tears off the wall, i. e. when the wall starts drying out. Heat transfer is reduced less than during film boiling, as the heated surface is cooled by high-quality vapor convection.

The occurrence of flow-boiling regimes and critical boiling conditions is influenced by a number of parameters, such as

the heat flux

$$\dot{q} = \frac{\dot{Q}}{A_w}, \quad (4.6)$$

the reduced pressure

$$p^* = \frac{p_s}{p_c}, \quad (4.7)$$

the mass flux

$$\dot{M} = \frac{\dot{m}}{A_c}, \quad (4.8)$$

the quality (vapor fraction)

$$x = \frac{h - h_l}{h_v - h_l}, \quad (4.9)$$

the tube diameter d , the tube orientation, the surface roughness R_a , and fluid properties.

The complexity of flow-boiling is reflected in a large number of publications. A detailed survey of almost all aspects of two-phase flow and heat transfer is published by *Hetsroni* [30]. His compilation concerns classical correlations that are experimentally verified for tube diameters larger than 3 mm to 5 mm. A comprehensive review of recent literature on flow-boiling in small channels is given by *Kandlikar* [41]. He concludes that, as a first order estimate, microchannel heat transfer may be predicted with flow-boiling correlations developed for large diameter tubes. *Petterson* [61] came to the same conclusion after broad studies on flow-boiling of CO₂ in parallel microchannel tubes of 0.8 mm inner diameter. He used several heat transfer models to fit his experimental data, and found the best agreement with the pool boiling correlation of the VDI Heat Atlas edited by *Gorenflo* [25].

Peng et al. [56] claimed that flow-boiling in microchannels can be quite different from heat transfer in macrotubes. He indicated that regular nucleate boiling does not exist, and introduced new concepts of *fictitious boiling*, *critical bubble size* and *evaporating space*. These hypotheses, however, were disproved by various experimental results, such as the data published by Zhang [87]. Other authors, for example Zhao [88], concluded that the heat transfer coefficient in microtubes is substantially higher than in macrotubes. Large flow instabilities in parallel microchannels were observed by a number of authors. Peles [55] even stated that two-phase flow in microchannels is inherently unstable.

So far, there are very few quantitative data for tubes or channels below $500\ \mu\text{m}$ diameter, which is the interesting range for package-integrated electronics cooling. Most published studies are conducted on application-oriented samples with parallel flow channels of various shapes (see Jiang [35] and [36], Peles [55], Ravigururajan [66]), or on single enhanced-surface channels documented by Zhang [87]. Although these data are valuable for practical applications, they do not form a suitable basis for the modeling of flow-boiling heat transfer, as the actual heat exchanger surface (and therefore the heat flux) is uncertain, or even unknown. In addition, maldistribution in parallel channels and arbitrary channel geometries complicate the comparability with conventional correlations.

Scope of Experimental Investigations

The ability to model local heat transfer coefficients is essential for the design of miniature heat exchangers. Due to the lack of published data, experiments were carried out with circular microtubes of $250\ \mu\text{m}$ and $500\ \mu\text{m}$ diameter, which are suitable dimensions for cooling of cryogenic tracking detectors. One single flow path was chosen to avoid negative impacts on the data by flow instabilities and maldistribution. The experiments were focused on nucleate boiling dominated heat transfer, which is the common regime in practical applications.

Although needed for the heat exchanger design, *local* flow-boiling heat transfer coefficients cannot be measured directly, as the applied heat load implies a quality change Δx . Mean heat transfer coefficients between x_{in} and x_{out} were therefore measured. The results were fitted with a heat exchanger model and the VDI Heat Atlas correlation for local flow-boiling heat transfer coefficients edited by Steiner [73]. The fitting algorithm is explained in Section 4.5. Details of the heat transfer correlation are discussed together with the experimental results in Section 5.3 and 5.4. Critical boiling conditions observed in the experiments are discussed in Section 5.5, but systematic studies and modeling were beyond the scope of the project.

4.2 Experimental Set-up

This Section describes the test facilities required to conduct heat transfer measurements in microtubes at cryogenic temperatures. The circuit scheme is shown in Figure 4.1. The working fluid is circulating in a closed circuit, which is designed for a maximum operating

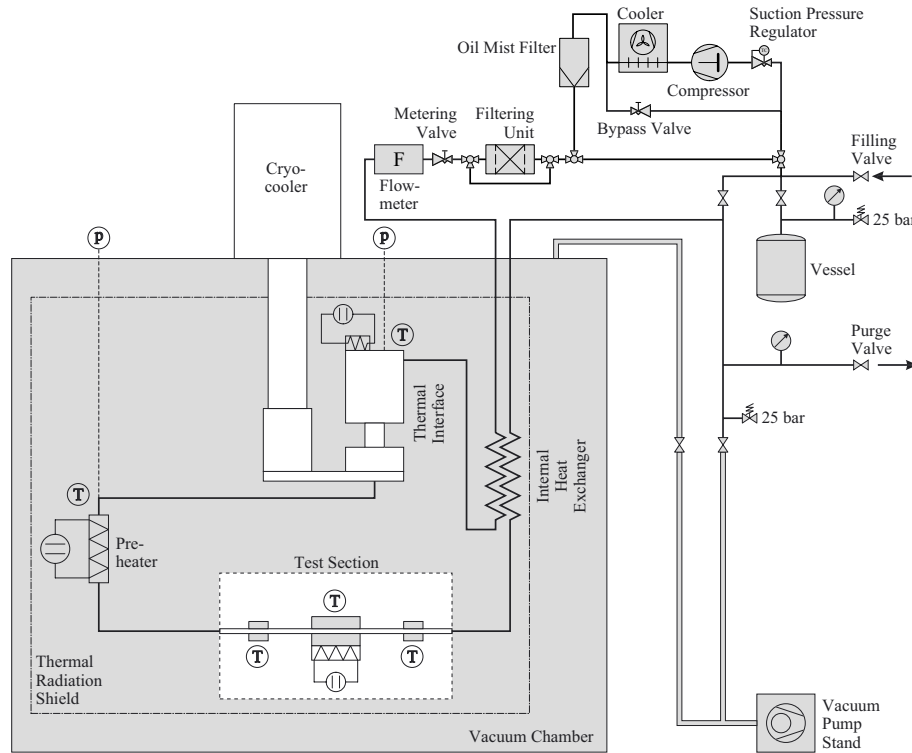


Figure 4.1: Experimental Set-up for Heat Transfer Measurements in Microtubes at Cryogenic Temperatures

pressure of 25 bar. The circuit consists of a warm part and a cold part. The warm part comprises a compressor unit for driving the fluid, a filtering system, a flowmeter, and some gas handling components. The cold part of the circuit is installed in a vacuum chamber operated under 10^{-6} mbar insulating vacuum. It is connected to the warm part via an internal heat exchanger that is also located in the vacuum chamber. The cold part consists of a thermal interface, an electrical pre-heater, and a test section. The thermal interface is attached to the cold finger of a cryocooler, which is the heat sink providing the cooling power. All cold circuit components are surrounded by a thermal radiation shield that is heat sunk to the cold finger.

The thermal interface consists of a condenser and a reservoir in the upper volume, and a sub-cooler heat exchanger in the lower volume. The reservoir is operated under saturation conditions (liquid/vapor phase equilibrium). The saturation temperature and the saturation pressure are stabilized by a temperature controller, using an electrical heater and a temperature sensor both installed on top of the thermal interface. The pre-heater serves to condition the temperature or the quality (vapor fraction) of the working fluid at the test section inlet. The fluid flow rate is controlled with both the by-pass valve in the compressor unit, and the metering valve. The design and control details of the major circuit components are presented in Section 6.

Sensors installed in the experimental set-up are listed in Table 4.1. The temperature

sensors and the electrical heaters were equipped for 4-lead differential measurement. The leads were heat-sunked to the cryocooler. The pressure sensors operated at room-temperature were connected with the cold circuit through capillary tubes. High-impedance filter frits were implemented to damp possible thermo-acoustic oscillations.

Table 4.1: Sensors Used in the Experimental Set-up

Sensor	Type	Model	Range	Accuracy
Temperature	PT-100	LakeShore TM PT-111	30 ... 673 K	$\pm 20 \text{ mK}^1$
Pressure	Strain Gauge	Schaevitz TM P9073	0 ... 25 bar (abs.)	$\pm 20 \text{ mbar}$
Mass Flow	Thermal	Hastings TM H-50K	0 ... 20 mmol/s He	$\pm 0.03 \text{ mmol/s}$
Vacuum	Pirani	Leybold TM TR 211	$5 \cdot 10^{-4} \dots 10^3 \text{ mbar}$	$\pm 20 \%$
	Penning	Leybold TM PR 25	$10^{-9} \dots 10^{-2} \text{ mbar}$	$\pm 30 \%$

The instruments listed in Table 4.2 communicated with a PC via GPIB interface. The pressure sensors and the flowmeter were connected directly to a multi-function DAQ board in the PC. During the experiments data were stored in text files with a time interval of 5 s. The accuracy of the experimental data is discussed in Section 4.5.

Table 4.2: Instruments of the Experimental Set-up

Instrument	Model	Accuracy
Temperature Controller	LakeShore TM 331	$\pm 10 \text{ mK}^2$
Temperature Monitor	LakeShore TM 218	$\pm 33 \text{ mK}^3$
Flowmeter	Hastings TM EALL-50KPGX	See Sensor
Power Supply	Rohde & Schwarz TM NGPT 35	$\pm 3.5 \text{ mV} / \pm 0.2 \text{ mA}$
Vacuum Pressure Gauge	Leybold TM CM 31	See Sensors

4.3 Concept of Heat Transfer Measurement in Microtubes

The concept of heat transfer measurements in microtubes differs from experiments with large tubes, as the inner wall temperature and the local heat transfer coefficient cannot be measured directly. The following shows how to determine the mean heat transfer coefficient and the mean inner wall temperature from the measured temperature of the heat exchanger body, and how the effective thermal resistance between the heat exchanger body and the inner wall of the flow channel can be obtained.

¹ Corresponds to the repeatability and the stability. Temperature sensors in the test section are cross-calibrated.

² Control stability.

³ Electronics accuracy.

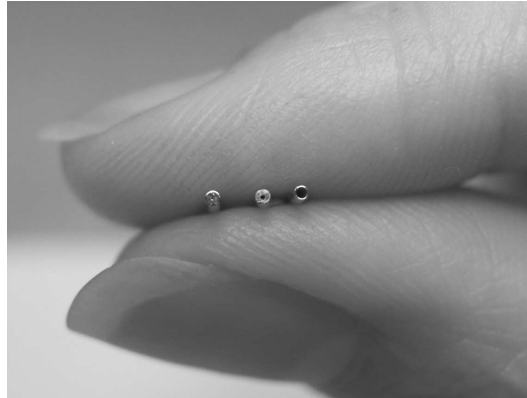


Figure 4.2: Microtubes of 800 μm Outer Diameter and 120, 250 and 500 μm Nominal Inner Diameter

Layout of the Test Section

The test section shown in Figure 4.3 consists of three high-conductivity copper blocks, which are soft-soldered onto the microtube. The middle block forms the compound heat exchanger together with the solder tin layer and the tube. It is heated by an electrical heater. The heater and the temperature sensor T_b are connected on opposite sides of the copper body. Two adiabatic copper blocks for temperature measurement are located up- and downstream of the heat exchanger at a distance larger than the thermal fin length in the tube wall. Since there is no heat load to these two blocks, the measured temperatures T_{in} and T_{out} are identical with the fluid bulk temperatures at these points. The temperature sensors T_{in} , T_b and T_{out} are cross-calibrated.

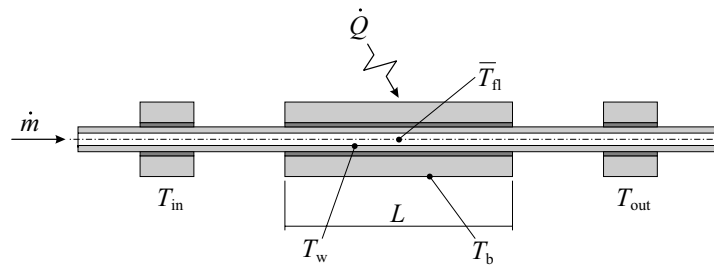


Figure 4.3: Layout of the Test Section with the Locations of Temperature Measurement

The radial temperature distribution is almost uniform around the tube due to the high thermal conductivity of the heat exchanger's copper body. This is shown in the thermal simulation of Figure 4.4, representing a transversal view through the center of the heat exchanger. The copper body has dimensions of $4 \times 6 \times 30 \text{ mm}$, and contains a $800 \times 250 \mu\text{m}$ stainless steel tube with a solder tin layer of $50 \mu\text{m}$. The electrical film heater covers an area of $6 \times 6 \text{ mm}$ in the middle of the right flat surface of the compound heat exchanger.

The pre-heater and the test section were assembled on the same tube as shown in Fig-

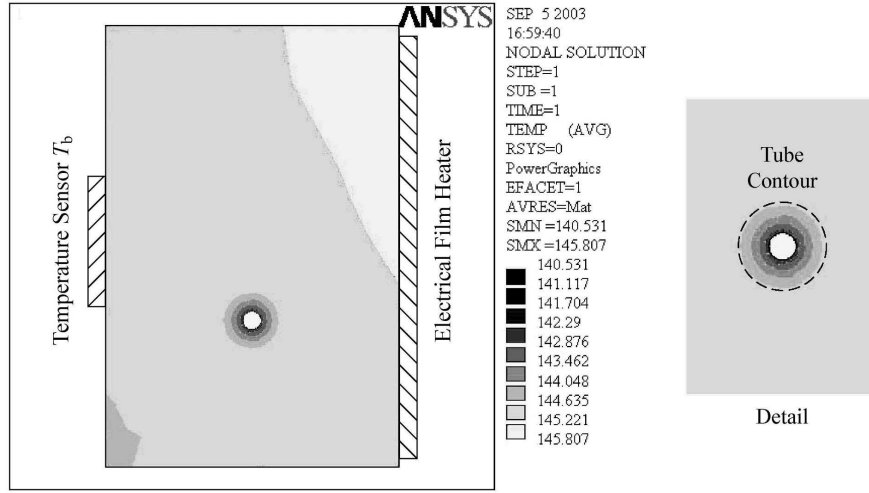


Figure 4.4: Radial Temperature Distribution in the Heat Exchanger Body at High Heat Flux; Thermal Simulation with $\dot{Q} = 5.0$ W, $T_s = 120$ K, and $\alpha = 10000$ W/m²K.

ure 4.5. The fluid is entering the tube in the sub-cooled liquid phase, which allows to determine its thermodynamical state from the measured pressure and temperature. The (single-phase) fluid temperature or (two-phase) fluid quality at the test section inlet is controlled by the pre-heater power. In the two-phase region, the fluid state at the test section inlet is calculated from the energy balance over the pre-heater. The tube length before the test section inlet is much larger than the hydrodynamic entry length, and the single-phase flow profiles in the test section are therefore always fully developed.

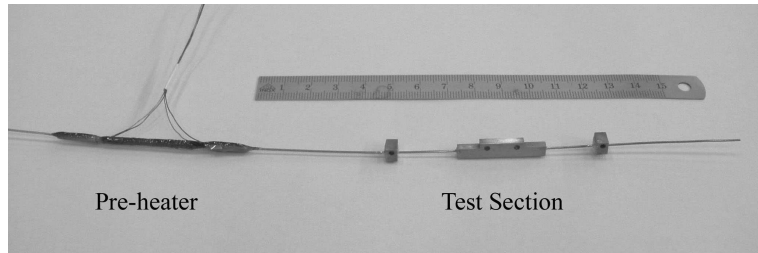


Figure 4.5: Pre-heater and Test Section Assembly

The mean heat transfer coefficient $\bar{\alpha}$ in the heat exchanger is defined as

$$\bar{\alpha} = \frac{\dot{Q}}{A_w \Delta T_{m,w}}, \quad (4.10)$$

where \dot{Q} is the heat load, A_w is the wetted surface of the flow channel, and $\Delta T_{m,w}$ is the mean temperature difference. $\Delta T_{m,w}$ is given in single-phase flow by the logarithmic

mean temperature difference

$$\Delta T_{m,w} = \frac{T_{\text{out}} - T_{\text{in}}}{\ln \left(\frac{\bar{T}_w - T_{\text{in}}}{\bar{T}_w - T_{\text{out}}} \right)}, \quad (4.11)$$

and in two-phase flow by

$$\Delta T_{m,w} = \bar{T}_w - \bar{T}_{\text{fl}}. \quad (4.12)$$

T_{in} and T_{out} are the fluid bulk temperatures at the inlet and at the outlet of the heat exchanger, \bar{T}_{fl} is the mean fluid temperature in the heat exchanger, and \bar{T}_w is the mean temperature of the wetted surface.

Eq. (4.11) and Eq. (4.12) are valid as the inner wall temperature is almost constant along the heat exchanger axis z , which is achieved by the high conductivity and by the geometry of the heat exchanger's copper body⁴. The assumption is verified by the thermal simulations shown in Figure 4.6. The location of the electrical heater is marked as a dashed square. Figure 4.6a represents experimental conditions at laminar flow with a large temperature difference in the fluid of $T_{\text{out}} - T_{\text{in}} = 15$ K. The inner wall temperature difference along the tube axis z is $\Delta T_w(z) \leq 1.0$ K. Figure 4.6b is the cross-sectional view of the simulation in Figure 4.4, representing flow-boiling heat transfer conditions with high heat load and constant fluid saturation temperature T_s . The inner wall temperature difference along the tube axis z is also $\Delta T_w(z) \leq 1.0$ K.

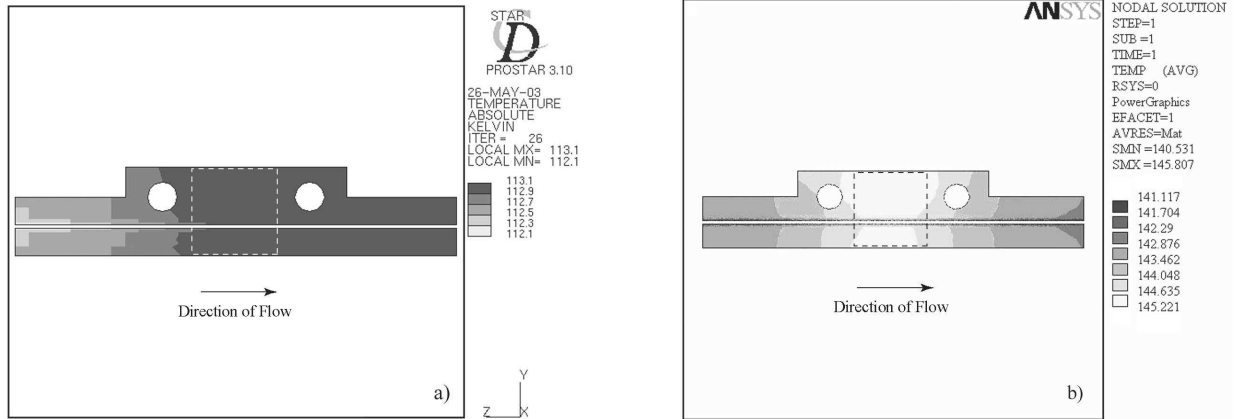


Figure 4.6: Thermal Simulations of the Inner Wall Temperature Distribution in the Heat Exchanger. a) Laminar Flow: $\dot{Q} = 0.5$ W, $\dot{m} = 28.6$ mg/s Argon, $T_{\text{in}} = 95$ K, $p = 15$ bar b) Two-phase Flow: $\dot{Q} = 5.0$ W, $T_s = 120$ K, $\alpha = 10000$ W/m²K.

As $T_w(z)$ and \bar{T}_w cannot be measured directly, the copper body temperature T_b is measured, and Eq. (4.10) to (4.12) change to

$$\bar{k} = \frac{\dot{Q}}{A_w \Delta T_{m,b}}, \quad (4.13)$$

⁴ $\Delta T_w(z)$ can be further reduced by increasing the mass of the copper body, and by a uniform distribution of the heat load.

with

$$\Delta T_{m,b} = \frac{T_{\text{out}} - T_{\text{in}}}{\ln \left(\frac{T_b - T_{\text{in}}}{T_b - T_{\text{out}}} \right)} \quad (4.14)$$

in single-phase flow, and

$$\Delta T_{m,b} = T_b - \bar{T}_{\text{fl}} \quad (4.15)$$

in two-phase flow.

\bar{k} is the mean *overall* heat transfer coefficient related to the wetted surface A_w . It is obtained directly from the measured data, and is related with $\bar{\alpha}$ by the following model.

The heat exchange between the fluid and the area in the copper body, where the temperature sensor T_b is located, can be modeled as a series connection of thermal resistances R . The measured overall heat transfer coefficient \bar{k} is then expressed in the form

$$\bar{k} = \frac{1}{(\bar{R}_\alpha + R_{\text{eff}}) A_w} = \frac{1}{\frac{1}{\bar{\alpha}} + R_{\text{eff}} A_w} . \quad (4.16)$$

Here R_{eff} is defined as the effective thermal resistance of the compound heat exchanger, and includes both conductivity and contact resistances of the various layers between the wetted surface A_w and the location of the temperature sensor T_b . If R_{eff} is known, $\bar{\alpha}$ can be calculated as

$$\bar{\alpha} = \frac{\bar{k}}{1 - \bar{k} A_w R_{\text{eff}}} . \quad (4.17)$$

Determination of the Effective Thermal Resistance R_{eff}

The concept of determining the effective thermal resistance R_{eff} of the compound heat exchanger is similar to a so-called *Wilson Plot Method* described in [61], [62]. The general idea is that a model for single-phase turbulent heat transfer is fitted to a set of experimental data on overall heat transfer coefficients \bar{k} . The data set is taken with varying mass flow, as the heat transfer coefficient in turbulent flow mainly depends on the Reynolds number. The thermal conditions, i. e. the heat load and the fluid temperature level, are kept constant. If the model is appropriate, one can extract the varying heat transfer coefficient $\bar{\alpha}$ from the fit, and some static parameter that involves the difference between $\bar{\alpha}$ and \bar{k} in the experiment.

Instead of applying the graphical *Wilson Plot Method* with a linear regression, the mathematical minimization tool *Minuit* implemented in the *ROOT* package [68] is used here to fit the experimental data directly. The benefits are that there is practically no restriction for the shape of the fit function and for the number of variables, and the fit also yields information of its meaningfulness. The number of free parameters should be as low as possible, but theoretically extends to a maximum of $N - 1$ for N data points.

To develop a suitable fit function, Eq. (4.16) is written in the form

$$\frac{1}{\bar{k}} = \frac{1}{\bar{\alpha}} + R_{\text{eff}} A_w . \quad (4.18)$$

Substituting $\bar{\alpha}$ with

$$\bar{\alpha} = \frac{Nu \lambda}{d}, \quad (4.19)$$

and Nu with Eq. (4.5) as heat transfer model in turbulent flow yields the fit function

$$\frac{1}{\bar{k}} = \frac{d}{H0 (Re^{H1} - H2) Pr^{0.4} \left[1 + \left(\frac{d}{L} \right)^{\frac{2}{3}} \right] \left(\frac{\eta}{\eta_w} \right)^{0.11} \lambda} + H3 A_w. \quad (4.20)$$

$H0$, $H1$ and $H2$ are parameters of the heat transfer model, and $H3 = R_{\text{eff}}$ is the effective thermal resistance. The dimensionless numbers Re , Pr and (η/η_w) , as well as the fluid thermal conductivity λ are the variables determined from actual mean fluid properties at each data point. The Hausen type Eq. (4.5) is preferred to the Dittus and Boelter type Eq. (4.4), as it has higher accuracy in the transition region of $Re = 2300$ to $Re = 10000$.

An example of using Eq. (4.20) for fitting experimental data is shown in Figure 4.7. The heat transfer coefficient $\bar{\alpha}$ becomes infinite at infinite Reynolds numbers, and the left summand in Eq. (4.20) becomes zero. The asymptotic value of the plot is then equal to the product $R_{\text{eff}} A_w$.

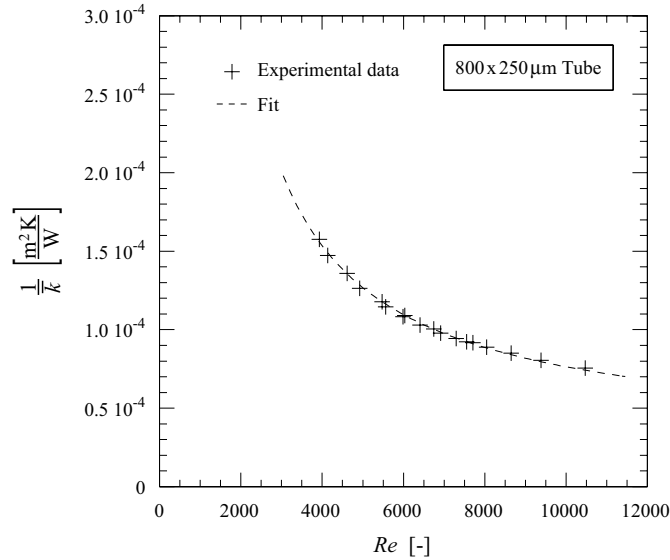


Figure 4.7: Fitting Turbulent Heat Transfer Data with Eq. (4.20);
Example Data of a Heat Exchanger with a $800 \times 250 \mu\text{m}$ Tube

The good agreement between the data and the fit suggests that the model is appropriate. Experimental data at high Reynolds number are clearly the most significant, as the lever arm of the fit function to $Re \rightarrow \infty$ is very long. In the example, the coefficients $H0$ and $H2$ were fixed to

$$\begin{aligned} H0 &= 0.012 \quad \text{and} \\ H2 &= 280, \end{aligned}$$

complying with the conventional correlation of Eq. (4.5). In a first fitting loop, both the Reynolds exponent H1 and H3 were free parameters. The fitted value of H1 was then fixed in a second fitting loop. With only one free parameter H3 the value and the error of the effective thermal resistance was then obtained.

The underlying assumption that R_{eff} is a constant, however, has to be discussed in more detail:

In flow-boiling heat transfer, the fluid saturation temperature is nearly constant as well as the inner wall temperature, which was shown in Figure 4.6b for high heat flux operation. It follows that, under the condition of constant local heat transfer coefficients⁵, the relative heat flux in each heat exchanger section is always the same. The heat load therefore always travels on the same path through the compound heat exchanger. R_{eff} can then be understood as a “material property”, comprising only conductivity and contact⁶ resistances. R_{eff} is specific to the location of the temperature sensor T_b , and (in first order) independent of the overall heat flux.

In single-phase flow, however, the *relative* heat flux in each heat exchanger section depends on the exponential form of the fluid temperature profile, as well as on the absolute value of the logarithmic mean temperature difference. R_{eff} consequently changes with the flow rate, which is in contrast to Eq. (4.20). The modeling of these dependencies is not straightforward, and the fit function must therefore remain incomplete.

To determine R_{eff} for two-phase measurements, it is important to measure data at the highest possible Reynolds number, and with the lowest possible $\Delta T_{\text{fl}} = T_{\text{out}} - T_{\text{in}}$. The small systematic error caused by the asymmetric heat flux distribution is partially compensated by the saturation temperature shift (due to the two-phase pressure drop) when placing the sensor T_b in the middle of the heat exchanger⁷. Under appropriate conditions, the systematic error is well below the statistical error for determining R_{eff} .

The systematic error of using R_{eff} to correct single-phase heat transfer data increases with the increasing asymmetry in the heat flux distribution, which is proportional to the distribution of temperature differences between the fluid and the wall along the heat exchanger axis. The asymmetry increases both with increasing ΔT_{fl} , and with decreasing logarithmic mean temperature difference, i. e. with increasing heat transfer coefficients $\bar{\alpha}$. The influence of R_{eff} on the ratio $\bar{\alpha}/\bar{k}$ also increases with $\bar{\alpha}$ following Eq. 4.17. Experiments with turbulent liquid flow should therefore be conducted at low ΔT_{fl} . In laminar liquid and turbulent vapor measurements, on the other hand, the systematic error of R_{eff} is insignificant due to lower heat transfer coefficients $\bar{\alpha}$.

The analysis of the heat transfer measurements presented in Section 5 is based on R_{eff} , following Eq. (4.17). Despite the small systematic errors, R_{eff} is considered as a constant for all single-phase and flow-boiling heat transfer data. The installation of a test section including sensors is kept unchanged throughout the experiments, which are conducted at a

⁵ This will be shown later in Section 5.

⁶ The contact resistance also includes incomplete surface wetting of the solder tin.

⁷ Mirrored heat flux distribution in a symmetric assembly.

fixed temperature level to assure constant material conductivities and contact resistances⁸. The ratio of $\bar{\alpha}/\bar{k}$ in Table C.1 and C.2 illustrates that R_{eff} has little influence in laminar liquid and turbulent vapor flow, but it becomes significant in turbulent liquid and flow-boiling heat transfer.

4.4 Characteristic Dimensions in Rough Tubes

For the analysis of experimental data and their representation in form of correlations it is essential to determine the characteristic dimensions of the tubes used in the experiments. This is particularly important in the case of microtubes, where the actual diameter may deviate from the nominal diameter, and where the roughness can have a significant influence on the heat transfer.

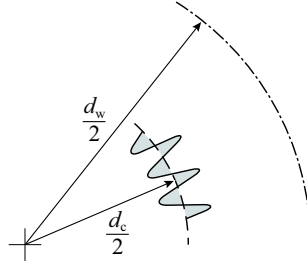


Figure 4.8: Characteristic Dimensions in Rough Tubes

In tubes with large roughness, the cross-section A_c and the wetted surface A_w have to be defined independently. Figure 4.8 compares a circular smooth tube of diameter $d = d_c$ with a rough tube of the same cross-sectional area. One characteristic dimension of such a rough tube can be defined as

$$d_c = \sqrt{\frac{4 A_c}{\pi}}, \quad (4.21)$$

which is the diameter of a perfectly smooth circular tube of the same cross-sectional area. A_c and therefore d_c determine the fluid velocity w and the mass flux \dot{M} :

$$w = \frac{\dot{m}}{\rho A_c}, \quad (4.22)$$

$$\dot{M} = \frac{\dot{m}}{A_c}. \quad (4.23)$$

A second characteristic dimension d_w shall be defined as

$$d_w = \frac{P}{\pi}. \quad (4.24)$$

⁸ Contact resistances would vary only due to changed forces between material layers, caused by differences in thermal dilatation.

P is the perimeter of the rough tube, and d_w is the diameter of a perfectly smooth circular tube with identical wetted surface area. The wetted surface area A_w of a heat exchanger of length L is calculated as

$$A_w = P L . \quad (4.25)$$

Eq. (4.25) assumes that the axial roughness is small compared to the radial roughness, which is usual for drawn tubes.

The literature review on surface roughness effects in small tubes by *Kandlikar et al.* [42] shows, that the hydraulic diameter

$$d_h = \frac{4 A_c}{P} \quad (4.26)$$

is used almost exclusively as characteristic dimension. However, from Figure 4.8 it is evident that d_h has no physical relation to the wetted surface of tubes with large roughness. This may explain why experimental data of larger tubes are usually in good agreement with theoretical predictions, whereas deviations increase toward small dimensions, i. e. increasing relative roughness. It is important to note that the actual wetted surface area A_w of tubes with large roughness can only be determined by direct optical measurement, and *not* indirectly through d_h by means of e. g. pressure drop measurements with laminar flow (see Eq. (5.5)).

The two characteristic diameters d_c and d_w of the microtubes used in the experiments were determined from microscope images. After finishing the experiments, three cross-sectional samples and one longitudinal sample were prepared from each microtube, taken from the 30 mm long area where the heat exchanger was situated. Images with reference dimensions were taken under an optical and an electron microscope. Examples of these images are shown in Figure 4.9 and Figure 4.10.

The images were converted into vector graphics, which allowed to measure the actual cross-sectional area A_c and the perimeter P . The results of the image analysis are summarized in Table 4.3. The data presented are mean values determined from the values measured for the three cross-sectional images. The errors are calculated as the square root of the mean square deviation from the mean values. Systematic errors were not evaluated, as they are small in comparison with the RMS deviations.

Table 4.3: Characteristic Dimensions of the Measured Microtubes

Microtube (OD \times ID)	800 \times 250 μm	800 \times 500 μm
Perimeter P	$(106.5 \pm 8.1) \times 10^{-5} \text{ m}$	$(184.6 \pm 2.5) \times 10^{-5} \text{ m}$
Cross-section A_c	$(63.0 \pm 8.8) \times 10^{-9} \text{ m}^2$	$(238.4 \pm 4.8) \times 10^{-9} \text{ m}^2$
Heat Exchanger Length L	$3.0 \times 10^{-2} \text{ m}$	$3.0 \times 10^{-2} \text{ m}$
Wetted Surface A_w	$(31.9 \pm 2.4) \times 10^{-6} \text{ m}^2$	$(55.4 \pm 0.8) \times 10^{-6} \text{ m}^2$
Characteristic Diameter d_c	$283 \pm 20 \mu\text{m}$	$551 \pm 6 \mu\text{m}$
Characteristic Diameter d_w	$339 \pm 26 \mu\text{m}$	$588 \pm 8 \mu\text{m}$

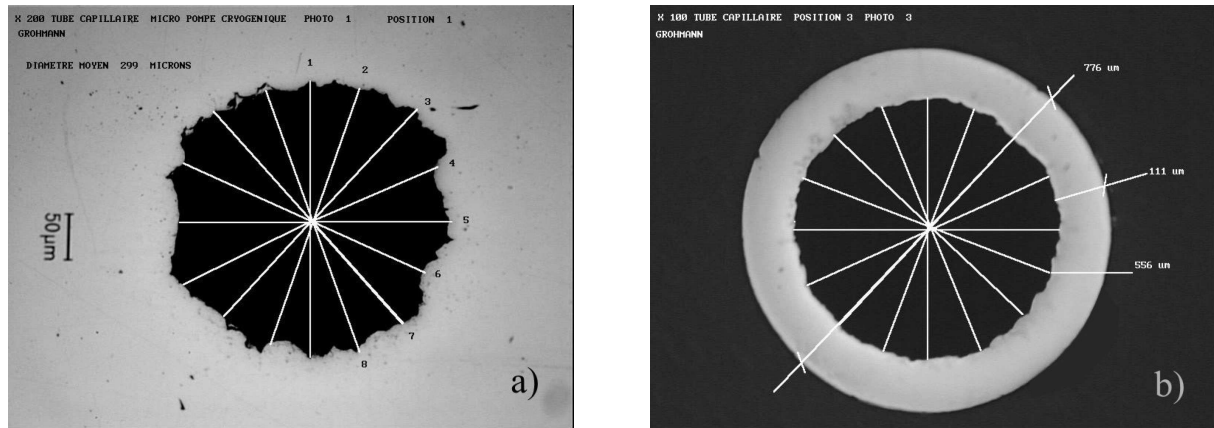


Figure 4.9: Examples of Images of Transversal Cuts of the Microtubes. a) Tube $800 \times 250 \mu\text{m}$, Magnification Factor 200; b) Tube $800 \times 500 \mu\text{m}$, Magnification Factor 100

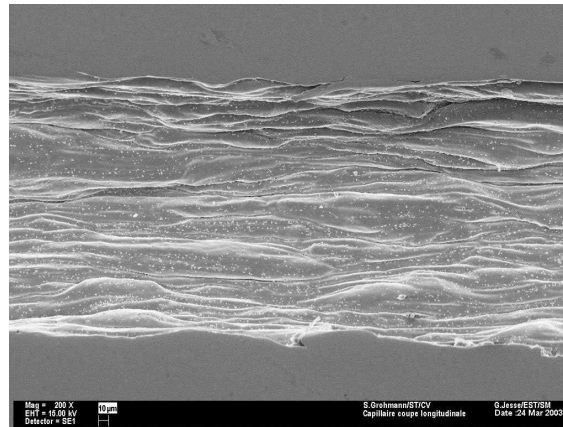


Figure 4.10: Axial Cut of the Microtube $800 \times 250 \mu\text{m}$, Magnification Factor 200

The relative roughness of the tubes can be expressed with a new parameter r_d defined as

$$r_d = \frac{d_w}{d_c} . \quad (4.27)$$

This parameter has values of $r_d = 1.20 \pm 0.12$ for the $800 \times 250 \mu\text{m}$ tube, $r_d = 1.07 \pm 0.02$ for the $800 \times 500 \mu\text{m}$ tube, and $r_d = 1.0$ in smooth circular tubes. The relative roughness parameter r_d is a measure for changed surface to volume ratios compared to smooth circular tubes. It is not identical with the commonly used relative roughness ϵ , which is defined as $\epsilon = R_a/d$. R_a is the arithmetic mean of the absolute values of vertical deviation from the mean line through the rough profile [8], and d is the mean line diameter.

The characteristic diameters are used in the Reynolds number and in the Nusselt number. The Nusselt number is the dimensionless temperature gradient at the wetted surface, defined as

$$Nu = \frac{\alpha d_w}{\lambda} . \quad (4.28)$$

The Reynolds number can be interpreted as the ratio of inertia to viscous forces in the velocity boundary layer [34]. As the boundary layer develops at the wetted surface, Re is also defined with d_w as characteristic diameter

$$Re = \frac{w \rho d_w}{\eta} . \quad (4.29)$$

The definitions of d_c and d_w in Eq. (4.21) and Eq. (4.24) assume similarity between smooth circular tubes and rough tubes. This similarity shall be discussed with an example of experimental data for laminar liquid heat transfer, shown in Figure 4.11.

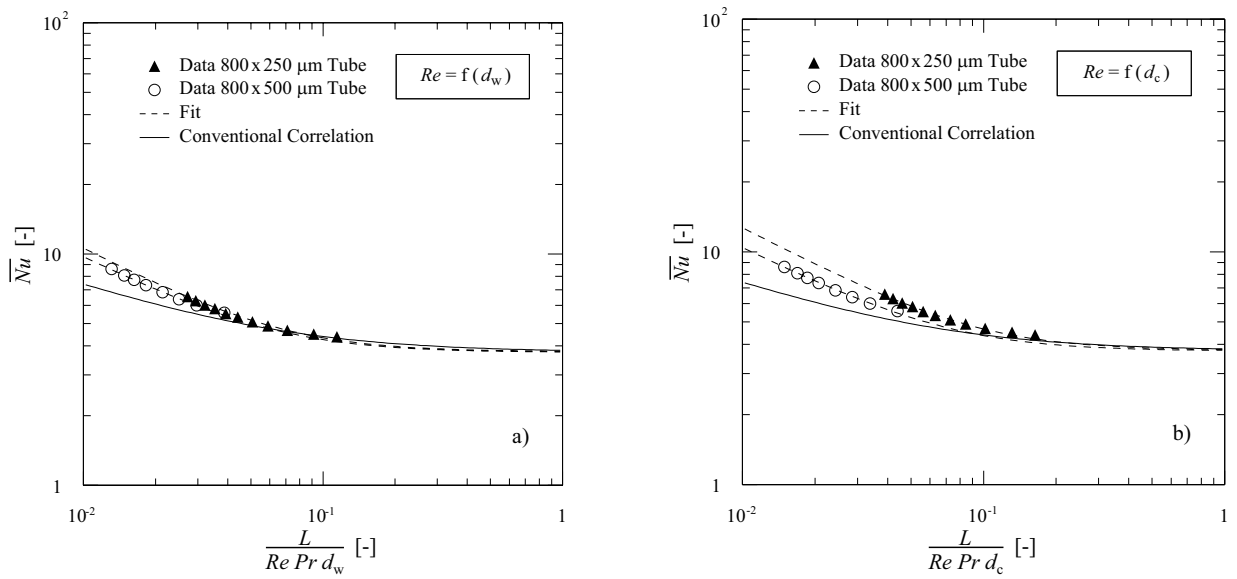


Figure 4.11: Example of Using d_c and d_w from Table 4.3 as Characteristic Dimensions to Evaluate Laminar Liquid Heat Transfer Data. a) $\overline{Nu} = f(d_w)$, $Re = f(d_w)$; b) $\overline{Nu} = f(d_w)$; $Re = f(d_c)$

The data in Figure 4.11a are evaluated with the definitions of Nu and Re according to Eq. (4.28) and Eq. (4.29). The *Conventional Correlation* represents average Nusselt numbers for hydrodynamically developed flow and constant wall temperature according to Eq. (4.3). In long tubes and at low Reynolds numbers, the function approaches asymptotically the value of $Nu_\infty = 3.656$, which is the analytical solution for fully developed hydrodynamical and thermal profiles in circular tubes. The experimental data show higher Nusselt numbers for short tubes, which indicates that the heat transfer in the thermal entry region is better than predicted by the corresponding empirical term in Eq. (4.3). However, the data can be clearly fitted to $Nu_\infty = 3.656$, and therefore comply with the theory for smooth circular tubes.

Although the results in Figure 4.11a confirm the similarity between rough and smooth tubes, they give no information of whether the value of d_w is correct or not. As the

measured heat transfer coefficient α is given as

$$\bar{\alpha} = \frac{\dot{Q}}{A_w \Delta T_m}, \quad (4.30)$$

the diameter cancels out in the Nusselt number, if A_w and d_w are calculated from the same perimeter P

$$\overline{Nu} = \frac{\bar{\alpha} d_w}{\lambda} = \frac{\dot{Q}}{\pi L \Delta T_m \lambda}. \quad (4.31)$$

The effect of a different value of the characteristic diameter is demonstrated in Figure 4.11b, where Re and the reduced length (abscissa) are calculated with d_c instead of d_w .

The experimental results of laminar liquid heat transfer are discussed in more detail in Section 5.1.

4.5 Experimental Program and Data Analysis

The experimental program was defined to study typical cooling conditions of cryogenic tracking detectors, and to understand and explain possible deviations from common heat transfer behavior when scaling to microtube dimensions. Argon of 99.9995% purity was chosen as working fluid for operating silicon detectors at 130 K. The absolute system pressure was kept around 15 bar, which corresponds to a saturation temperature of 124 K. Experiments were conducted with two microtubes of 250 μm and 500 μm nominal inner diameter.

All experimental data were taken under steady state conditions over a period of 5 min, and with a time interval of 5 s. For each quantity x , the arithmetic mean value \bar{x} as well as the standard deviation σ_x were calculated from the 60 readings x_i

$$\bar{x} = \frac{1}{n} \sum_{i=1}^n x_i \quad ; \quad \sigma_x = \sqrt{\frac{1}{n-1} \sum_{i=1}^n (x_i - \bar{x})^2}. \quad (4.32)$$

The zero-offset of the flowmeter was measured in the beginning of each experimental session, and was used for correcting the flowmeter readings. The three temperature sensors T_{in} , T_b and T_{out} of the test section were cross-calibrated once after a new installation. Statistical errors of the instruments σ_i (such as repeatability and stability) and statistical errors obtained from the zero-offset and cross-calibrations σ_{cal} were added to σ_x with the Gaussian error propagation method [53] to obtain the uncertainty Δx of the measured quantity:

$$\Delta x = \sqrt{\sigma_x^2 + \sigma_i^2 + \sigma_{\text{cal}}^2}. \quad (4.33)$$

The errors of the derived quantities $\bar{z} = f(\bar{x}; \bar{y})$ were calculated from the errors of the directly measured quantities Δx and Δy as

$$\Delta z = \sqrt{\left(\frac{\partial f}{\partial x} \Delta x\right)^2 + \left(\frac{\partial f}{\partial y} \Delta y\right)^2}. \quad (4.34)$$

The uncertainty of the overall heat transfer coefficient \bar{k} depends on

$$\Delta\bar{k} = f(\Delta\dot{Q}; \Delta A_w; \Delta T_b; \Delta T_{in}; \Delta T_{out}) \quad (4.35)$$

in single-phase flow, and

$$\Delta\bar{k} = f(\Delta\dot{Q}; \Delta A_w; \Delta T_b; \Delta\bar{T}_f) \quad (4.36)$$

in two-phase flow, following Eq. (4.13) to (4.15). The uncertainty of the heat transfer coefficient $\bar{\alpha}$ yields with Eq. (4.17)

$$\Delta\bar{\alpha} = f(\Delta\bar{k}; \Delta A_w; \Delta R_{eff}) . \quad (4.37)$$

Although all these errors are obtained from experimental data sets with assumed Gaussian statistics yielding Eq. (4.32), two types of errors have to be distinguished. The pure statistical errors are $\Delta\dot{Q}$ and ΔT s, as these directly measured quantities are statistically distributed throughout the experiments. ΔA_w and ΔR_{eff} are considered as systematic errors, since they do not vary. However, they cannot be corrected as their sign is unknown.

The same principle applies for the error analysis of Reynolds numbers, and the quality. Measured quantities with statistical variations are considered to have statistical errors; constant errors in dimensions and fluid properties are considered as uncorrected systematic errors. Both types of errors (or measuring uncertainties) are presented separately for each data point in Appendix C.

Analysis of Single-phase Heat Transfer Data

The experimental program for single-phase heat transfer was focused on the measurement of the effective thermal resistance R_{eff} , and to support modeling of flow-boiling heat transfer. Requirements on the experimental set-up in single-phase heat transfer are rather different from two-phase operation, especially in laminar flow and in vapor phase measurements. Studies on single-phase heat transfer were therefore limited to the following program:

- | | |
|------------------------|----------------------------------------------------------------------------------------------------------------------------------------------------------------------------------------------------------------------------------------------------------------------------------|
| Turbulent liquid flow: | Experiments were performed at constant heat load and variable flow rate with liquid of about 30–15 K sub-cooling. For each tube, the parameters of the heat transfer correlation and the effective thermal resistance R_{eff} were obtained from fitting the same set of data. |
| Turbulent vapor flow: | Experiments and system design were not focused on vapor-phase measurements. However, data were taken to support modeling of convective boiling heat transfer. The data measured at 5–25 K super-heating are less accurate than the liquid-phase measurements. |
| Laminar liquid flow: | Experiments were conducted at constant heat load and variable flow rate with liquid of about 35–10 K sub-cooling. Mean heat transfer coefficients were measured in hydrodynamically developed flow and at constant wall temperature. |

Laminar vapor flow: The instrumentation was not designed for this flow regime. No data were taken.

The calculation of heat transfer coefficients, Nusselt and Reynolds numbers was already explained in Section 4.3 and 4.4. Mean fluid properties were calculated with the GASPAK package [16] as a function of the mean fluid temperature and the pressure. The mean fluid temperature was calculated as

$$\bar{T}_{\text{fl}} = \frac{1}{2} (T_{\text{in}} + T_{\text{out}}) . \quad (4.38)$$

As the pressure was only measured upstream of the pre-heater, a frictional pressure drop correlation [43] was applied for correcting the pressure in the test section. The effect of the pressure drop on fluid properties is negligible in liquid phase measurements, but it is significant in the vapor phase.

For modeling of single-phase heat transfer data, the Prandtl number was calculated from the fluid dynamic viscosity η , the specific heat c_p , and the thermal conductivity λ as

$$Pr = \frac{\eta c_p}{\lambda} . \quad (4.39)$$

In liquid phase heat transfer, the temperature dependence of fluid properties was taken into account by a ratio $(\eta/\eta_w)^n$, requiring the tube wall temperature T_w for $\eta_w = f(p, T_w)$. This temperature was calculated iteratively with the modeled heat transfer coefficient α^*

$$T_w = \frac{e^{[(T_{\text{out}} - T_{\text{in}}) \alpha^* A_w \dot{Q}^{-1}]} T_{\text{out}} - T_{\text{in}}}{e^{[(T_{\text{out}} - T_{\text{in}}) \alpha^* A_w \dot{Q}^{-1}]} - 1} . \quad (4.40)$$

Experimental data were fitted with the heat transfer models of Eq. (4.3) and (4.5), respectively, using the *Minuit* minimization tool of ROOT [68]. The C++ source code of the fitting routine for turbulent liquid flow heat transfer is presented in Appendix B.1. The code for laminar liquid flow and turbulent vapor flow is similar, requiring only the adaptation of the fit function **FitFunc**, and the adaptation of fixed and free parameters.

As explained before, turbulent liquid data were analyzed first to obtain both the fitted turbulent liquid flow heat transfer correlation, and the effective thermal resistance R_{eff} . Turbulent vapor flow data, laminar liquid flow data, and flow-boiling heat transfer data were analyzed afterwards with R_{eff} as a fixed parameter. This illustrates that all heat transfer measurements are coupled. On one hand they are connected through the effective thermal resistance R_{eff} , and on the other hand single-phase heat transfer data are used for modeling of convective boiling heat transfer.

Analysis of Flow-boiling Heat Transfer Data

Experiments on flow-boiling heat transfer were focused on nucleate boiling, which is the dominant regime in most applications. Nevertheless, a few data were taken under pure convective boiling conditions to support the modeling of experimental results. The program of two-phase flow heat transfer measurements was as follows:

Convective boiling:	Experiments were performed with a heat flux lower than required for the onset of nucleate boiling ($\dot{q} < \dot{q}_{\text{onb}}$). Data series were taken at constant mass flow, constant heat load (constant Δx) and variable inlet quality x_{in} .
Flow-boiling:	Experiments were conducted in the nucleate boiling dominated regime at a heat flux $\dot{q} > \dot{q}_{\text{onb}}$. Data series were taken at constant mass flow rates. Mean heat transfer coefficients were measured between $x_{\text{in}} \approx 0$ and x_{out} . The heat load \dot{Q} was ramped up until the outlet quality reached $x_{\text{out}} \approx 1$, or until critical boiling conditions occurred.

To determine the flow-boiling heat transfer coefficient $\bar{\alpha}$ with the equations explained in Section 4.3, the fluid bulk temperature \bar{T}_{fl} in the heat exchanger was calculated from the temperature T_{out} measured at the test section outlet. However, the pressure drop between the middle of the heat exchanger and the location of the sensor T_{out} yielded a saturation temperature shift. To correct the temperature shift, the pressure p measured upstream of the pre-heater was used (see Figure 4.1). As the single-phase pressure drop between the pressure pick-up and the test section inlet was negligible, the measured pressure corresponded to the saturation pressure at the test section inlet. The mean fluid saturation temperature was therefore calculated as

$$\bar{T}_{\text{fl}} = \frac{1}{2} (T_{\text{s}}(p) + T_{\text{out}}) . \quad (4.41)$$

The saturation temperature shift between \bar{T}_{fl} and T_{out} ranged from about 0.1 K to 0.8 K in the $800 \times 250 \mu\text{m}$ tube, depending on the mass flux and the quality. In the $800 \times 500 \mu\text{m}$ tube the saturation temperature shift was generally below 0.1 K.

To calculate the fluid qualities at the test section inlet and outlet, the reference fluid enthalpy h was determined from pressure and temperature measurements in the sub-cooled liquid phase upstream of the pre-heater $h = f(p, T)$. The fluid enthalpies at the test section inlet and outlet were calculated with the energy balance over the heat exchangers

$$h_{\text{in}} = h + \frac{P_{\text{pre}}}{\dot{m}} , \quad (4.42)$$

$$h_{\text{out}} = h + \frac{P_{\text{pre}} + \dot{Q}}{\dot{m}} , \quad (4.43)$$

where P_{pre} is the pre-heater power, and \dot{Q} is the heat load of the test section heat exchanger. The inlet and outlet qualities were calculated with the saturated liquid and vapor enthalpies, which are functions of the mean fluid saturation temperature \bar{T}_{fl}

$$h_{\text{l}}, h_{\text{v}} = f(\bar{T}_{\text{fl}}) , \quad (4.44)$$

$$x_{\text{in}} = \frac{h_{\text{in}} - h_{\text{l}}}{h_{\text{v}} - h_{\text{l}}} , \quad (4.45)$$

$$x_{\text{out}} = \frac{h_{\text{out}} - h_{\text{l}}}{h_{\text{v}} - h_{\text{l}}} . \quad (4.46)$$

In general, local heat transfer coefficients cannot be measured directly in two-phase flow, as the heat load implies a quality change Δx . The concept was therefore to measure mean

heat transfer coefficients $\bar{\alpha}$ between $x_{\text{in}} \approx 0$ and x_{out} , and to fit the experimental data with a heat exchanger model that numerically integrates correlated local heat transfer coefficients. The flowchart of such an algorithm is shown in Figure 4.12. The modeling of the local flow-boiling heat transfer is based on the VDI Heat Atlas correlation edited by *Steiner* [73].

The fitting algorithm works the following way:

- In the beginning, $i = 1 \dots M$ sets of experimental data are read from a data file. Each set contains all the operating conditions and fluid properties needed in the algorithm, such as the measured heat transfer coefficient $\bar{\alpha}_i$, the error of the heat transfer coefficient $\Delta\bar{\alpha}_i$, the heat load \dot{Q}_i , the outlet quality $x_{\text{out},i}$ and so on.
- Single-phase heat transfer coefficients $\alpha_{l,0,i}$ and $\alpha_{v,0,i}$ are then calculated for a data point i , assuming that the entire mass flux was present as saturated liquid and saturated vapor, respectively.
- Next, the heat exchanger of data point i is split into a number of $j = 1 \dots N$ sections, each having the same heat load $\dot{Q}_{i,j} = \dot{Q}_i/N$. The mean fluid quality $x_{i,j}$ is calculated for each section, as well as the convective boiling heat transfer coefficient $\alpha_{c,i,j}$. The latter depends on single-phase heat transfer of the saturated phases, the density ratio, and the quality. The same length $L_{i,j} = L/N$ is allocated to each section as a start value. The actual lengths of the sections are calculated later, as they depend on the ratio of mean and local heat transfer coefficients⁹. A typical value of N is 20.
- Based on the section length $L_{i,j}$, the heat flux $\dot{q}_{i,j}$ is calculated for each section. Once the heat flux is known, the nucleate boiling heat transfer coefficient $\alpha_{\text{nb},i,j}$ can be calculated for each section.
- The local flow-boiling heat transfer coefficients $\alpha_{i,j}$ are calculated from the convective boiling and nucleate boiling heat transfer coefficients of each section.
- The mean heat transfer coefficient $\bar{\alpha}_i^*$ of the data set i is numerically integrated.
- The actual section lengths are calculated depending on the ratio of mean and local heat transfer coefficients.
- The integrated length L_i^* is compared to the real length L of the heat exchanger, and iterated until the difference is smaller than a defined numerical accuracy ΔL .
- The entire routine is repeated for $i = 1 \dots M$ data sets.
- The fitting routine *Minuit* minimizes the sum of the squared errors of all M data sets. Free fitting parameters are passed to the function for calculating the local nucleate boiling heat transfer coefficient $\alpha_{\text{nb},i,j}$.

⁹ If the heat transfer coefficient in a section is beyond average, the section must be shorter than average, because both heat load and ΔT are constant in all sections.

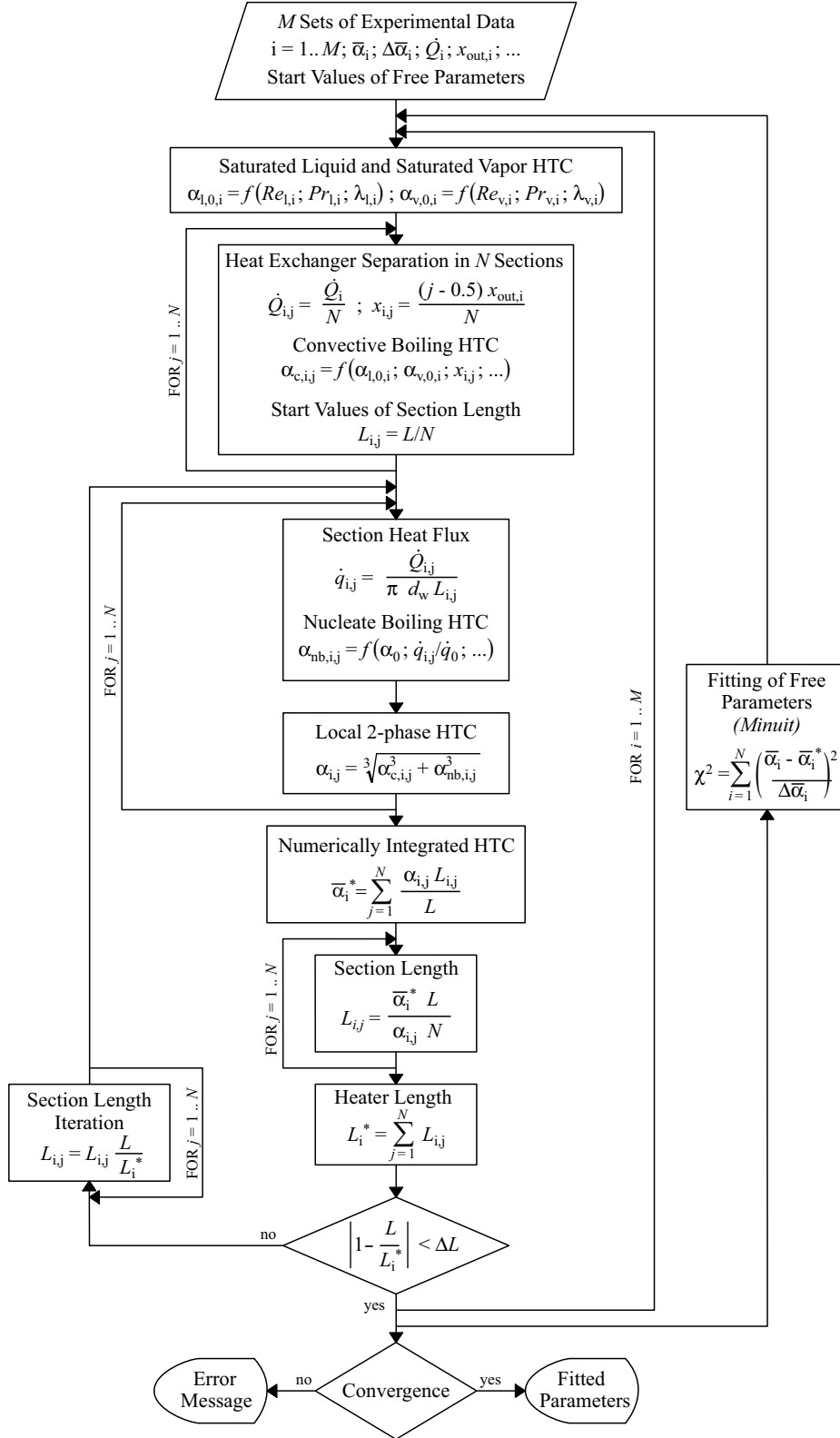


Figure 4.12: Flowchart for Fitting Measured Mean Flow-boiling Heat Transfer Coefficients (HTCs) with Correlation [73] for Local Flow-boiling Heat Transfer

Details of individual equations in the VDI Heat Atlas correlation are discussed together with the experimental results in Section 5.3 and 5.4. The source code of the C++ fitting algorithm is presented in Appendix B.2.

The inlet quality in the test section is kept in a range of $x_{\text{in}} = -5\%$ to -2% to ensure stable operation¹⁰. The slight sub-cooling of the inlet fluid is neglected in the fitting routine, as the single-phase heat transfer coefficient or the length of a single-phase flow section cannot be reliably modeled under these conditions.

In retrospect, the iteration of the section lengths is not required, as the nucleate boiling heat transfer coefficient in microtubes is not significantly influenced by the quality.

¹⁰ Operating conditions, which are too close to the boiling line, lead to oscillations between single- and two-phase flow. The associated change in pressure drop causes instable flow.

5 EXPERIMENTAL RESULTS ON HEAT TRANSFER IN MICROTUBES

The analysis and evaluation of experimental heat transfer data is consistent with the definitions of Section 4, i. e.

- all heat transfer coefficients α are related to the wetted surface A_w ,
- all Nusselt and Reynolds numbers are related to the wetted surface A_w , and
- all velocities w and mass fluxes \dot{M} are calculated with the cross-sectional area A_c .

5.1 Single-phase Heat Transfer

Heat Transfer in Single-phase Turbulent Liquid Flow

Experimental results of single-phase turbulent liquid flow heat transfer measurements are shown in Figure 5.1. The quality of the fits proves that both the turbulent heat transfer model and the concept of measuring the effective thermal resistance R_{eff} are reasonably accurate.

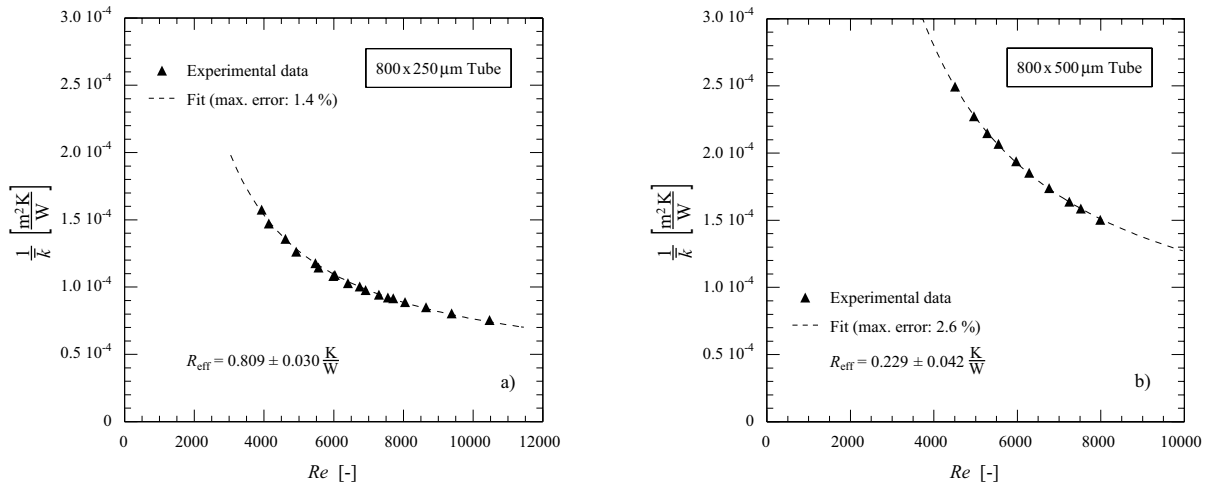


Figure 5.1: Results of Fitting Turbulent Liquid Flow Heat Transfer Data with Eq. (4.20)

The results of the fits are summarized in Table 5.1. The coefficient H1 is a free parameter in the first fit. H1 is then fixed to the fitted value to obtain the error of R_{eff} . ΔR_{eff}

Table 5.1: Fitted Parameters in Single-phase Turbulent Liquid Flow

	800 × 250 μm Tube	800 × 500 μm Tube
Fit Function	$\frac{1}{k} = \frac{d_w}{H0(Re^{H1}-H2) Pr^{0.4}} \frac{1}{1+(\frac{d_w}{L})^{\frac{2}{3}}} \frac{\eta}{\eta_w}^{0.11} \frac{1}{\lambda} + H3 A_w$ Eq. (4.20)	
H0 (fixed)	0.012	
H1	0.904	0.885
H2 (fixed)	280	
H3 (R_{eff})	$0.809 \pm 0.030 \text{ K/W}$	$0.229 \pm 0.042 \text{ K/W}$

is the standard deviation σ of coefficient H3 following Eq. (4.32). It is included in the error analysis as uncorrected systematic error. The effective thermal resistance is mainly determined by the thermal resistances of the stainless steel tube and the solder tin layer, as well as by the contact resistances. R_{eff} is therefore larger for the 800 × 250 μm tube. The influence of R_{eff} increases with the heat transfer coefficient $\bar{\alpha}$, and ranges for all measured data from 0.8 % to 93.8 %. Detailed values are listed for each data point in Appendix C.

The turbulent liquid heat transfer coefficients are plotted together with the conventional correlation Eq. (4.5) in Figure 5.2. The results are similar to the data published by *Adams* et al. [3]. With respect to the conventional correlation, the heat transfer is obviously enhanced with decreasing diameter, which is also seen at the fitted Re exponents H1 in Table 5.1. However, the experimental results of both tubes can be modeled with one equation, if the relative roughness parameter r_d defined in Eq. (4.27) is taken into account.

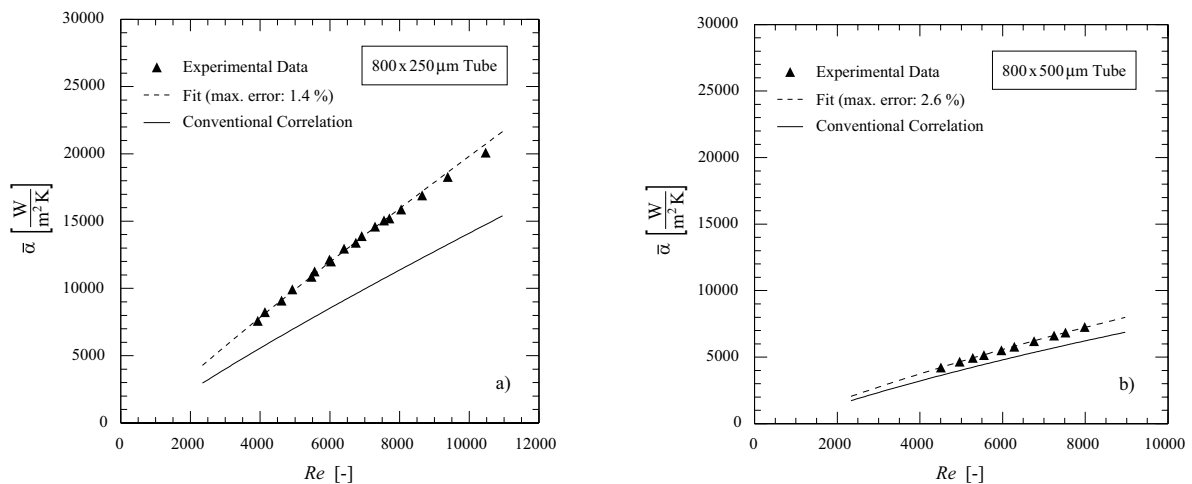


Figure 5.2: Heat Transfer Coefficients in Single-phase Turbulent Liquid Flow

A suitable form to implement r_d is

$$H1 = H1_{\text{smooth}} \cdot r_d^n. \quad (5.1)$$

The fit of coefficient n with the data from both tubes yields

$$Nu_{\text{turb},l} = 0.012 \left[Re^{(0.87 \cdot r_d^{0.22})} - 280 \right] Pr^{0.4} \left[1 + \left(\frac{d_w}{L} \right)^{\frac{2}{3}} \right] \left(\frac{\eta}{\eta_w} \right)^{0.11}. \quad (5.2)$$

The maximum error between measured data and correlation is 1.4 % and 2.6 %, respectively. One can therefore conclude that the enhancement of heat transfer is only due to the relative roughness r_d , and not due to a diameter dependence specific to microtube dimensions. Eq. (5.2) is fully consistent with the turbulent heat transfer correlation Eq. (4.5) for smooth circular tubes.

Heat Transfer in Single-phase Turbulent Vapor Flow

The measured turbulent heat transfer coefficients in the vapor phase are shown in Figure 5.3. The trend in Figure 5.3b shows similar behavior as liquid phase data. The results for the $800 \times 250 \mu\text{m}$ tube, however, do not comply with the trend of the correlations.

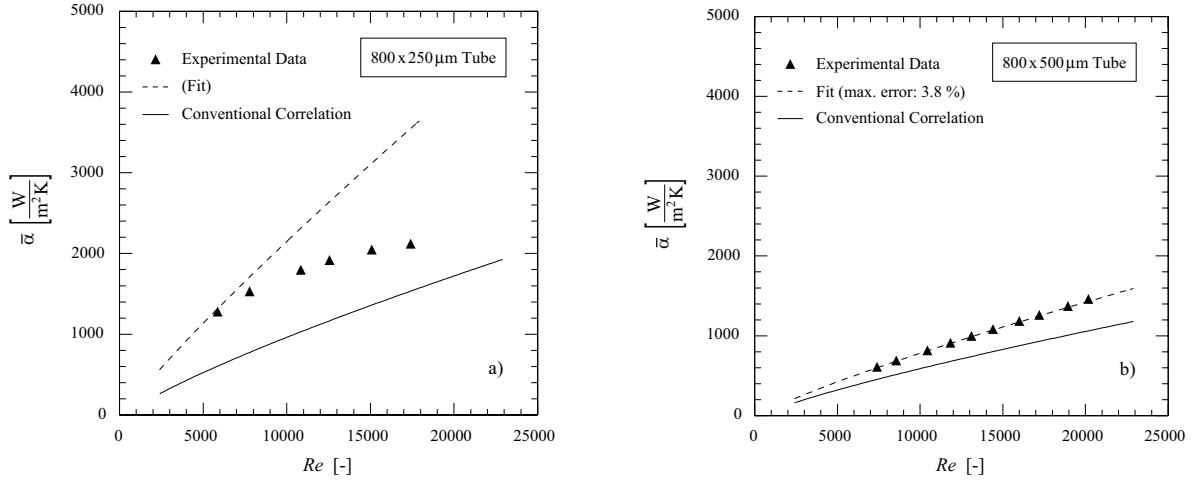


Figure 5.3: Heat Transfer Coefficients in Single-phase Turbulent Vapor Flow

This deviation is believed to be due to systematic errors in the experiments, as vapor phase measurements were not a major objective in the system design. Possible reasons for the deviations are:

- The major problem is that the pressure in the test section is not precisely known, as it is only measured far upstream. The correction with a pressure drop correlation is uncertain.

- The pressure drop in the $800 \times 250 \mu\text{m}$ tube compared to the $800 \times 500 \mu\text{m}$ tube is roughly twice as high at the same Reynolds number (see Table 2.5 in the discussion on scaling). This implies also that the pressure drop in the test section itself becomes significant. The assumption of incompressible flow with mean fluid properties may therefore not be valid.
- In addition, data in Figure 5.3a were taken in a power-on/power-off mode between the data points, whereas data in the $800 \times 500 \mu\text{m}$ tube were taken at a step-wise ramping of the heater power. Low heat transfer coefficients together with a low capacity flux caused a very slow response of the system. This may have resulted in a slow shift of operating conditions.

Clearly, there is no reason to believe in fundamental differences between turbulent liquid and turbulent vapor phase heat transfer. Only experimental data of the $800 \times 500 \mu\text{m}$ tube are therefore fitted with the type of Eq. (5.1), yielding the turbulent vapor heat transfer correlation

$$Nu_{\text{turb,v}} = 0.0214 \left[Re^{(0.8 \cdot r_d^{0.55})} - 100 \right] Pr^{0.4} \left[1 + \left(\frac{d_w}{L} \right)^{\frac{2}{3}} \right]. \quad (5.3)$$

Eq. (5.3) matches at least low Reynolds number data in Figure 5.3a, where the pressure drop is less significant. The correlation is consistent with the conventional correlation Eq. (4.5) for turbulent vapor heat transfer in smooth circular tubes. Nevertheless, more statistics of dedicated experiments is required to generally validate Eq. (5.3).

Heat Transfer in Single-phase Laminar Liquid Flow

The experimental results shown in Figure 5.4 were already presented in Figure 4.11 for the discussion of characteristic dimensions. At low Re , i. e. large values of the reduced length

$$L^* = \frac{L}{Re Pr d_w}, \quad (5.4)$$

the data fit well with $Nu_\infty = 3.656$ for fully developed flow. In the entry region, however, the heat transfer is superior to the conventional correlation Eq. (4.3). This is explained with the distortion or breakage of boundary layers by the surface roughness.

The results of the fits are summarized in Table 5.2. Unlike in turbulent flow, the data cannot be modeled yet with one correlation. The intersection of the fit functions with the ordinate yields values of $\overline{Nu} \approx 10$ for both tubes. However, there should be a larger difference, considering the relative roughness parameters of $r_d = 1.20$ and $r_d = 1.07$, respectively. The reason for this inconsistency may be seen in the choice of the characteristic diameter for Re and L^* . It was already shown in Figure 4.11b that the difference in the fit functions increases at $Re = f(d_c)$. One may therefore suppose that still a smaller diameter d_{lam} is needed as reference for Re . It would be interesting to

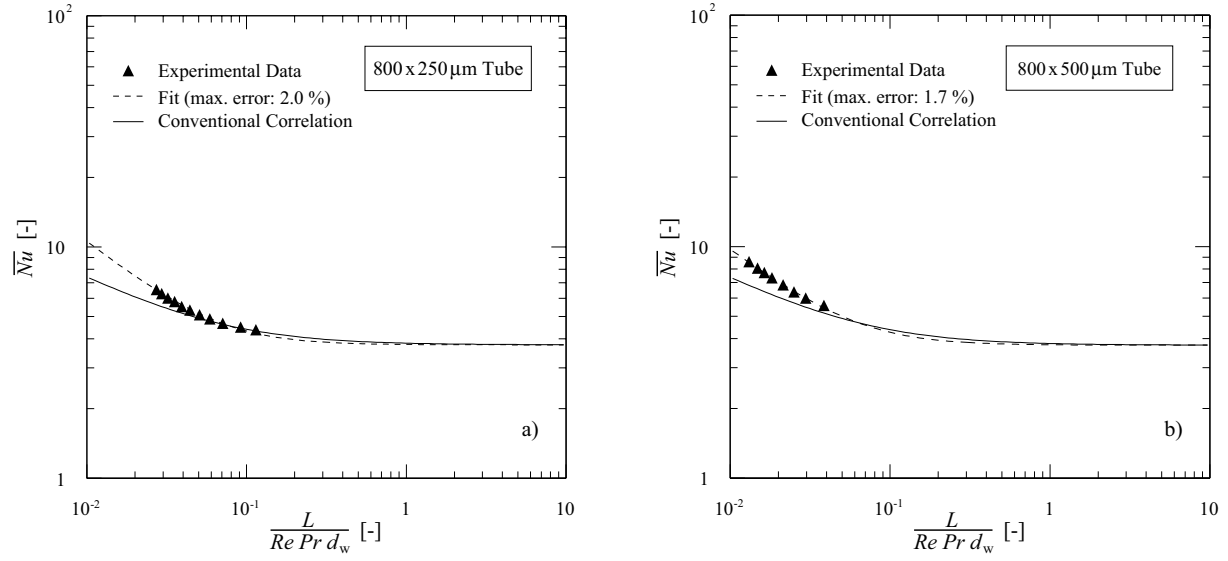


Figure 5.4: Nusselt Numbers in Single-phase Laminar Liquid Flow

Table 5.2: Fitted Parameters in Single-phase Laminar Liquid Flow

	800 × 250 μm Tube	800 × 500 μm Tube
Fit Function	$\overline{Nu}_{lam,l} = \left[\left(\frac{a}{1-n} \left(\frac{Re Pr d_w}{L} \right)^n \right)^3 + Nu_\infty^3 \right]^{\frac{1}{3}} \left(\frac{\eta}{\eta_w} \right)^{0.14}$ Eq. (4.3)	
a	0.391	0.421
n	0.538	0.515
Nu_∞ (fixed)	3.656	

verify whether d_{lam} coincides with the laminar diameter obtained from pressure drop measurements, following

$$d_{lam} \equiv d_h = \sqrt{\frac{128 \eta L \dot{V}}{\Delta p \pi d_c^2}}. \quad (5.5)$$

If such a relation was found, a suitable mathematical form to implement the relative roughness r_d in Eq. (4.3) would be

$$\overline{Nu} = \left[\left(\frac{a}{1-\frac{n}{x}} \left(\frac{Re Pr d}{L} \right)^{n-x} \right)^3 + Nu_\infty^3 \right]^{\frac{1}{3}} K_T, \quad \text{with} \quad x = r_d^y. \quad (5.6)$$

Measured and modeled mean heat transfer coefficients $\bar{\alpha}$ are shown in Figure 5.5 as a function of the Reynolds number. The trend of good agreement between data and conventional correlation at low Re , and increasing positive deviations with increasing Re , is similar to the data published by *Rahman* [65].

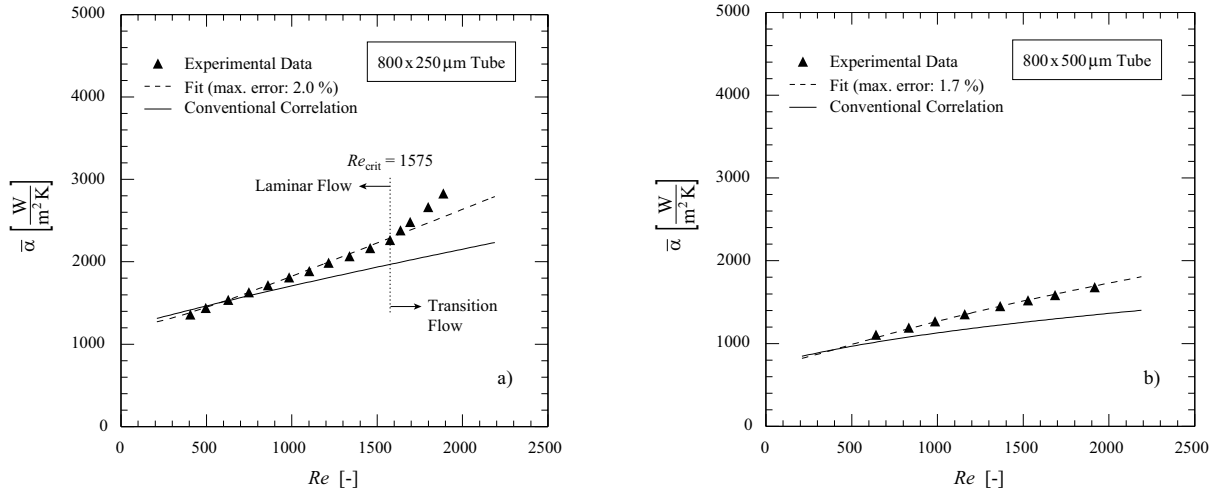


Figure 5.5: Heat Transfer Coefficients in Single-phase Laminar Liquid Flow

The flow transition from laminar to turbulent flow can be clearly identified in Figure 5.5a, with $Re_{\text{crit}} = 1575 \ll 2300$. The value of the critical Reynolds number may still change depending on the chosen reference diameter for the Reynolds number, but it can only change towards smaller values as d_w is certainly the largest characteristic diameter for a rough tube. Unfortunately, the flow transition could not be measured in the $800 \times 500 \mu\text{m}$ tube, because the test stand could not be operated with higher flow rates in laminar flow.

5.2 Conclusions from Single-phase Heat Transfer Measurements

The following conclusions can be derived from the single-phase heat transfer measurements:

- There is no physical difference in heat transfer mechanisms between macro- and micro-tubes.
- The enhancement of heat transfer coefficients in small tubes compared to conventional correlations is explained with the increased influence of roughness, i. e. the relative increase of the wetted surface compared to the volume. In laminar flow, the breakage of boundary layers on asperities improves the heat transfer in the entry region.
- The enhancement of surface effects in tubes with large relative roughness can be modeled with the relative roughness parameter r_d defined in Eq. (4.27).
- Beyond heat transfer in microtubes, the parameter r_d might be suitable to model the improvement of heat transfer in so-called *enhanced surface tubes* in first order¹.

¹ A second order effect is e. g. superimposed rotation.

5.3 Flow-boiling/Convective Boiling Heat Transfer

The local flow-boiling heat transfer coefficient α is calculated in the *VDI Heat Atlas* correlation [73] as a function of the local convective heat transfer coefficient α_c and the local nucleate boiling heat transfer coefficient α_{nb} :

$$\alpha = \sqrt[3]{\alpha_c^3 + \alpha_{nb}^3} . \quad (5.7)$$

If nucleate boiling occurs, it usually dominates flow-boiling heat transfer, and the quality of modeling α_{nb} described in Section 5.4 is therefore important.

Convective boiling conditions occur at low heat flux, where the wall superheat is too small for the activation of nucleation centers. Evaporation takes place at the liquid/vapor phase boundary. Convective boiling heat transfer depends mainly on the mass flux \dot{M} , the quality x , and the density ratio ρ_l/ρ_v . Correlations are usually based on single-phase heat transfer. The VDI Heat Atlas correlation [73] for convective boiling in vertical tubes² has the form

$$\frac{\alpha_c}{\alpha_{1,0}} = \left\{ (1-x)^{0.01} \left[(1-x)^{1.5} + 1.9 x^{0.6} \left(\frac{\rho_l}{\rho_v} \right)^{0.35} \right]^{-2.2} + x^{0.01} \left[\frac{\alpha_{v,0}}{\alpha_{1,0}} \left(1 + 8 (1-x)^{0.7} \left(\frac{\rho_l}{\rho_v} \right)^{0.67} \right) \right]^{-2} \right\}^{-0.5} . \quad (5.8)$$

$\alpha_{1,0}$ and $\alpha_{v,0}$ are local single-phase heat transfer coefficients, calculated for the case that the fluid was flowing at the same mass flux in form of saturated liquid and saturated vapor, respectively.

Convective boiling heat transfer plays a minor role in most flow-boiling heat transfer conditions under high heat flux. Nevertheless, the experimental data summarized in Figure 5.6 were taken to verify whether Eq. (5.8) could be used in the overall flow-boiling heat transfer Eq. (5.7).

The results for the $800 \times 500 \mu\text{m}$ tube in Figure 5.6b³ are in very good agreement with the correlation Eq. (5.8). This is remarkable, as the single-phase heat transfer coefficients $\alpha_{1,0}$ and $\alpha_{v,0}$ were calculated with Eq. (5.2) and Eq. (5.3), respectively. In the $800 \times 250 \mu\text{m}$ tube, the agreement between experiment and correlation is within 10% for the data series of $\dot{M} = 530 \text{ kg/m}^2\text{s}$. At higher mass flux, however, the correlation over-predicts experimental data by up to 60%. This may be due to the uncertainty in the vapor phase heat transfer coefficient $\alpha_{v,0}$, which influences the slope of the function at increasing quality.

It is certainly not justified to fit some of the 9 adjustable parameters of Eq. (5.8) with the few experimental data to receive a better representation for the $800 \times 250 \mu\text{m}$ tube.

² The reason why the correlation for vertical tubes is used is explained in the discussion on nucleate boiling in Section 5.4.

³ Unfortunately, it was not possible to take data at higher quality, because the pre-heater was partially burned during the adjustment of data points, and consequently lost a major fraction of its power.

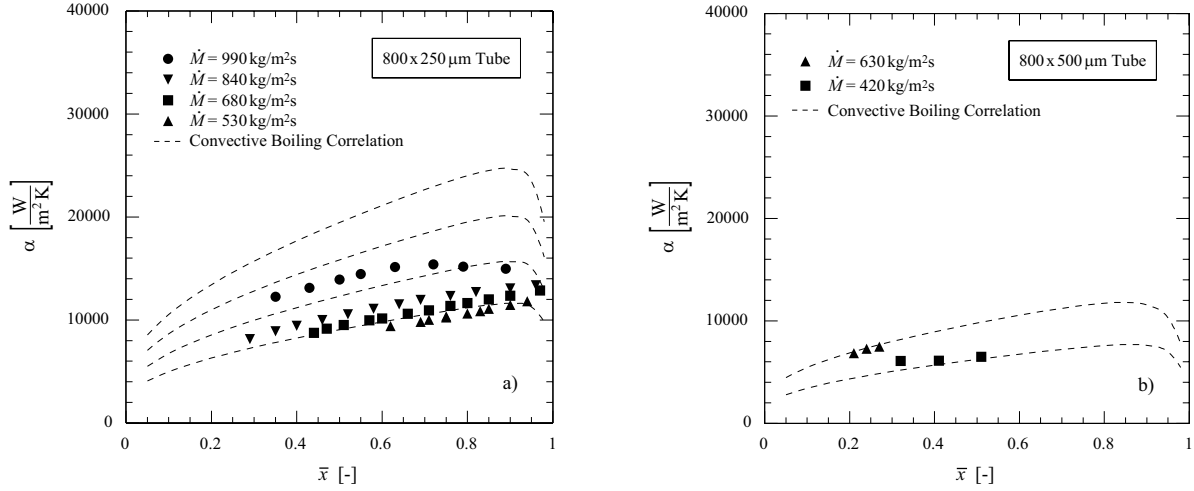


Figure 5.6: Results of Convective Boiling Heat Transfer Measurements

On the contrary, the excellent agreement shown in Figure 5.6b suggests that Eq. (5.8) is valid in the range of the tube diameters investigated here. The correlation is therefore used unchanged for modeling flow-boiling heat transfer coefficients with Eq. (5.7).

5.4 Nucleate Boiling

For the analysis of α_{nb} with the method described in Section 4.5 only data were selected, where the heat flux was higher than required for the onset of nucleate boiling, and lower than the critical heat flux for dryout ($\dot{q}_{onb} \leq \dot{q} \leq \dot{q}_{crit}$). In the experiments dominated by nucleate boiling, the fluid was always entering the test section in the liquid phase close to saturation ($x_{in} \approx -0.05$). A heat flux $\dot{q} \geq \dot{q}_{onb}$ was then needed to generate two-phase flow. At the lower limit of \dot{q} , experiments were conducted with a heat flux just high enough for stable two-phase operation. This was usually obtained at outlet qualities of $x_{out} = 0.10$ – 0.20 . The start of dryout was seen in the data series of mean heat transfer coefficients, when data points of higher heat flux fell below the *trend* of low heat flux data.

The measured temperature differences as a function of heat load are plotted in Figure 5.7 for all experiments carried out in the nucleate boiling dominated regime. The data are correlated with the nucleate boiling heat transfer model in [73], which has the general form

$$\frac{\alpha_{nb}}{\alpha_0} = C_F \left(\frac{\dot{q}}{\dot{q}_0} \right)^n F(p^*) F(d) F(W) F(\dot{M}, x). \quad (5.9)$$

α_0 is the reference heat transfer coefficient in pool boiling at the heat flux \dot{q}_0 . For argon these values are

$$\begin{aligned} \alpha_0 &= 3870 \text{ W/m}^2\text{K}, \quad \text{at} \\ \dot{q}_0 &= 10000 \text{ W/m}^2. \end{aligned}$$

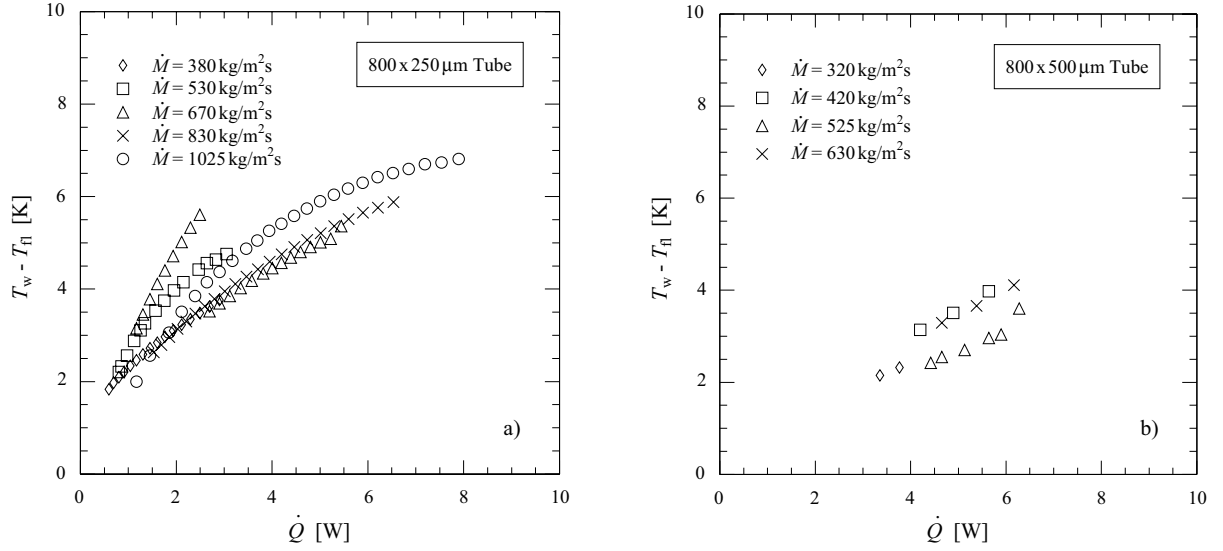


Figure 5.7: Summary of Measured Temperature Differences in Nucleate Boiling Heat Transfer

The fluid properties are considered by the factor C_F , wall properties by a factor $F(W)$, tube dimensions by a factor $F(d)$ and flow conditions by a factor $F(\dot{M}, x)$. The influence of the saturation pressure is included in $F(p^*)$, and the heat flux dependence is described by the power function $(\dot{q}/\dot{q}_0)^n$. The influence of these factors and the relevance of their description in [73] for flow-boiling heat transfer in microtubes is now discussed on the basis of the experimental results. Individual effects are discussed first, before the complete function is presented that is used for fitting the data.

Flow- and Heat Transfer Regimes

Before modeling flow-boiling heat transfer coefficients one has to be aware that several flow regimes may occur, which are related to the phase distribution in the tube. A number of methods for predicting flow regimes in tubes can be found in the literature [75], [30], [73], [83]. *Ghiaasiaan* [23] published studies on flow patterns in microtubes, but found generally poor agreement with conventional models. He points out that stratified flow is essentially absent due to the influence of surface tension. *Kandlikar* [41] summarized a number of publications on mini-/microchannel flow patterns and own experimental data. He identifies three commonly encountered flow patterns in minichannels, which are called isolated bubble, confined bubble (or plug/slug) and annular flow. At present, the literature on microchannel flow patterns is considered insufficient to draw any generalized conclusion.

So far, a systematic influence of flow regimes on heat transfer is only confirmed for operating conditions with significant phase separation and partial surface dryout. As such conditions are unlikely in microtubes, and as the modeling of flow regimes in tubes with large roughness is uncertain, flow patterns are not discussed in further detail.

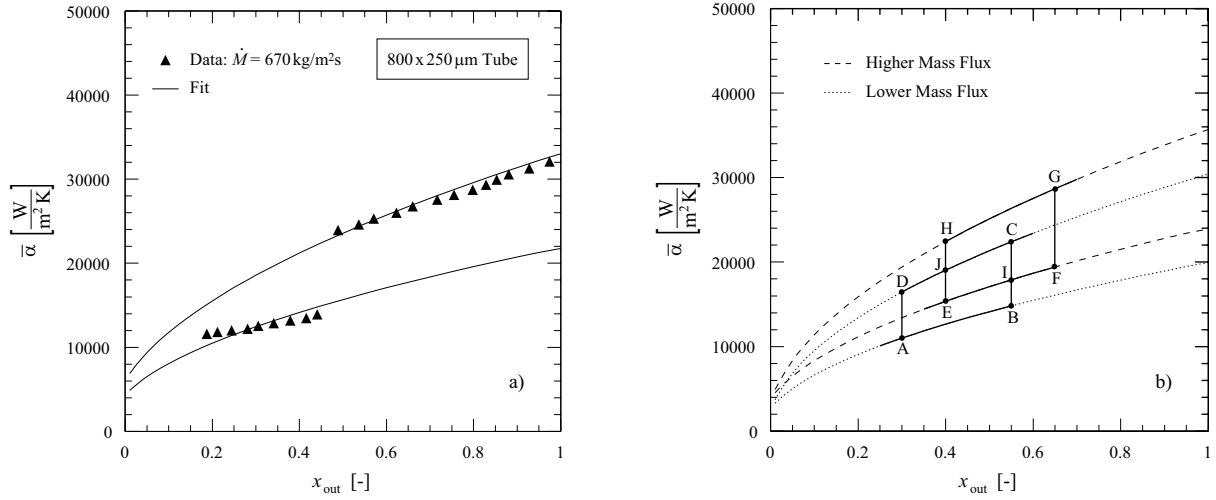


Figure 5.8: Variation of Flow- and Heat Transfer Regimes in Two-phase Flow. a) Measured Mean Heat Transfer Coefficients between $x_{\text{in}} = -0.05$ and x_{out} , $800 \times 250 \mu\text{m}$ Tube b) Seemingly Inconsistent Results Related to Hysteresis

However, the flow regime can still have a significant influence on heat transfer, which is shown in Figure 5.8 a. The data points represent mean heat transfer coefficients $\bar{\alpha}$ between $x_{\text{in}} = -0.05$ and x_{out} , taken at a constant mass flow and with a step-wise increase of the heat load. At about $x_{\text{out}} = 0.45$, the mean heat transfer coefficient increases by 70 % at just a slight increase of the heat load and the outlet quality. Such a step in the *mean* heat transfer coefficient can only be explained, if the *entire* flow and heat transfer regime in the heat exchanger changes. A consequence is then that flow regimes do not only depend on local conditions, but can be influenced by retroactive effects.

Experimental results suggest that flow regimes can be meta-stable, which means that there is certainly hysteresis in the flow transition. The hysteresis can lead to *seemingly* inconsistent results, which is shown in Figure 5.8 b. In the *Lower Mass Flux* regime, the heat transfer coefficient may take values in the hysteresis area of either between (A-B), or between (C-D), depending on the *history* of the flow. In the *Higher Mass Flux* regime, heat transfer coefficients are possible between (E-F) and (G-H). The overlap of hysteresis areas allows data points between (J-C) and (E-I), yielding lower heat transfer coefficients for the higher mass flux and heat flux data.

Such *seemingly* inconsistent data were obtained in the experiments, shown in Figure 5.9. The two data series in Figure 5.9 a, and the two data series in Figure 5.9 b were each taken one after another in the same experimental session. They are in itself consistent, as higher heat transfer coefficients were measured for higher heat and mass fluxes. However, the data series of $\dot{M} = 525 \text{ kg/m}^2\text{s}$ in Figure 5.9 b shows lower heat transfer coefficients than the $\dot{M} = 320 \text{ kg/m}^2\text{s}$ series in Figure 5.9 a. The differences between Figure 5.9 a and 5.9 b are about 20 %, which is beyond statistical errors of the measurements. One can therefore conclude that the variations concern the heat transfer itself, related to flow profiles, hysteresis, and to the history of the flow.

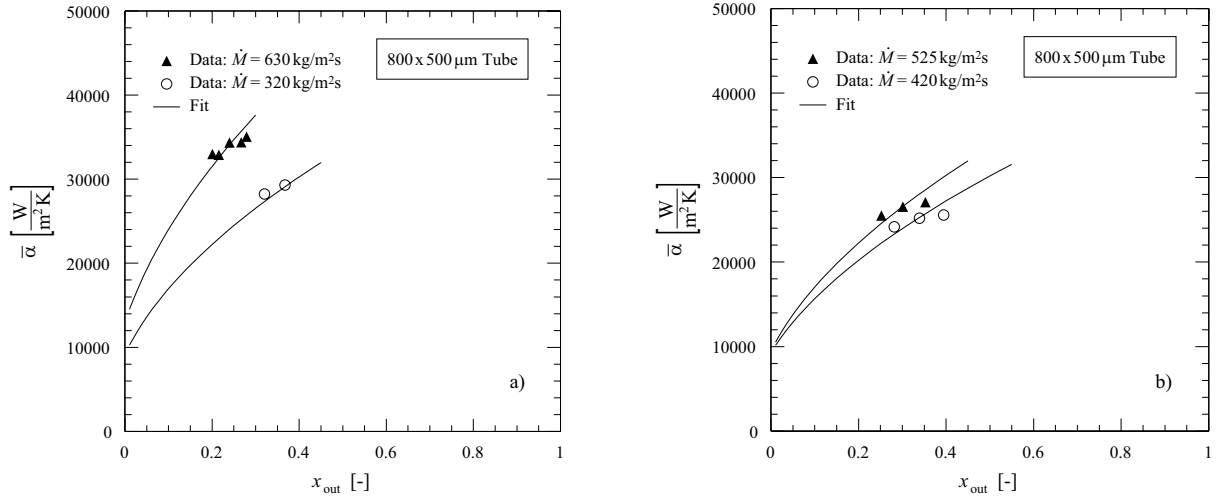


Figure 5.9: Consistent and *Seemingly* Inconsistent Mean Heat Transfer Coefficients Measured in the $800 \times 500 \mu\text{m}$ Tube.

Although not proven optically in the experiments, one can well imagine that meta-stable flow regimes and different heat transfer levels are associated with the *number of active nucleation centers*, which is not necessarily always the same under reproduced operating conditions. Flow-boiling heat transfer correlations therefore have rather large uncertainties. The standard deviation between the correlation and data from an experimental database is given in [73] for a number of fluids, ranging from $\pm 4\%$ to $\pm 96\%$. High statistics is consequently required to understand the difference between intrinsic heat transfer variations and systematic effects that can be modeled.

Heat Flux and Mass Flux Dependence

The *VDI Heat Atlas* correlation distinguishes between vertical and horizontal tubes. The nucleate boiling heat transfer coefficient is independent of mass flux and quality in vertical tubes, whereas α_{nb} improves with \dot{M} and declines with x in horizontal tubes. This behavior is related to phase separation and partial surface wetting.

Fitting of experimental data in Figure 5.9 and Figure 5.10⁴ shows that there is no mass flux and quality dependence in these microtubes, although they are installed in a horizontal sense. This result is explained by a stronger influence of the surface tension in microtubes, which makes phase separation phenomena less likely to occur. Differences between the data series in each plot are only due to higher heat fluxes at higher flow rates.

As the tube orientation has obviously no significant influence on nucleate boiling heat transfer in microtubes, the modeling of α_{nb} is based on the *VDI Heat Atlas* correlation for *vertical* tubes. The heat flux exponent n is a function of the reduced pressure, and yields for cryogenic fluids [73]:

⁴ The $\dot{M} = 670 \text{ kg/m}^2\text{s}$ data are identical with the higher values in Figure 5.8 a.

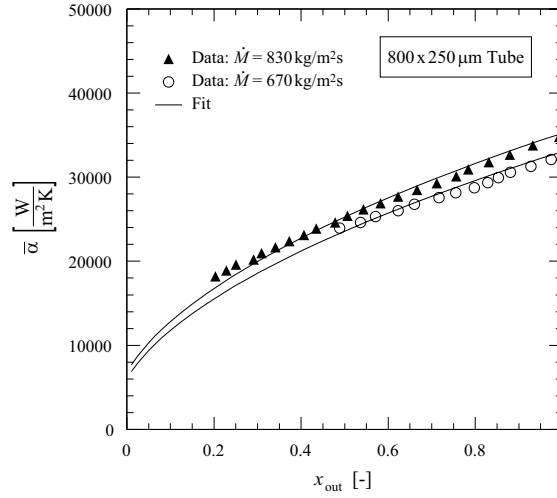


Figure 5.10: Heat Flux and Mass Flux Dependence of Mean Heat Transfer Coefficients, $800 \times 250 \mu\text{m}$ Tube.

$$n = 0.7 - 0.13 \cdot 10^{0.48 p^*} . \quad (5.10)$$

The factor $F(\dot{M}, x)$ is

$$F(\dot{M}, x) = 1 . \quad (5.11)$$

All the experimental data presented in this Section are fitted with these n and $F(\dot{M}, x)$ as constants. The excellent agreement between data points and fit in Figure 5.10 proves that the heat flux dependence is well described with Eq. (5.10). Here one has to point out, that the fit of the measured *mean* heat transfer coefficients is a result of the heat exchanger modeling with numerical integration of the (modeled) *local* heat transfer coefficients. The agreement between fit and data in *each* point therefore means that the entire model is consistent between $x_{\text{in}} = 0$ and the x_{out} of that point.

Saturation Pressure Dependence $F(p^*)$

The influence of the saturation pressure on nucleate boiling heat transfer is described in [73] by the function

$$F(p^*) = 2.816 p^{*0.45} + \left(3.4 + \frac{1.7}{1 - p^{*7}} \right) p^{*3.7} , \quad (5.12)$$

where $p^* = p_s/p_c$ is the reduced pressure calculated from the saturation pressure p_s and the critical pressure p_c . As fluid properties are independent of scaling, the function is used without modification.

Influence of Wall Properties $F(W)$

Although the effect of surface properties is not known in detail, the influence of roughness is taken into account in [73] by the function

$$F(W) = \left(\frac{R_a}{R_{a,0}} \right)^{0.133}, \quad \text{with } R_{a,0} = 1 \mu\text{m}. \quad (5.13)$$

A difficulty in using Eq. (5.13) is to determine the arithmetic mean roughness R_a of the microtubes used in the experiments. From the microscope images values of

$$\begin{aligned} R_a &= 9 \mu\text{m} \quad (800 \times 250 \mu\text{m tube}), \\ R_a &= 7 \mu\text{m} \quad (800 \times 500 \mu\text{m tube}) \end{aligned}$$

were estimated. This yields factors of $F(W) = 1.34$ and $F(W) = 1.30$, respectively.

Diameter Dependence $F(d)$

The factor $F(d)$ in [73] describes the increase of heat transfer at decreasing diameter:

$$F(d) = \left(\frac{d_0}{d} \right)^{0.4}, \quad \text{with } d_0 = 0.01 \text{ m}. \quad (5.14)$$

This effect can be explained by the increasing surface to volume ratio A/V in small tubes (see discussions on scaling in Section 2.3), which is weighted with an exponent of 0.4:

$$\frac{A}{V} = \frac{4}{d} \quad \text{in smooth circular tubes}, \quad (5.15)$$

$$\left(\frac{A/V}{A_0/V_0} \right)^{0.4} = \left(\frac{d_0}{d} \right)^{0.4}. \quad (5.16)$$

The surface to volume ratio in rough tubes with characteristic diameters d_w and d_c is

$$\frac{A}{V} = \frac{4 d_w}{d_c^2}, \quad (5.17)$$

or with the relative roughness r_d defined in Eq. (4.27)

$$\frac{A}{V} = \frac{4 r_d}{d_c}. \quad (5.18)$$

Redefining $F(d)$ for rough tubes then yields

$$F(d) = \left(\frac{d_0 r_d}{d_c} \right)^{0.4}. \quad (5.19)$$

Applying the definitions of Eq. (5.10), (5.11), (5.12), (5.13) and (5.19), the nucleate boiling heat transfer model of Eq. (5.9) becomes

$$\frac{\alpha_{z,nb}}{\alpha_0} = C_F^* \left(\frac{\dot{q}}{\dot{q}_0} \right)^n \left[2.816 p^{*0.45} + \left(3.4 + \frac{1.7}{1 - p^{*7}} \right) p^{*3.7} \right] \left(\frac{d_0 r_d}{d_c} \right)^{0.4} \left(\frac{R_a}{R_{a,0}} \right)^{0.133}. \quad (5.20)$$

All the data series can be fitted with this equation, keeping only the factor C_F^* as a free parameter. The results of these fits are shown in Figure 5.11 and Figure 5.12. *Blank* symbols are data with local dryout toward the end of the heat exchanger. These data are not considered in the modeling. The effect of film boiling is discussed in Section 5.5. Experimental data in Figure 5.11 c and Figure 5.11 d are identical with data in Figure 5.9 a and Figure 5.10, respectively. Data presented in Figure 5.9 are contained in Figure 5.12.

A summary of the fitted parameters C_F^* and their goodness of fit χ^2 are shown in Table 5.3. The goodness of fit is defined as

$$\chi^2 = \sum_{i=1}^N \frac{(\bar{\alpha} - \bar{\alpha}_{\text{fit}})^2}{\Delta \bar{\alpha}^2}, \quad (5.21)$$

meaning that χ^2 should be around N . In general, too large χ^2 signify underestimated errors $\Delta \bar{\alpha}$, whereas too small χ^2 indicate overestimated errors or specially selected data. In the context of intrinsic variations in nucleate boiling heat transfer, however, χ^2 cannot be regarded strictly as a measure of the error estimation and the correctness of the fit function.

Table 5.3: Summary of Fitted Coefficients C_F^* Using Eq. (5.20)

Tube	Data Series	N Data Points	C_F^*	χ^2
$800 \times 250 \mu\text{m}$ $F(d) = 4.47$	$\dot{M} = 380 \text{ kg/m}^2\text{s}$	16	0.19	7.3
	$\dot{M} = 530 \text{ kg/m}^2\text{s}$	14	0.15	58.8
	$\dot{M} = 670 \text{ kg/m}^2\text{s}$	9	0.12	138.4
	$\dot{M} = 670 \text{ kg/m}^2\text{s}$	13	0.19	17.3
	$\dot{M} = 830 \text{ kg/m}^2\text{s}$	22	0.18	72.9
	$\dot{M} = 1025 \text{ kg/m}^2\text{s}$	24	0.15	283.9
	Mean		0.16 ± 0.03	
$800 \times 500 \mu\text{m}$ $F(d) = 3.27$	$\dot{M} = 320 \text{ kg/m}^2\text{s}$	2	0.39	0.1
	$\dot{M} = 420 \text{ kg/m}^2\text{s}$	3	0.29	2.5
	$\dot{M} = 525 \text{ kg/m}^2\text{s}$	3	0.29	2.5
	$\dot{M} = 630 \text{ kg/m}^2\text{s}$	1	0.31	–
	$\dot{M} = 630 \text{ kg/m}^2\text{s}$	5	0.37	3.0
	Mean		0.33 ± 0.05	

Although there is only limited statistics, one can see a significant difference in the factors C_F^* between the two tubes. The $800 \times 250 \mu\text{m}$ tube reveals lower heat transfer coefficients,

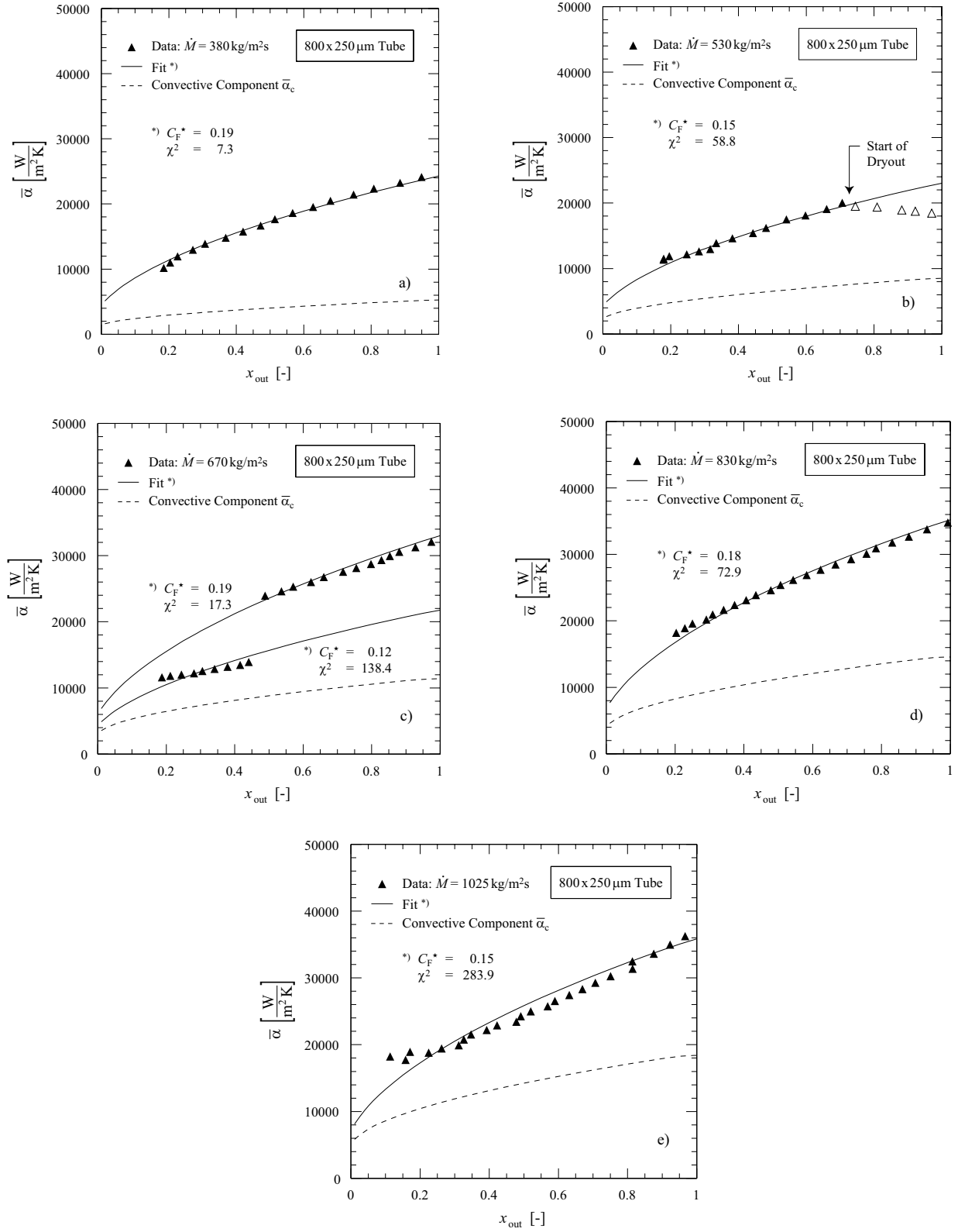


Figure 5.11: Summary of Measured and Fitted Mean Flow-boiling Heat Transfer Coefficients between $x_{in} = -0.05$ and x_{out} in the 800 x 250 μm Tube.

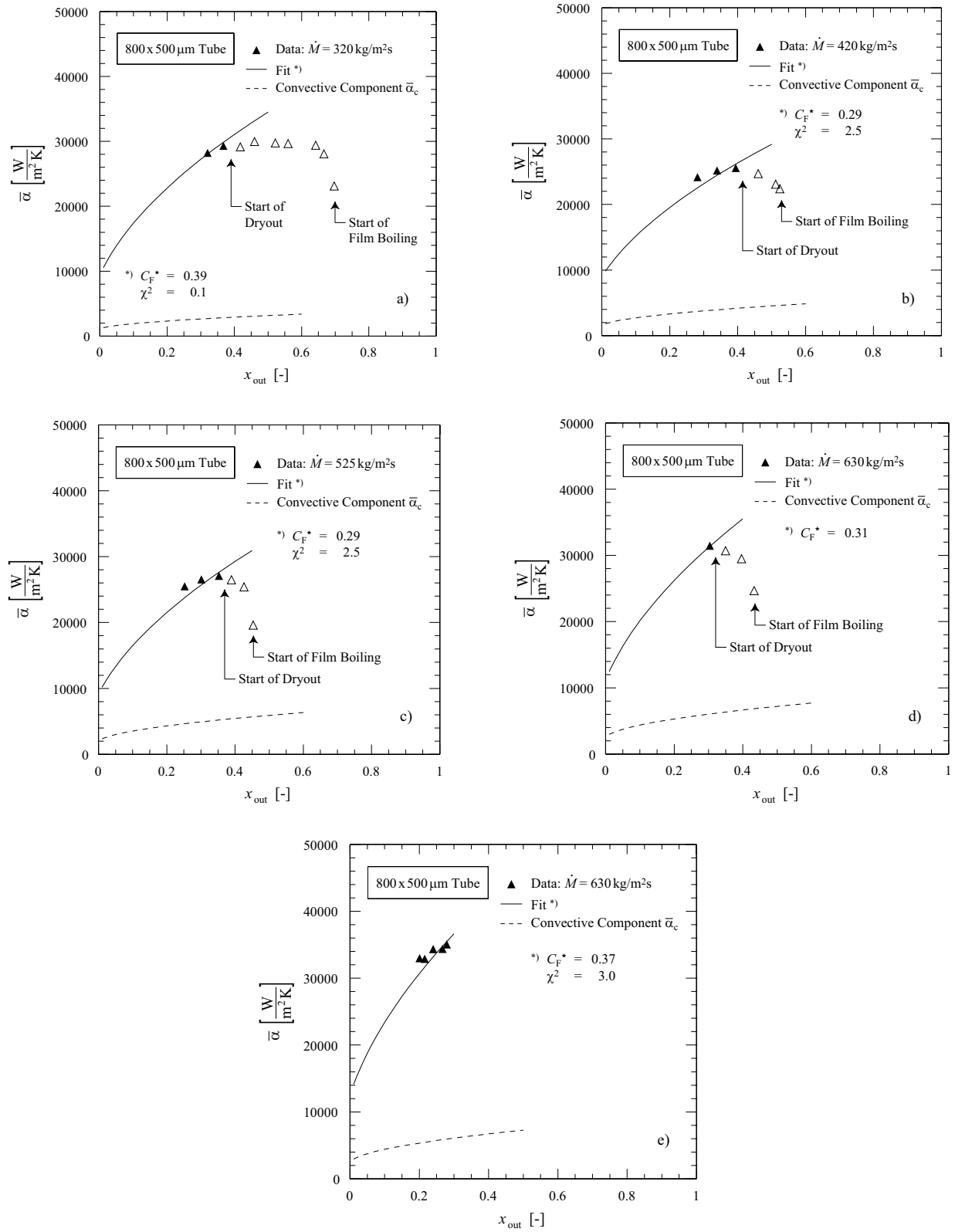


Figure 5.12: Summary of Measured and Fitted Mean Flow-boiling Heat Transfer Coefficients between $x_{in} = -0.05$ and x_{out} in the $800 \times 500 \mu\text{m}$ Tube.

which contradicts common behavior in large tubes and the definition of the diameter dependence $F(d)$. This inverse trend could even not be explained, if the diameter dependence were set to $F(d) = 1$ in either case. Moreover, all values of C_F^* fall below the fluid-specific constant $C_F = 0.93$, which is given in [73] for argon with a standard deviation of ± 0.34 . One can therefore conclude that Eq. (5.19) is incomplete.

It has been shown so far that, with the exception of the diameter dependence, nucleate boiling heat transfer in microtubes can be quite well modeled with the *VDI Heat Atlas* correlation for vertical tubes, suggesting that there is no fundamental difference at this size of tubes. To be fully consistent between this correlation and the experimental results, an extension of the parameter $F(d)$ is proposed. This extension, however, must be based on some assumptions and mathematical concepts, as modeling with experimental results of only two microtube diameters is uncertain.

One may assume that the limitation of nucleate boiling heat transfer in microtubes is somehow associated with the ratio of tube and bubble volume. The equilibrium of a spherical liquid-vapor bubble interface requires [30]

$$T_v = T_l, \quad (5.22)$$

$$\mu_v = \mu_l, \quad (5.23)$$

$$p_v - p_l = \frac{2\sigma}{r}. \quad (5.24)$$

T_v and T_l are the vapor and liquid phase temperatures, μ_v and μ_l are the chemical potentials, and p_v and p_l are the vapor and liquid pressures on either side of the interface. σ is the surface tension, and r is the radius of the interface. The superheat needed for an equilibrium bubble of radius r can be approximated as [30]

$$T = \frac{T_s}{1 - \frac{2\sigma \rho_l}{\Delta h_{lv} r \rho_v (\rho_l - \rho_v)}}, \quad (5.25)$$

where T_s is the saturation temperature, Δh_{lv} is the latent heat, and ρ_l and ρ_v are the densities of the liquid and the vapor phase. Nuclei of radius greater than r from Eq. (5.25) become bubbles and grow; those of smaller radius collapse [30]. For argon at a saturation temperature of 124 K this radius is as small as $r = 0.12 \mu\text{m}$ at 1 K superheating. One can therefore conclude that there is no physical limit of nucleate boiling in microtube dimensions, which are of interest for practical applications. This statement is coherent with observations made by *Zhang* [87], who visualized bubble growth from smaller than $10 \mu\text{m}$ diameter to departure sizes of $50\text{--}100 \mu\text{m}$ diameter.

As a result, one may conclude that the confinement of *bubble growth* is a limiting factor of nucleate boiling heat transfer, rather than the amount of superheating or the bubble formation itself. The effect should then depend on the ratio of tube diameter to departure diameter of bubbles, e. i. the degree of turbulence or slip caused by bubbles departing from the wall.

A number of correlations for calculating the departure diameter of bubbles use the Laplace

constant \mathcal{L} as a basis [30], [23]

$$\mathcal{L} = \sqrt{\frac{\sigma}{g (\rho_l - \rho_v)}} . \quad (5.26)$$

Although the departure diameter in a tube may rather depend on drag forces than on buoyancy, the Laplace constant is proposed here for simplicity. For argon with a saturation temperature of $T_s = 124 \text{ K}$ it has a value of $\mathcal{L} = 630 \mu\text{m}$.

Considering common trends in tubes described by Eq. (5.14), a phenomenon is to be modeled that only becomes effective in small tubes, i. e. where the tube diameter is in the range or below the value of \mathcal{L} . A so-called *saturation function* of the form

$$F_b = 1 - e^{-c \frac{d_c}{\mathcal{L}}} \quad (5.27)$$

is therefore suitable. The exponential function F_b with the ratio d_c/\mathcal{L} related to tube and bubble volume can take values between 0 and 1, if the coefficient c is positive. Fitting all experimental data with this expression while fixing C_F to 0.93 yields a diameter dependence of

$$F(d) = \left(\frac{d_0 r_d}{d_c} \right)^{0.4} \left(1 - e^{-0.45 \frac{d_c}{\mathcal{L}}} \right) . \quad (5.28)$$

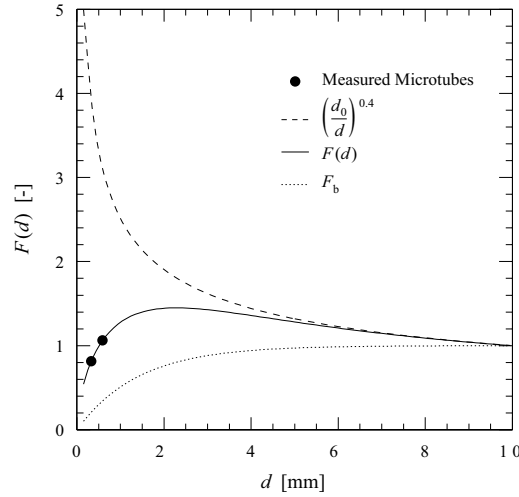


Figure 5.13: Diameter Dependence $F(d)$ for Smooth Circular Tubes ($r_d = 1.0$) According to Eq. (5.28)

The individual terms of Eq. (5.28) are shown graphically in Figure 5.13. It becomes clear that the classical definition of the diameter dependence with Eq. (5.14) is inappropriate, as $(d_0/d)^{0.4}$ becomes infinite in very small tubes. The new factor F_b has practically no effect down to tube diameters of $d = 3 \text{ mm}$, which is consistent with the scope of the classical VDI Heat Atlas correlation in [73].

Summary of the Nucleate Boiling Heat Transfer Model

With the diameter dependence defined in Eq. (5.28) the nucleate boiling heat transfer model finally yields

$$\frac{\alpha_{z,nb}}{\alpha_0} = C_F \left(\frac{\dot{q}}{\dot{q}_0} \right)^n \left[2.816 p^{*0.45} + \left(3.4 + \frac{1.7}{1 - p^{*7}} \right) p^{*3.7} \right] \left[\left(\frac{d_0 r_d}{d_c} \right)^{0.4} \left(1 - e^{-0.45 \frac{d_c}{\mathcal{L}}} \right) \right] \left(\frac{Ra}{Ra,0} \right)^{0.133}. \quad (5.29)$$

Fitting all 112 data points of Figure 5.11 and Figure 5.12 with Eq. (5.29) and the free parameter C_F yields

$$\begin{aligned} C_F &= 0.91 \pm 0.01 \\ \chi^2 &= 196. \end{aligned} \quad (5.30)$$

The result indicates that 68 % of the data fall within the error margin of $C_F = 0.91 \pm 0.01$. This precision, however, can not obscure the fact that the overall accuracy of flow-boiling heat transfer correlations is no better than $\pm 30\%$ to $\pm 40\%$. This is a consequence of varying numbers of active nucleation centers, which are the reason for meta-stable flow regimes.

In any case, more experimental data are imperative to evaluate whether the form of Eq. (5.28) and the exponent $c = 0.45$ are generally valid. Figure 5.13 suggests that dedicated experiments should be conducted in a tube diameter range of $d = 0.1\text{ mm}$ to $d = 1.5\text{ mm}$. Polar fluids with large surface tension and wetting angle, such as water, should be studied as well, as the surface tension influences the Laplace constant \mathcal{L} .

5.5 Critical Boiling Conditions

The phenomena of film boiling and dryout were already explained in Section 4.1. Film boiling is usually understood as a critical boiling condition that occurs at low quality and high heat flux. However, film boiling can also set in as a result of local dryout. This is shown in Figure 5.14 for dry evaporation ($x_{\text{out}} \approx 1$) and partial evaporation ($x_{\text{out}} < 1$). The two steady state conditions in Figure 5.14a correspond to the last two data points in Figure 5.11d. Accordingly, the two steady state conditions of $x_{\text{out}} = 0.43$ and $x_{\text{out}} = 0.45$ in Figure 5.14b relate to the last two data points in Figure 5.12c.

In both cases, a slight increase of the heat load \dot{Q} leads to thermal runaway of the block temperature T_b . However, the fluid is still entering the heat exchanger slightly sub-cooled at $x_{\text{in}} \approx -0.05$. Under normal conditions, the mean heat transfer coefficient could not change so dramatically at just a small increase of the outlet quality. Consequently, the local increase of the wall temperature at the outlet must be responsible for the onset of a critical boiling condition, which may be called *retroactive film boiling*. It requires a heat source with no temperature limit, and a high conductivity material to propagate the

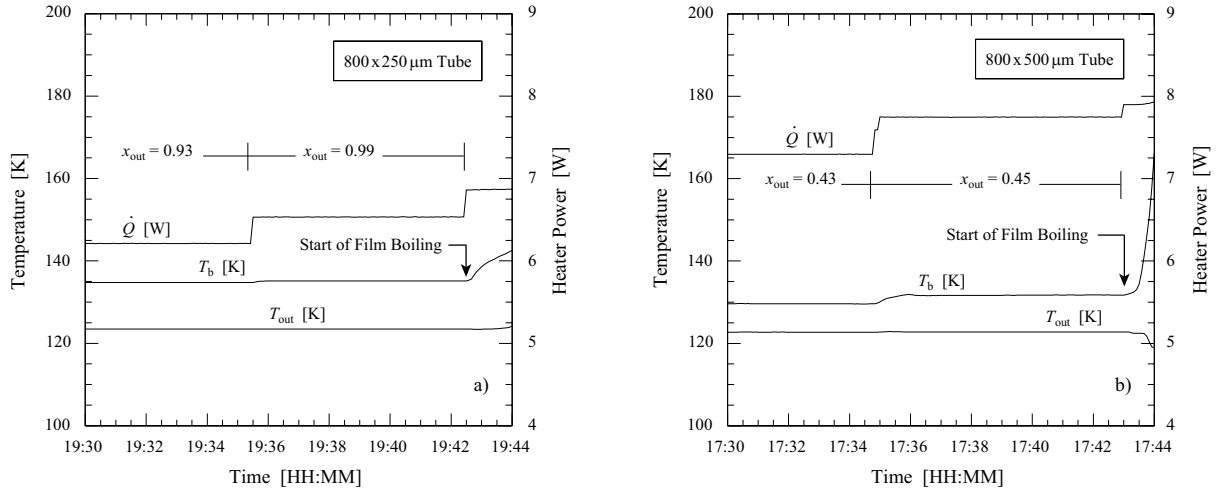


Figure 5.14: Film Boiling at High Quality

high wall temperature from the outlet (the location of dryout) to the inlet of the heat exchanger. The increased wall temperature signifies a heat flux $\dot{q}^* > \dot{q}_{crit}$, and causes film boiling despite the fact that the nominal heat flux $\dot{q} = \dot{Q}/A_w$ is smaller than \dot{q}_{crit} .

Similar results as shown in Figure 5.14a are reported by *Jiang et al.* [36]. He defines the critical heat flux (CHF) as the heat flux observed at $x_{out} = 1.0$, where thermal runaway occurred. This CHF, however, is certainly not identical to the critical heat flux \dot{q}_{crit} for film boiling. In our experiments, thermal runaway was observed at the end of *all* data series shown in Figure 5.11 and Figure 5.12, at all different mass and heat fluxes. The effect is therefore clearly related to dryout.

Both constructional prerequisites for *retroactive film boiling*, i. e. an electrical heat source and high wall conductivity, are present in electronic devices made of silicon. It is therefore essential to avoid the operational prerequisite, namely any form of dryout. This can be assured by a sufficient circulation rate of the coolant with e. g. $x_{out} \leq 0.5$, and a reasonable heat flux. Unfortunately, the *Ahmad* correlation [5] for the critical dryout heat flux does not fit the data very well, and the number of experimental data is not yet sufficient for modeling. For safety reasons, the control of electrical heat sources cooled by direct evaporation should always be thermally interlocked.

5.6 Stability of Flow-boiling

Stability tests of two-phase microtube cooling were carried out with a dummy detector module built for thermal and thermo-mechanical tests. The mechanical design of the module was already explained in Figure 1.3. The module is built with a $600 \times 500 \mu\text{m}$ CuNi cooling tube of $R_a \approx 3 \mu\text{m}$ surface roughness, which is embedded in the spacer under the pitch adapter. The installation of the module in the cooling circuit is shown in Figure 5.15, replacing the test section in the circuit scheme of Figure 4.1. The heat

load of the APV25 readout ASICs is simulated by electrical resistance heaters. Several PT-100 temperature sensors are attached to measure the temperature distribution in the module.

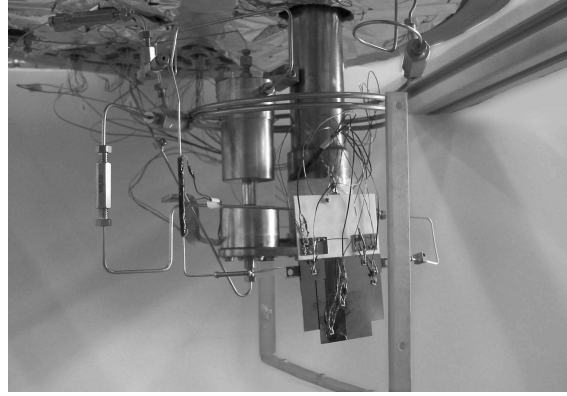


Figure 5.15: Installation of the Thermal Test Module in the Cooling Circuit

Generally, systems with reasonable pressure drop are more stable than systems operated at low velocities. The hydraulic design is particularly important in two-phase microtube cooling systems, as unsteady flow in parallel microchannels has been observed by a number of authors [41], [55]. The instabilities are caused by clogging of individual flow channels with growing vapor bubbles, and the resulting pressure waves can then cause flow reversal through a low-impedance by-pass (a parallel channel). Such instabilities, however, will not appear in microtube heat exchangers with a single flow path. The hypothesis that “two-phase flow in microchannels is inherently unstable” [55] can therefore not be supported.

Nevertheless, certain operating conditions close to the boiling line are prone to instabilities. This is demonstrated in Figure 5.16, where the fluid is entering the module slightly sub-cooled with a mass flux of $\dot{M} = 140 \text{ kg/m}^2\text{s}$. The heat load of $\dot{Q} = 1.5 \text{ W}$ is too small to ensure stable nucleation, and the system is therefore permanently oscillating between sub-cooled liquid cooling, liquid superheating, and evaporation.

In the VDI Heat Atlas correlation [73], the required heat flux for onset of nucleate boiling is given as

$$\dot{q}_{\text{onb}} = \frac{2 \sigma T_s \alpha_{l,0}}{r_{\text{crit}} \rho_v (h_v - h_l)} . \quad (5.31)$$

σ is the surface tension, T_s the saturation temperature, $\alpha_{l,0}$ the single-phase liquid heat transfer coefficient at the same mass flux, r_{crit} a critical radius, ρ_v the vapor density, and $h_v - h_l$ the latent heat. Under the operating conditions of Figure 5.16 and with $r_{\text{crit}} = 0.3 \mu\text{m}$ (constant for common technical surfaces [73]), Eq. (5.31) yields $\dot{q}_{\text{onb}} = 260 \text{ W/m}^2$, which is considerably below the actual heat flux of $\dot{q} = 19 \text{ kW/m}^2$. Although Eq. (5.31) is not experimentally verified for microtubes, the results suggest that the required heat flux to *provoke* nucleate boiling out of single-phase flow is considerably higher than the heat flux \dot{q}_{onb} to *cause* and *maintain* nucleate boiling in two-phase flow. This can be explained by the larger overpressure that is required in the bubble to accelerate the entire liquid

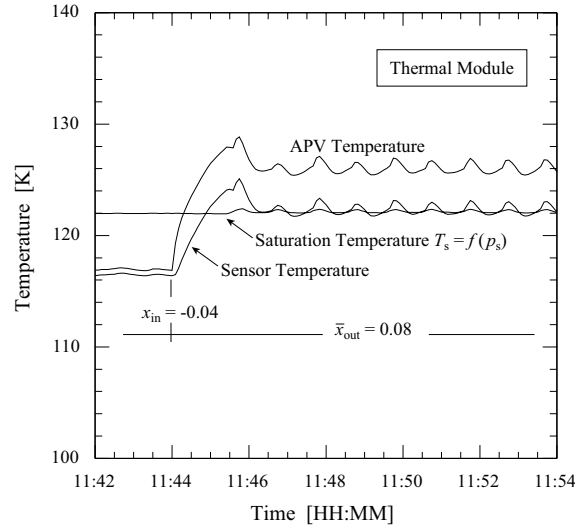


Figure 5.16: Instable Operation Close to the Boiling Line; $x_{\text{in}} = -0.04$, $\dot{M} = 140 \text{ kg/m}^2\text{s}$, $\dot{q} = 19 \text{ kW/m}^2$

column in the first case, whereas in the presence of two phases, the bubble can expand at lower Δp into the vapor phase. The difference of almost a factor 100 in the example has to be considered in the circuit layout.

The results in Figure 5.16, however, do not mean that the heat flux in a device always has to be higher than the minimum heat flux for onset of nucleate boiling \dot{q}_{onb} . If the fluid is entering the device in the two-phase region, stable operation in a pure convective boiling regime is possible at $\dot{q} < \dot{q}_{\text{onb}}$.

With an appropriate circuit design, microtube cooling systems can be operated in the nucleate boiling regime with very high stability. Figure 5.17a shows the thermal response of the cold module, when the nominal heat load for 6 APVs (1.78 W) is switched on after 6 min. The fluid is entering the module with a quality of $x_{\text{in}} = 0.39$ and a mass flux of $\dot{M} = 240 \text{ kg/m}^2\text{s}$. Data are recorded with a time interval of 5 s. The temperature stability of all sensors over a period of 1 hour is better than 20 mK. The stability of the flow is better than the noise of the flowmeter⁵.

Figure 5.17b shows the results of a long-term test over a period of 1 week. Data are recorded with a time interval of 1 min for an inlet quality of $x_{\text{in}} = 0.27$, a heat load of $\dot{Q} = 1.78 \text{ W}$, and a mass flux of $\dot{M} = 440 \text{ kg/m}^2\text{s}$. The system is operated without any active control, except the compensation heater for the cryocooler installed at the thermal interface. The results show that there is no oscillation or instability. The temperature shift of 1.4 K over the whole period is due to a loss of system pressure, which is caused by a small leak in the warm part of the circuit.

⁵ The standard deviation of data points during the measurements is identical with the standard deviation during zero-offset calibration of the flowmeter.

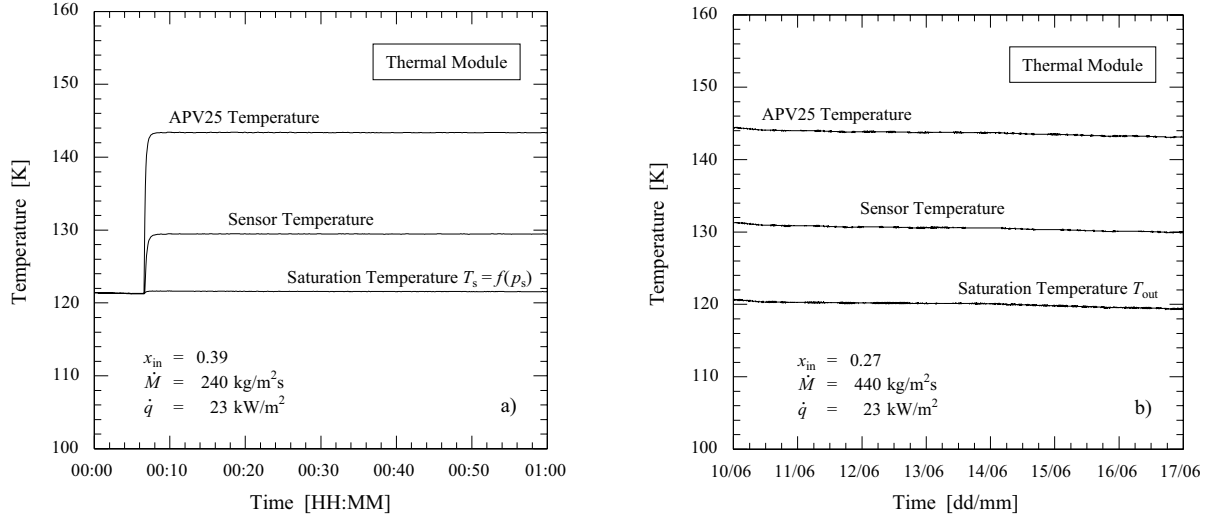


Figure 5.17: Temperature Stability of Two-phase Cooling

5.7 Design of Miniature Evaporator Heat Exchangers

The following design rules for miniature evaporator heat exchangers can be deduced from the experiments:

- The most important design criterion is the heat flux. Too low heat fluxes can cause instabilities in the transition from single-phase to two-phase flow (Figure 5.16). Too high heat fluxes can cause critical boiling conditions (Figure 5.14). The heat flux is the most influential parameter on the heat transfer coefficient.
- The heat flux to provoke nucleate boiling in (nearly saturated) single-phase flow can be considerably higher than the heat flux \dot{q}_{onb} to cause and maintain nucleate boiling in two-phase flow, which has to be considered in the circuit layout.
- Dryout conditions in evaporator heat exchangers must be avoided, choosing a sufficient fluid circulation rate and a reasonable heat flux. Electrical heat sources should always be thermally interlocked.
- The mass flux and the quality have little influence on nucleate boiling heat transfer. High velocities and pressure drop do not improve heat exchange and temperature differences, which is in contrast to single-phase flow. However, the stability of systems is usually improved with the pressure drop.
- From the last point it follows that short evaporators with a larger diameter are better than long evaporators with a smaller diameter at the same heat exchanger surface.
- Heat exchangers with parallel microchannels should be avoided in nucleate boiling heat transfer, unless instabilities caused by the bubble growth and subsequent flow reversal through a low-impedance bypass are prevented by appropriated means. In addition, the maldistribution of liquid in parallel channels increases the risk of local dryout, which can cause retroactive film boiling.

- Nucleate boiling requires microscopic surface roughness for the formation of nucleation centers.
- Macroscopic roughness in small tubes has a bigger influence than roughness in large tubes as a result of the increased surface-to-volume ratio. The roughness increases the actual wetted surface and therefore improves the heat transfer⁶. On the other hand, surface roughness increases flow friction. The influence of roughness on two-phase flow pressure drop in microtubes has to be further investigated.

For the practical application of cooling cryogenic tracking detectors, the appropriate cooling tube diameter depends on the overall pressure head in the circuit, and on the connection of modules in series or in parallel. The available pressure head in a fluid circuit with a cold pump or with a warm compressor is in the order of 2 bar to 5 bar. This pressure head should mainly be exhausted in the evaporator heat exchangers in order to maximize the cooling power density, i. e. to minimize the visibility of the cooling system in the modules.

Table 5.4: Calculated Two-phase Pressure Drop of Detector Half Modules Connected in Series; Fluid Argon at $T_s = 124$ K; Inlet Quality $x_{\text{in}} = 0$; Outlet Quality $x_{\text{out}} = 0.5$

APVs / Half Module	6		
Channels / APV	128		
Power Dissipation / Channel	2.31 mW		
Module Width	47 mm		
Cooling Tube Surface Roughness	3 μm		
Inner Tube Diameter	250 μm	500 μm	
Number of Half Modules in Series	4	4	14
Total Heat Exchanger Length	188 mm	188 mm	658 mm
Total Heat Load	7.1 W	7.1 W	24.8 W
Fluid Mass Flux	1718 kg/m ² s	429 kg/m ² s	1503 kg/m ² s
Total Pressure Drop Homogeneous Flow Model [83]	2.10 bar	0.07 bar	2.23 bar
Total Pressure Drop Storek & Brauer Correlation [74]	3.39 bar	0.12 bar	3.53 bar

⁶ As long as the decrease of $\alpha_{z,\text{nb}}$ due to the reduced heat flux does not dominate in nucleate boiling.

For the module design described in Figure 1.3, the calculated pressure drops of in series connected half modules are summarized in Table 5.4. In case of 4 half modules connected in series (which would be a typical design for Roman Pot detectors) a $250\text{ }\mu\text{m}$ tube would be sufficient, yielding a total pressure drop of about 2 bar to 3 bar. A $500\text{ }\mu\text{m}$ tube, on the other hand, has a total pressure drop of only about 100 mbar. Up to 14 half modules could be cooled in series with a pressure drop of 2 bar to 3 bar.

The $500\text{ }\mu\text{m}$ tube does not take full advantage of the potential of two-phase cooling. Even the heat flux of 48 kW/m^2 in the $250\text{ }\mu\text{m}$ tube is far from critical values. In the heat transfer measurements with the $800 \times 250\text{ }\mu\text{m}$ tube, heat fluxes up to 250 kW/m^2 were applied without risking critical boiling conditions. The lower limit of the tube diameters is therefore mainly restricted by the length of the flow channels, and the resulting pressure drop.

The only asset of the $500\text{ }\mu\text{m}$ tube may be a lower risk of clogging. However, miniature cryogenic fluid circuits inherently require clean conditions. In a circuit with a cryogenic micropump clogging should not be an issue, as the micropump is equipped with a filter of micrometer size, and downstream heat exchangers are consequently protected. In a fluid circuit with a warm compressor, the internal heat exchanger is more prone to clogging (or rather to freezing), if the filtering system is not sufficient. During weeks of operation with the oil-lubricated compressor unit the $800 \times 250\text{ }\mu\text{m}$ test section never got blocked.

The results in Table 5.4 strongly depend on the tube roughness, and vary between the predictions of the two pressure drop models. Neither of the two correlations are proven to work with microtubes. Although the homogeneous flow model generally yields acceptable precision at high mass fluxes [83], experimental investigations on two-phase pressure drop in microtubes are recommended.

6 DESIGN PRINCIPLES AND APPLICATIONS FOR MINIATURIZED CRYOGENIC FLUID CIRCUITS

6.1 *Circuit Layout with a Cryogenic Micropump*

The layout of a miniaturized fluid circuit suitable for cooling of cryogenic tracking detectors in a Roman Pot station is shown in Figure 6.1. The cooling unit is placed in the center between two Roman Pots, which are separated by several meters.

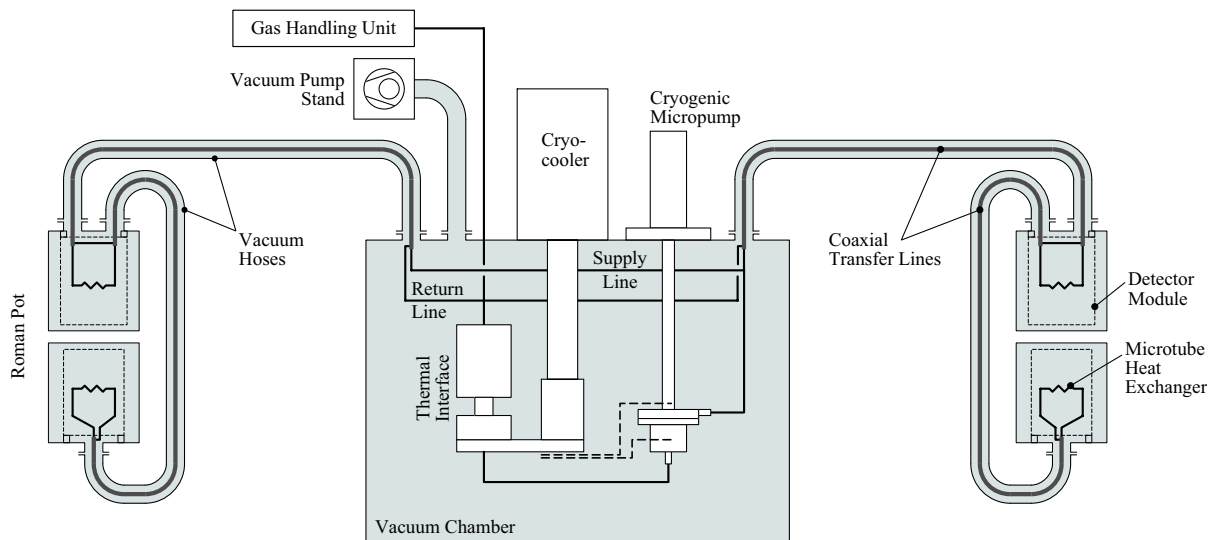


Figure 6.1: Cooling Circuit Layout for a Roman Pot Station

In the central cooling unit, a thermal interface is attached to the cold finger of a cryocooler, which is installed inside a vacuum chamber. The thermal interface shown in detail in Figure 6.2 consists of two reservoirs. In the upper reservoir, the fluid is condensed and stored in a receiver volume, before it enters a sub-cooler through a connecting channel in a neck that connects both reservoirs. The thermal design of the neck determines the temperature difference between the condenser and the sub-cooler heat exchangers.

The liquid is primed by a cryogenic micropump, which requires sub-cooling to avoid cavitation at the inlet, as well as to absorb its frictional heat. The micropump is thermally connected to the cold finger in order to pre-cool the pump body before start-up, and to absorb the heat leak along the shaft. The fluid is pumped into a fluid supply line, which is split inside the vacuum chamber according to the number of parallel consumers. The

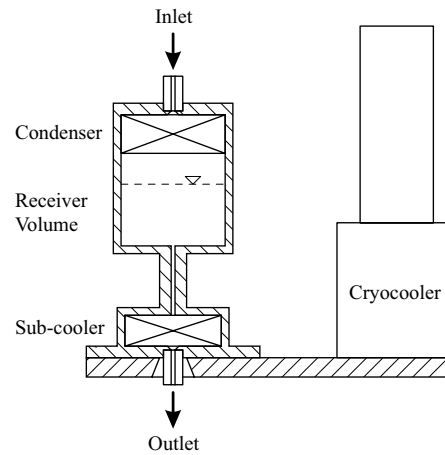


Figure 6.2: Design of the Thermal Interface

branches of the fluid supply line enter into the internal tubes of coaxial transfer lines, transporting the liquid to the Roman Pots. In the detector modules, the fluid is partially evaporated by the module's heat dissipation, and further pumped through coaxial transfer lines to downstream modules connected in series. At a circulation rate of two, 50 % of the fluid's latent heat is evaporated after the last module. The two-phase fluid then returns to the thermal interface through the external tubes of the coaxial transfer lines, and through the common fluid return line. Due to the pressure drop in the modules, the fluid return flow is at lower saturation temperature, protecting the liquid supply in the transfer lines from boil-off. Typical tube diameters for a Roman Pot station with an overall cooling power of 20 W are:

- Fluid supply and fluid return lines: 1 mm
- Internal tubes of transfer lines: 1 mm
- External tubes of transfer lines: 2 mm
- Wall thicknesses: 100 μm
- Microtube evaporator heat exchangers: 250 μm to 500 μm
- Wall thickness: 50 μm

The return line of the fluid circuit is connected to a gas handling unit outside the vacuum chamber. In the hermetic cooling system, the gas handling unit consists of an expansion vessel including safety valve to limit the system pressure during shutdown, and of means to evacuate, purge and fill the circuit.

The entire internal volume including the vacuum chamber, the flexible vacuum hoses, and the Roman Pots with the detector modules is interconnected. The cryogenic insulating vacuum of 10^{-6} mbar is provided by an autonomous vacuum pump stand¹.

¹ The control of the vacuum pump stand is interlocked with the beam line vacuum of the LHC.

Circuit Control

At start-up, the gaseous working fluid is condensed from the room-temperature pressure vessel into the thermal interface and into the micropump body. The micropump is switched on only after sufficient sub-cooling of the pump body, provided by the thermal link to the cold finger. Cooldown of the transfer lines and the detector modules is controlled by the pumping speed.

The cryocooler is operated constantly at its nominal power. During operation, the largest fraction of the cooling power is used to condense the working fluid. The condenser power is equivalent to the overall heat dissipation of the detector modules, plus parasitic heat leaks in the system. The difference to the cryocooler power is compensated by an electrical heater installed on top of the thermal interface. The heater is connected to a temperature controller, which controls the module temperatures through the fluid saturation temperature in the thermal interface. The receiver volume in the thermal interface is under saturation and balances varying operating conditions by the liquid level variation. The heat load over the neck in the thermal interface is constant at nominal and partial load operation, which yields roughly constant temperature differences between the condenser and the sub-cooler. The cooling capacity for the modules, i. e. the flow rate in the circuit, is controlled by the pump speed of the micropump.

Advantages of the Cooling Concept

The cooling concept of a miniaturized cryogenic fluid circuit with a cryogenic micropump is patented under DE 102 10 524 C1 [26]. Major advantages with respect to the requirements of detector cooling in High Energy Physics are:

- minimization of the cooling system's mass contribution in the detector modules,
- heat absorption with microtube heat exchangers very close to the readout electronics, which is the main source of heat,
- very large heat transfer coefficients, which together with the latter point minimizes thermal gradients and thermal stress in the detector modules,
- thin-wall microtubes minimize the stress on the modules due to the cooling tube connections,
- efficient mechanical and acoustic decoupling of the detector modules from the cryocooler.

Advantages related to the cooling system itself are:

- low and medium power cryogenic cooling distribution over long distances with low losses,
- minimization of the heat leak in transfer lines due to the small tube surfaces,
- separated temperature control through the thermal interface, and flow (capacity) control by the pumping speed,

- independent, hermetic and oil-free system that requires only electricity supply.

6.2 Design of the Compressor Unit

In the experiments on heat transfer measurements it could be demonstrated that a compressor unit is a reliable technical alternative to a cryogenic micropump. Such a compressor unit is connected to the low-temperature part of the microtube fluid circuit via an internal heat exchanger. The circuit layout and the operation were already explained in Section 2.2 and Section 4.2.

The compressor unit shown in Figure 6.3 consists of standard components from refrigeration technology. The inlet vapor is compressed with a hermetic compressor, and then cooled close to ambient temperature in an air-cooler. The smallest hermetic compressors commercially available are piston compressors, which still have flow rates of almost a factor 10 higher than required in microtube fluid circuits. A large fraction of the compressed

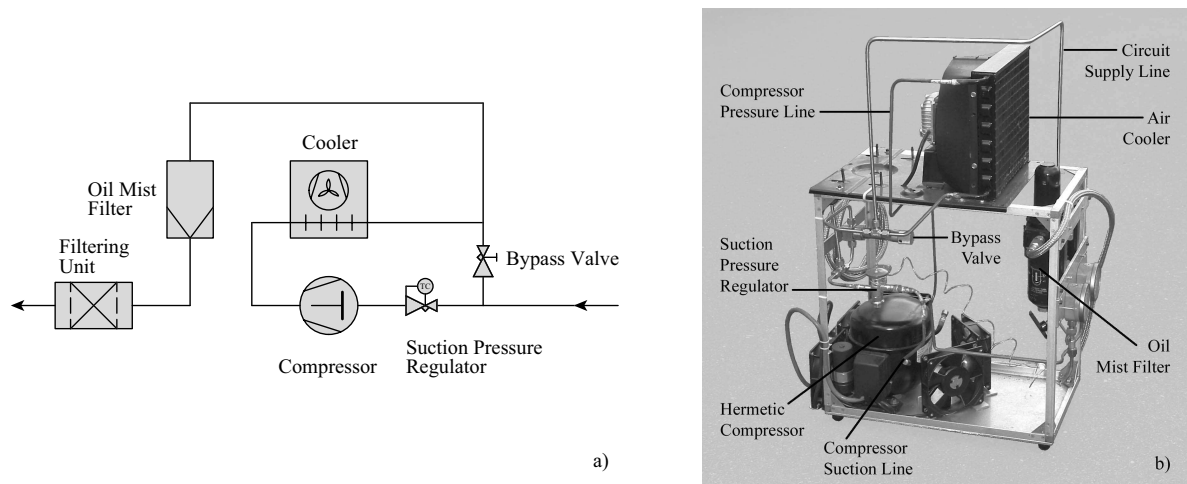


Figure 6.3: Design of the Compressor Unit

flow is therefore returned to the compressor inlet through a bypass valve. The outlet flow of the compressor has about 3 % to 5 % oil content, which has to be returned to the inlet. The air-cooler is therefore located above the compressor. The compressor pressure line is designed for vapor velocities of $w > 10$ m/s, which ensures oil-transport in the inclined tube. From the air-cooler, the oil is returned to the compressor together with the bypass flow, supported by gravity. The circuit supply line is inclined and designed for low vapor velocities in order to separate oil droplets. The oil mist is separated afterwards in a first filtering stage. A subsequent filtering unit consists of an activated charcoal filter for oil vapors, a molecular sieve filter for water vapor, and a $2\text{ }\mu\text{m}$ particle filter. This unit is not shown in Figure 6.3b.

The hermetic compressor of type *Danfoss TL4GH* used in the experiments is a heat pump compressor normally operated with refrigerant R134a. It is designed for high back

pressure applications, having a larger discharge valve. The size of the discharge reed valve limits the maximum suction pressure, and the minimum pressure ratio. Too high suction pressure leads to increased mass flow and exceedingly high volume flow through the discharge valve. This together with a low pressure ratio makes the reed valve open too far and too long, and will result in material fatigue². The suction pressure in the compressor unit is therefore limited by a suction pressure regulator³.

On the other hand, the maximum pressure ratio is limited by the fluid outlet temperature, which should generally be below 180 °C to avoid cracking of the compressor oil. This is particularly important for the monoatomic fluid argon, which has an isentropic exponent of $\kappa = 1.68$ at $T = 300$ K and $p = 5$ bar compared to $\kappa = 1.18$ for R134a.

During the experiments, an appropriate balance between minimum and maximum pressure ratio was found at $\pi \approx 3$, with a compressor inlet pressure of 6 bar and a high pressure of 15 bar to 20 bar (depending on the required flow rate in the microtube circuit). No performance degradation of the compressor *TL4GH* was noticed after several months of operation.

The throttling of the suction pressure, however, is energetically inefficient. A better way to profit from the minimum pressure ratio required by the compressor is to expand the condensed fluid into the two-phase region (refrigeration cycle). The cryocooler can then be operated at a 10 K to 20 K higher condensation temperature, which reduces its energy consumption.

6.3 Potential Applications

The advantages of miniaturized cryogenic fluid circuits are of interest for a number of applications beyond the field of detector cooling in High Energy Physics. Closed-cycle cryogenic cooling is particularly needed for the commercialization of superconductor technology. Table 6.1 gives some insight into R&D activities in this field.

Promising applications in the cooling power range of 10 W to 100 W are superconductive magnet bearings, which are being developed for centrifuges, motors, generators, and fly-wheels in energy storage systems. In such applications, the cooling power of an external cryocooler can be transferred with low losses to a bearing in the center of a machine, requiring little space for the vacuum insulated transfer line. The mass of the bearings itself can be reduced by the fraction of conductive material normally needed for heat spreading. In addition, temperature gradients and thermal stresses can be minimized, integrating microtube evaporator heat exchangers close to the heat sources. In some of these applications, e. g. in fly-wheels, the energetic efficiency of the cooling system is as important as the prize, influencing the overall energy consumption and the operating costs.

² Several compressors of type *Danfoss TL3G* failed after a few days of operation at a pressure ratio $\pi \leq 1.5$.

³ A thermostatic expansion valve of type *Danfoss TUA* is used, where the diaphragm is pressurized with the default pressure through the temperature sensor capillary

Medium power cryogenic applications beyond 100 W cooling power are, for instance, superconductive transformers, superconductive current limiters and superconductive motors. Up-scaling of the cryogenic micropump, the compressor unit and the microtube fluid circuit to the capacities required in these applications is straightforward.

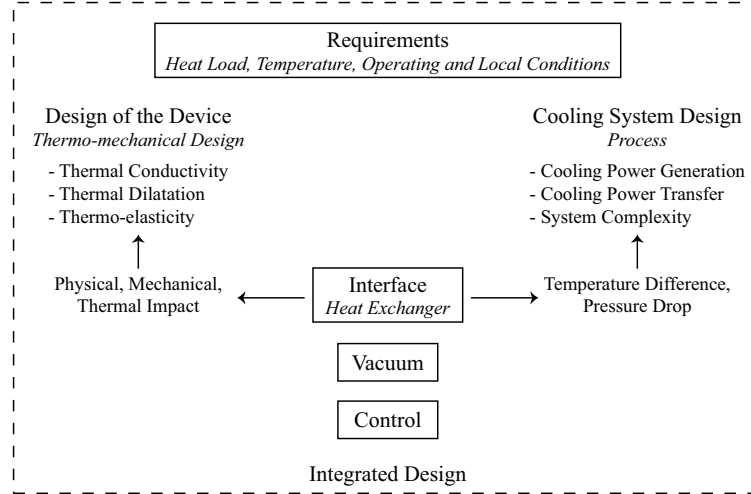


Figure 6.4: Design Issues of Cryogenic Applications Related to the Cooling

Generalized design issues for detector cooling and superconductor applications are summarized in Figure 6.4. Cooling is an essential issue in most of these applications, and cannot be considered as an independent service. Integrated and interdisciplinary R&D is therefore imperative.

Table 6.1: R&D Activities of German Companies on HTSC Applications and Their Market Expectations [19]

Application	Cooling Requirements	Company Milestones	Expected Market Potential	Remarks
12 MVA Current Limiters	300 W @ 77 K	R&D: 2006	5000–10000 units/a	Existing Market
1–4 MVA Current Limiters	120–150 W @ 77 K	Market Introduction: 2005–2006		
Motors with HTSC Rotor	40 W @ 35 K	Full Production: until 2012	500–1000 units/a	Present Product Line
Flywheels for Energy Storage Systems	30–50 W @ 60–77 K	R&D: 2004–2005 Market Introduction: until 2008	5000 units/a	Existing Market Efficiency Important
Passive Magnet Bearings for Centrifuges, Motors, Generators, ...	2 W @ 77 K 30 W @ 77 W	Market Introduction: 2004–2005	Total Volume: 300 MIO EUR/a	Goal: Cooling $\leq 10\%$

7 CONCLUSIONS

7.1 Summary

Cooling Distribution (Section 2)

Miniaturized cryogenic fluid circuits are the key to compensate the limitation of regenerative cryocoolers in terms of cooling distribution in the range of medium cooling power. The best performance and the highest degree of integration in a device is achieved with two-phase flow and active circulation of the coolant. The two technical options are circuits with a room-temperature compressor and with a cryogenic pump, respectively.

The specific volume flow rate per unit of cooling power in such a circuit is typically in the range of 0.5 ml/min W to 1.0 ml/min W, which leads to flow channel diameters well below 1 mm in heat exchangers. The heat transfer and the pressure drop in microchannel heat exchangers is increasingly influenced by surface effects such as roughness, as the surface-to-volume ratio increases towards small dimensions. Parallel microchannels enable the reduction of temperature gradients, and the power upgrade by adding parallel channels of the same diameter. The increase of the cooling power density, however, generally requires an increase of the pressure head, and single-phase turbulent or two-phase flow regimes.

Cryogenic Micropumps (Section 3)

Liquid pumps suitable for miniaturized cryogenic fluid circuits are not available on the market. With respect to the performance requirements, volumetric rotary pumps have the best potential for miniaturization. The performance of these pumps is largely influenced by internal clearances, which is particularly important for operation with low viscosity fluids.

A prototype of a cryogenic micropump was developed, based on the principle of micro annular gear pumps that are commercially available for room-temperature applications. The key components are produced by micro machining technologies with positional and shape tolerances on the micron level. Critical design issues such as bearings, lubrication, and thermal dilatation are solved by the material composition.

The operating principle of the cryogenic micropump was proven to work. A performance of almost 3 bar pressure head was achieved at a mass flow rate of 100 mg/s argon at 110 K. The operation was demonstrated for several hours. Nonetheless, the development has revealed that the implication of the design rules in practice is highly demanding, and that a reliable operation will require thorough control of fabrication and assembly.

Heat Transfer Measurement in Microtubes (Section 4)

The concept of heat transfer measurements in microtubes differs from experiments with large tubes, as the inner wall temperature and the local heat transfer coefficient cannot be measured directly. The mean heat transfer coefficient and the mean inner wall temperature are therefore determined from the measured temperature of the heat exchanger body, and from the effective thermal resistance between the heat exchanger body and the wetted surface.

The effective thermal resistance R_{eff} is determined from a series of measurements in single-phase turbulent liquid flow as an extrapolation to infinite Reynolds numbers. In flow-boiling heat transfer, R_{eff} is a constant "material property" specific to the location of the temperature sensor on the heat exchanger body. It is therefore (in first order) independent of the heat flux. In single-phase flow, R_{eff} is influenced by the heat flux distribution in the heat exchanger body.

Characteristic dimensions in tubes with large relative roughness are analyzed in Section 4.4. A new relative roughness parameter r_d is proposed in Eq. (4.27), signifying the diameter ratio between a perfectly smooth circular tube of the same wetted surface, and a perfectly smooth circular tube of the same cross-sectional area.

The analysis of flow-boiling heat transfer data described in Section 4.5 is based on the measurement of mean heat transfer coefficients at a constant inlet quality of $x_{\text{in}} \approx 0$, and at variable outlet quality x_{out} . The experimental data are fitted with a heat exchanger model, and a correlation for local flow-boiling heat transfer coefficients.

Results of Heat Transfer Measurements (Section 5)

Section 5 contains experimental results on single-phase and flow boiling heat transfer in horizontal microtubes of 250 μm and 500 μm nominal inner diameter, and the modeling of these data. The working fluid is argon at around 120 K.

The results on single-phase heat transfer summarized in Section 5.1 reveal that there is no physical difference in heat transfer mechanisms between macrotubes and microtubes. The enhancement of heat transfer coefficients in small tubes compared to conventional correlations is explained with the increased influence of roughness, i. e. the relative increase of the wetted surface compared to the volume. The enhancement of surface effects in tubes with large relative roughness can be modeled with the new parameter r_d , yielding Eq. (5.2) in turbulent liquid flow, and Eq. (5.3) in turbulent vapor flow. In laminar flow, the breakage of boundary layers on asperities improves the heat transfer in the entry region.

Experimental results on flow-boiling heat transfer are discussed in Section 5.3 to Section 5.6. The modeling of heat transfer coefficients is based on the VDI Heat Atlas correlation [73] for vertical tubes.

Although the focus was mainly on nucleate boiling, some data were taken at low heat flux under pure convective boiling conditions. The results presented in Section 5.3 suggest

that the corresponding VDI Heat Atlas model can be applied with a reasonable accuracy.

The experimental data on nucleate boiling heat transfer are analyzed in Section 5.4. The results show that there is no significant influence of the mass flux and the quality. The VDI Heat Atlas correlation for vertical tubes is in good agreement with the data, except for the diameter dependence. An extension of the diameter function is therefore proposed in Eq. (5.28), based on the Laplace constant. The extended function becomes effective when the tube diameter is in the range of the bubble departure diameter from the wall.

Nucleate boiling flow regimes can be meta-stable. The effect is certainly related to the number of active nucleation centers, which is influenced by the history of the flow. The prediction of nucleate boiling heat transfer coefficients can therefore be no better than about $\pm 30\%$ to $\pm 40\%$. High statistics is required to analyze the difference between the intrinsic variations and systematic effects.

Critical boiling conditions are discussed in Section 5.5. The term *retroactive film boiling* is introduced for an effect, which describes thermal runaway caused by local dryout. Retroactive film boiling requires an electrical heat source, and a high conductivity material to propagate an increased wall temperature (that signifies an *actual* heat flux beyond the critical heat flux) from the location of dryout through the heat exchanger.

Section 5.6 illustrates that evaporative microtube cooling systems can be operated with a very high stability. Operating conditions close to the boiling line, however, should be avoided.

General design rules for microtube evaporator heat exchangers are summarized in Section 5.7. The heat flux is the most important parameter, determining the heat transfer coefficient, as well as the onset of nucleate boiling and critical boiling conditions. Short evaporators with a larger diameter are better than long evaporators with a smaller diameter at the same heat exchanger surface. Heat exchangers with parallel microchannels may be unstable due to the clogging of individual flow channel by growing bubbles. Parallel microchannels should therefore be avoided, unless flow reversal is prevented by appropriated means. Maldistribution of liquid in parallel channels increases the risk of local dryout, which can cause retroactive film boiling.

The design of microtube evaporator heat exchangers for cryogenic silicon detector modules is mainly determined by the length of the heat exchanger, the number of modules in series, and the available pressure head. The heat flux even in $250\ \mu\text{m}$ tubes is far from critical boiling conditions. In case of the detector module design described in Section 1 and with an available pressure head of about 2 bar to 3 bar, 4 half modules with a $250\ \mu\text{m}$ cooling tube can be connected in series, compared to 14 half modules with a $500\ \mu\text{m}$ cooling tube.

Circuit Design and Applications (Section 6)

The layout and the control of a microtube fluid circuit with a cryogenic micropump is described in Section 6.1. The cooling concept is patented under DE 102 10 524 C1 [26]. It fulfills fundamental requirements to minimize the impact of cooling in cryogenic tracking detectors for High Energy Physics.

The design of a compressor unit as alternative for a cryogenic micropump is explained in Section 6.2. The compressor unit is built of standard components from refrigeration industry.

Section 6.3 lists potential applications for miniaturized cryogenic fluid circuits, which are mainly found in the field of superconductor technology. The importance of integrated R&D is emphasized.

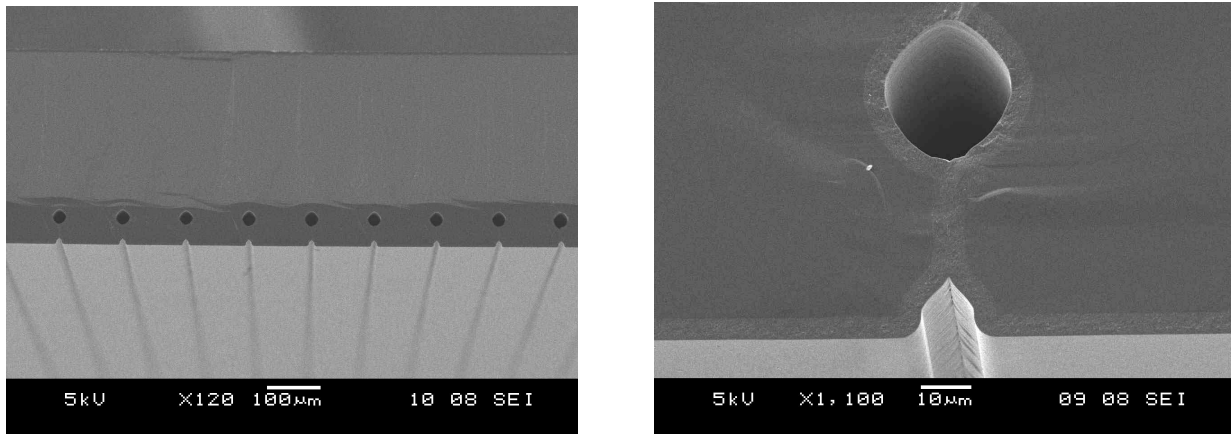


Figure 7.1: SEM Pictures of Buried Microchannels in Silicon Wafers Sealed with Poly-Silicon [10]

7.2 Proposals for Future Research and Development

Heat transfer and pressure drop are the most important quantities for the design of fluid circuits. The static pressure drop and the momentum pressure drop (in two-phase flow) are described by analytical solutions. These two components, however, have usually little influence on the overall pressure drop, which is mainly determined by flow friction. As the validity of conventional pressure drop correlations is not proven for small diameters, dedicated experiments on flow friction in microtubes are recommended. The results of the heat transfer measurements suggest that the single-phase pressure drop is not fundamentally different from that in macrotubes. Nonetheless, the influence of the increased relative roughness should be studied in detail. The prediction of the frictional pressure drop during nucleate boiling in microtubes, however, implicates larger uncertainties. Deviations from conventional correlations can be expected when the tube diameter is in the range or below the bubble departure diameter from the wall.

A number of future research topics can be derived from the heat transfer measurements. The proposed extensions of the *Hausen*-type equations for turbulent heat transfer with the relative roughness parameter r_d should be verified by more statistics. The results also suggest that the roughness parameter r_d might be suitable to model the improvement of single-phase heat transfer in so-called *enhanced surface tubes*. This hypothesis has to be proven by experiments.

The proposed Eq. (5.28) for the diameter dependence of nucleate boiling heat transfer clearly requires more statistics. Experiments should be conducted in a tube diameter range of 0.1 mm to 1.5 mm. Fluids with different surface tension and wetting angle should be considered, as the surface tension influences the bubble departure diameter from the wall. For critical boiling conditions and for the onset of nucleate boiling, poor agreement was found between the experimental data and common correlations. The modeling of these conditions (in particular that of dryout) is important, and should be further investigated.

The ultimate level of integration in detector and electronics cooling can be achieved with fluid channels in the bulk of processed silicon wafers. Figure 7.1 shows buried microchannels in a standard $300\text{ }\mu\text{m}$ silicon wafer, produced by the authors of Ref. [10]. Such channels can be produced in arbitrary size and shape. Sealing of the channels with poly-silicon yields an almost mono-crystalline structure, which prevents the generation of thermal stress.

Although the technology for fabricating buried microchannels is available, a number of technical issues have to be addressed before it can be applied for detector cooling. The most important issue is the post-processing of microchannels in wafers with processed electronics. This limits the maximum annealing temperature to about 400°C . Another important issue concerns the hydraulic connections to the wafer, and in particular the mechanical link between silicon and metallic tubing. The heat exchanger would need to have parallel microchannels, with channel diameters of $50\text{ }\mu\text{m}$ to $100\text{ }\mu\text{m}$. The design of such heat exchangers requires more R&D in order to understand the conditions for stable flow and heat transfer.

The concept of microchannel cooling is independent of the operating temperature. The cooling technology developed for cryogenic tracking detectors can be applied for detector cooling close to room-temperature, requiring only a change of the working fluid. For example, CO_2 is a suitable coolant for detector cooling around -20°C .

Buried microchannel cooling is particularly suited for pixel detectors, where the heat load is dissipated on the entire surface. Present generations have a power density of about 1 W/cm^2 detector surface. The pixel pitch is typically $50\text{ }\mu\text{m}$, allowing a vertex resolution of around $10\text{ }\mu\text{m}$. The demands for an upgraded LHC will push for a higher resolution and a higher precision in timing, which will inevitably increase the power density. Smaller pixel dimensions, however, make no sense if the thickness of the detector modules cannot be reduced. Here, the microchannel cooling may prove advantageous due to its high level of integration, and because no additional heat spreader material is required.

APPENDIX

A ALGORITHMS FOR SCALING OF HEAT TRANSFER AND FLOW PARAMETERS

The following algorithms shows how to scale heat exchange and flow parameters with the linear dimension variable β , representing the diameter d and the length L of a flow channel in a heat exchanger. In a first example, the power density per volume unit is fixed for reference. All subsequent formulas of Eq. (A.2) to (A.22) are only valid for this reference condition¹

$$V \propto \beta^3 \quad \text{and} \quad \dot{Q}/V = 1 . \quad (\text{A.1})$$

It is further assumed that material properties as well as fluid and transport properties of the working fluid are independent of size. It follows that the cooling power \dot{Q} and the mass flow \dot{m} scale with β^3

$$\dot{Q} = \dot{m} \Delta h = \dot{V} \rho \Delta h \propto \beta^3 . \quad (\text{A.2})$$

With the cross-sectional area A_c the velocity w scales with

$$w = \frac{\dot{V}}{A_c} \propto \frac{\beta^3}{\beta^2} = \beta , \quad (\text{A.3})$$

and the Reynolds number Re with

$$Re = \frac{\rho w d}{\eta} \propto \frac{\beta \beta}{1} = \beta^2 . \quad (\text{A.4})$$

Scaling effects on heat transfer and pressure drop depend on the flow regime, i. e. laminar flow, turbulent flow or two-phase flow, and have to be analyzed separately. In contrast to the laminar flow regime, there is no physical model and consequently no analytical solution for the heat transfer and the friction coefficient in single-phase turbulent and two-phase flow. These mechanisms are described with empirical correlations that are valid within certain boundary conditions. The mathematical form of these equations often allows only qualitative scaling analysis under specific conditions.

Laminar Flow

The heat transfer at laminar flow in circular tubes can be calculated theoretically in case of fully developed velocity and temperature profiles. At uniform surface heat flux, the

¹ An example of how to re-calculate the results for a different reference condition is given in Eq. (A.23).

Nusselt number Nu_∞ is a constant independent of Re and Pr . The solution of the energy equation gives

$$Nu_\infty = \frac{\alpha d}{\lambda} = 4.364 \quad \text{at} \quad \dot{q} = \text{constant} , \quad (\text{A.5})$$

and the approximation of the temperature profile in case of constant wall temperature yields

$$Nu_\infty = 3.656 \quad \text{at} \quad T_w = \text{constant} . \quad (\text{A.6})$$

In both cases, the heat transfer coefficient α_{lam} scales with

$$\alpha_{\text{lam}} = \frac{Nu_\infty \lambda}{d} \propto \frac{1}{\beta} = \beta^{-1} . \quad (\text{A.7})$$

Single-phase pressure drop is generally expressed in the form

$$\Delta p = \xi \frac{L}{d} \frac{\rho w^2}{2} . \quad (\text{A.8})$$

For incompressible laminar flow in smooth tubes the friction coefficient ξ is given by the *Hagen-Poiseuille* law as

$$\xi = \frac{64}{Re} , \quad (\text{A.9})$$

which is an exact solution of the *Navier-Stokes* equations. The combination of Eq. (A.8) and Eq. (A.9) yields

$$\Delta p_{\text{lam}} = \frac{64}{Re} \frac{L}{d} \frac{\rho w^2}{2} \propto \frac{1}{\beta^2} \frac{\beta}{\beta} \frac{\beta^2}{1} = 1 . \quad (\text{A.10})$$

Turbulent Flow

Heat transfer in turbulent flow can be described with the *Dittus and Boelter* equation [84], which gives in case of fluid heating

$$Nu = 0.0243 Re^{0.8} Pr^{0.4} . \quad (\text{A.11})$$

The heat transfer coefficient α_{turb} then scales with

$$\alpha_{\text{turb}} = \frac{Nu \lambda}{d} \propto \frac{\beta^{1.6}}{\beta} = \beta^{0.6} . \quad (\text{A.12})$$

According to *Blasius* [43], the friction coefficient ξ for turbulent flow in *smooth* tubes is calculated with

$$\xi = \frac{0.3164}{Re^{0.25}} \quad \text{for} \quad 3000 < Re < 10^5 , \quad (\text{A.13})$$

and the pressure drop under these conditions scales with

$$\Delta p_{\text{turb}} = \frac{0.3164}{Re^{0.25}} \frac{L}{d} \frac{\rho w^2}{2} \propto \frac{1}{\beta^{0.5}} \frac{\beta}{\beta} \frac{\beta^2}{1} = \beta^{1.5} . \quad (\text{A.14})$$

In *rough* tubes, the friction coefficient increases with the relative roughness $\epsilon = R_a/d$. The implicit expression

$$\frac{1}{\sqrt{\xi}} = -2 \log \left[\frac{2.51}{Re \sqrt{\xi}} + \frac{R_a}{3.71 d} \right] . \quad (\text{A.15})$$

describes the transition from smooth to rough turbulent flow [43], [37], and scaling factors can only be calculated for specific cases. In fully developed rough flow, the friction coefficient is independent of Re and can be expressed in the form [43]

$$\frac{1}{\sqrt{\xi}} = 2 \log \left(\frac{d}{R_a} \right) + 1.14 . \quad (\text{A.16})$$

If the relative roughness ϵ of tubes remains constant, the friction coefficient ξ scales with 1 and Eq. (A.8) yields

$$\Delta p_{\text{turb}} \propto 1 \frac{\beta}{\beta} \frac{\beta^2}{1} = \beta^2 . \quad (\text{A.17})$$

However, one may as well consider the arithmetic mean roughness R_a being constant, e. g. determined by the production method. In that case scaling parameters can only be estimated for specific conditions, as in case of Eq. (A.15).

Two-phase Flow

Heat transfer in two-phase flow is a complex topic, discussed in detail in Section 4 and Section 5. To estimate the scaling effect, the VDI Heat Atlas correlation [73] for nucleate boiling in vertical tubes is used. The local nucleate boiling heat transfer coefficient is given in [73] as

$$\frac{\alpha_{z,\text{nb}}}{\alpha_0} = C_F \left(\frac{\dot{q}}{\dot{q}_0} \right)^n F(p^*) F(d) F(W) , \quad (\text{A.18})$$

where α_0 and \dot{q}_0 are reference values from pool boiling. The heat flux $\dot{q} = \dot{Q}/A_w$ is proportional to (β^3/β^2) . The exponent n for the heat flux dependence is a function of the reduced pressure p^* . For cryogenic fluids and the common case of $p^* \approx 0.1$, n has a value of 0.5. The factor $F(p^*)$ considers fluid properties and has no effect on scaling. The diameter dependence $F(d)$ scales with $\beta^{-0.4}$, and $F(W)$ has no influence on scaling in case of constant absolute roughness R_a . Under these conditions, the two-phase heat transfer coefficient α_{2p} scales with

$$\alpha_{2p} \propto \left(\frac{\beta^3}{\beta^2} \right)^{0.5} \beta^{-0.4} = \beta^{0.1} . \quad (\text{A.19})$$

The scaling analysis of frictional pressure drop in two-phase flow is built on the *Storek* and *Brauer* correlation [74], where the influence of the mass flux \dot{M} and the diameter d are given as

$$\left(\frac{\Delta p}{L} \right)_{2p} \propto \dot{M}^{1.92} \quad \text{and} \quad \left(\frac{\Delta p}{L} \right)_{2p} \propto d^{-1.4} . \quad (\text{A.20})$$

The influence of roughness is expressed in the correction function

$$\psi = \sqrt{1 + 51 \left(\frac{R_a}{d} \right)^{0.8}} . \quad (\text{A.21})$$

In smooth tubes or in tubes with constant relative roughness ψ is proportional to β^0 , and the two-phase flow pressure drop Δp_{2p} scales with

$$\Delta p_{2p} \propto \left(\frac{\beta^3}{\beta^2} \right)^{1.92} \beta^{-1.4} \beta = \beta^{1.52} . \quad (\text{A.22})$$

The results of Eq. (A.2) to (A.22) are summarized in Table A.1.

Table A.1: Scaling of Heat Transfer and Flow Parameters at Constant Power Density

Parameter	Laminar Flow	Smooth Turbulent Flow	Rough ² Turbulent Flow	Two-phase ³ Flow
Velocity w	β			
Reynolds Number Re	β^2			
Cooling Power \dot{Q}	β^3			
Heat Flux \dot{Q}/A_w	β			
Heat Transfer Coefficient α	β^{-1}	$\beta^{0.6}$	$\beta^{0.6}$	$\beta^{0.1}$
Temperature Difference \dot{q}/α	β^2	$\beta^{0.4}$	$\beta^{0.4}$	$\beta^{0.9}$
Pressure Drop Δp	1	$\beta^{1.5}$	β^2	$\beta^{1.52}$

Different Reference Conditions

It was pointed out in Section 2.3 that different reference conditions may be chosen for various reasons. In such a case, the scaling parameters can be re-calculated as illustrated in the following example:

If systems with similar pressure drop shall be compared, and if a major fraction of the pressure drop is caused by turbulent flow in smooth tubes, Eq. (A.14) becomes

$$\Delta p_{\text{turb}} \propto \frac{1}{w^{0.25} \beta^{0.25}} \frac{w^2}{1} \stackrel{!}{=} 1, \quad (\text{A.23})$$

$$w \propto \beta^{1/7}. \quad (\text{A.24})$$

The scaling factors of all the other parameters can then be calculated on the basis of the velocity scaling $w \propto \beta^{1/7}$.

The scaling of heat transfer parameters at constant pressure drop is summarized in Table 2.5.

² Only valid for a constant relative roughness ϵ .

³ Only valid for smooth tubes.

B ALGORITHMS FOR FITTING HEAT TRANSFER DATA

B.1 Fitting Algorithm for Single-phase Heat Transfer Data

Beginning of the fitting routine in a file *FitTurbulentLiquid.cxx*.

```
// C++ SOURCE CODE FOR FITTING HEAT TRANSFER DATA WITH MINUIT [68]
// SINGLE PHASE TURBULENT LIQUID FLOW
//
// EXAMPLE DATA IN FILE 1phase_data.txt - 800x250um TUBE

#include "TMinuit.h"
#include "math.h"
#include <fstream>

Double_t Re[100], krec[100], Pr[100], KT[100], Lam[100], errorry[100];
Double_t chi2;
Int_t nrows;
Double_t dw, L, Chi2;
int i = 0;
```

```
Double_t FitFunc(Double_t x0, Double_t x1, Double_t x2, Double_t x3,
                 Double_t *par)
// Sub-routine: Fit function according to Eq. (4.20)
// x[0] = Re, x[1] = Pr, x[2] = KT, x[3] = Lam;
// par[0] = H0, par[1] = H1, par[2] = H2, par[3] = H3*Aw
{
    Double_t Pr04 = pow(x1,0.4);
    Double_t geom = 1 + pow(dw/L,2./3.);
    Double_t Nusselt = par[0]*(pow(x0,par[1])-par[2])*Pr04*geom*x2;
    Double_t value = dw/(Nusselt * x3) + par[3];
    return value;
}
```

```
void fcn(Int_t &npar, Double_t *gin, Double_t &f, Double_t *par, Int_t iflag)
// Sub-routine: Minimization function
{
    Int_t i;
    Double_t chisq = 0;
    Double_t delta;
    for (i=0; i<nrows; i++) {
        delta = (krec[i]-FitFunc(Re[i],Pr[i],KT[i],Lam[i],par))/errorry[i];
        chisq += delta*delta;
    }
}
```

```

    Chi2 = chisq;
    f = chisq;
}

void FitTurbulentLiquid()
// Main routine
{
    // Reading data from the file
    // -----
    int i = 0;
    char* file = "1phase_data.txt";
    std::ifstream in(file);
    in >> dw;
    in >> L;
    in >> nrows;
    while (1) {
        in >> Re[i] >> Pr[i] >> KT[i] >> Lam[i] >> krec[i];
        if (!in.good()) break;
        errory[i] = krec[i]*0.02;           /* Error of 1/k */
        i++;
    }
    in.close();

    // initialize TMinuit with a maximum of 5 parameters
    // -----
    TMinuit *gMinuit = new TMinuit(5);
    gMinuit->SetFCN(fcn);
    Double_t arglist[10];
    Int_t ierflg = 0;
    arglist[0] = 1;
    gMinuit->mnexcm("SET ERR", arglist ,1,ierflg);

    // Set starting values and step sizes for parameters
    // -----
    gMinuit->mnparm(0, "H0", 0.012, 0.0001,0,0,ierflg);
    gMinuit->mnparm(1, "H1", 0.904, 0.001,0,0,ierflg);    /* Obtained in 1st fitting */
    gMinuit->mnparm(2, "H2", 280, 0.1,0,0,ierflg);
    gMinuit->mnparm(3, "H3", 0.000001, 0.000000001,0,0,ierflg);

    // Fixing of parameters
    // -----
    gMinuit->FixParameter(0);
    gMinuit->FixParameter(1);           /* Comment out in 1st fitting! */
    gMinuit->FixParameter(2);

    // Now ready for minimization step
    // -----
    arglist[0] = 500;
    arglist[1] = 1.;
    gMinuit->mnexcm("MIGRAD", arglist ,2,ierflg);

    // Print results
    // -----
    Double_t amin,edm,errdef;
    Int_t nvpar,nparx,icstat;
    gMinuit->mnstat(amin,edm,errdef,nvpar,nparx,icstat);
}

```

```
    gMinuit->mnprin(3,amin);  
}
```

End of the fitting routine.

Beginning of the data file *1phase.data.txt* read in the fitting routine

FitTurbulentLiquid.cxx.

Example data: $800 \times 250 \mu\text{m}$ tube.

```
0.000339
0.03
18
10473.0 1.89018 1.01060 1.03417E-01 7.56029E-05
9384.45 1.89897 1.01166 1.04292E-01 8.05355E-05
8648.96 1.89984 1.01263 1.04410E-01 8.49943E-05
8047.04 1.90332 1.01348 1.04795E-01 8.88432E-05
7704.89 1.90095 1.01406 1.04558E-01 9.16310E-05
7555.86 1.90817 1.01423 1.05247E-01 9.23129E-05
7298.85 1.91129 1.01467 1.05530E-01 9.43319E-05
6911.06 1.91365 1.01541 1.05753E-01 9.78064E-05
6747.53 1.90207 1.01596 1.04705E-01 1.00485E-04
6409.18 1.91629 1.01653 1.06005E-01 1.03014E-04
5989.33 1.91856 1.01764 1.06216E-01 1.08241E-04
6035.52 1.90150 1.01778 1.04687E-01 1.09094E-04
5564.14 1.91832 1.01899 1.06214E-01 1.14621E-04
5476.32 1.90005 1.01964 1.04583E-01 1.17837E-04
4923.77 1.91832 1.02145 1.06240E-01 1.26451E-04
4615.57 1.89609 1.02338 1.04259E-01 1.35849E-04
4139.90 1.91373 1.02571 1.05889E-01 1.47213E-04
3930.55 1.88882 1.02787 1.03625E-01 1.57608E-04
```

End of the data file.

B.2 Fitting Algorithm for Flow Boiling Heat Transfer Data

Beginning of the fitting routine in a file *FitTwoPhase.cxx*.

```
// C++ SOURCE CODE FOR FITTING HEAT TRANSFER DATA WITH MINUIT [68]
// FLOW-BOILING IN THE NUCLEATE BOILING DOMINATED REGIME
//
// EXAMPLE DATA IN FILE 2phase_data.txt - 800x250um TUBE
// GLOBAL VARIABLES
// -----
double M[200], q[200], x_out[200], alpha[200], d_alpha[200];
double rho_l[200], rho_v[200], lam_l[200], lam_v[200];
double eta_l[200], eta_v[200], cp_l[200], cp_v[200];
double Re_l[200], Re_v[200], Pr_l[200], Pr_v[200];
double dw[200], dc[200], Ra[200];
double L, Ts, ps, dhv, sigma, pred, rd_l, rd_v, exp_l, exp_v;
int nrows;
double v[10], verr[10], vlow[10], vhigh[10];
char name[20];
double Chi2;

// FUNCTION HEADERS
// -----
double alpha_l0(double dw, double rd_l, double Re_l, double Pr_l, double lam_l)
double alpha_v0(double dw, double rd_v, double Re_v, double Pr_v, double lam_v)
double alpha_zc(double xz, double rho_l, double rho_v, double alpha_l0, double alphav0);
double alpha_znb(double dw, double dc, double qz, double Ra, double CF, double Lap,
double exc)
double alpha_int(double dw, double dc, double Ra, double q, double Re_l, double Pr_l,
double lam_l, double Re_v, double Pr_v, double lam_v, double xout,
double rho_l, double rho_v, double M, double *par)

int Fitting();
int FitTwoPhase();

// HEADER FILES
// -----
#ifdef __CINT__
#include "TVirtualFitter.h"
#include "TMath.h"
#include "TStopwatch.h"
#include <stdlib.h>
#include <stdio.h>
#include <fstream.h>

int main()
{
    return FitTwoPhase();
}
#endif
```

```

double alpha_l0(double dw, double rd_l, double Re_l, double Pr_l, double lam_l)
// Sub-routine: Single-phase HTC for saturated liquid phase at the same mass flux
// Nusselt number for turbulent liquid flow according to Eq. (5.2)
// Factor KT for wall temperature correction omitted
{
    double Nu;
    Nu = 0.012*(pow(Re_l,0.87*rd_l)-280)*pow(Pr_l,0.4)*(1+pow(dw/L,2./3.));
    double value = Nu*lam_l/dw;
    return value;
}

```

```

double alpha_v0(double dw, double rd_v, double Re_v, double Pr_v, double lam_v)
// Sub-routine: Single-phase HTC for saturated vapor phase at the same mass flux
// Nusselt number for turbulent vapor flow according to Eq. (5.3)
{
    double Nu;
    Nu = 0.0214*(pow(Re_v,0.8*rd_v)-100)*pow(Pr_v,0.4)*(1+pow(dw/L,2./3.));
    double value = Nu*lam_v/dw;
    return value;
}

```

```

double alpha_zc(double xz, double rho_l, double rho_v, double alpha_l0, double alpha_v0)
// Sub-routine: Calculation of the local convective boiling HTC - Eq. (5.8)
// Local data are labeled with <z>
{
    double termc1 = pow(pow((1-xz),1.5)+1.9*pow(xz,0.6)*pow(rho_l/rho_v,0.35),-2.2);
    double termc2 = pow(alpha_v0/alpha_l0*(1+8*pow(1-xz,0.7)*pow(rho_l/rho_v,0.67)),-2.);
    double value = alpha_l0*pow(pow(1-xz,0.01)*termc1+pow(xz,0.01)*termc2,-0.5);
    return value;
}

```

```

double alpha_znb(double dw, double dc, double qz, double Ra, double CF, double Lap,
double exc)
// Sub-routine: Calculation of the local nucleate boiling HTC - Eq. (5.29)
// Local data are labeled with <z>
{
    static double a0 = 3870.;           /* Reference pool boiling HTC */
    static double q0 = 10000.;          /* Reference pool boiling heat flux */
    static double d0 = 0.01;            /* Reference diameter */
    static double Ra0 = 1.0E-06;        /* Reference roughness */

    double npv = 0.7-0.13*pow(10,0.48*pred);
    double Fpv = 2.816*pow(pred,0.45)+(3.4+1.7/(1-pow(pred,7.)))*pow(pred,3.7);
    double Fd = pow(dw*d0/pow(dc,2.),0.4)*(1-exp(-exc*dc/Lap));
    double Fw = pow(Ra/Ra0,0.133);
    double value = a0*CF*pow(qz/q0,npv)*Fpv*Fd*Fw;
    return value;
}

```

```

double alpha_int(double dw, double dc, double Ra, double q, double Rel, double Prl,
                 double laml, double Rev, double Prv, double lamv, double xout,
                 double rhol, double rhov, double M, double *par)
// Sub-routine: Fit function; numerical integration of local 2-phase HTCs
// Local data are labeled with <z>
{
    static int N = 20;                                /* 20 heater sections */
    static double pi = 3.1415;
    double xz[20];
    double lz[20];
    double qz[20];
    double azc[20], aznb[20], az[20];
    double alpham;
    double L_it, dL;
    double value = 0;
    int j, k;

    rd_l = pow(dw/dc, exp_l); /* Roughness factor for Re-exponent / turb. liquid flow */
    rd_v = pow(dw/dc, exp_v); /* Roughness factor for Re-exponent / turb. vapor flow */
    double al0 = alpha_l0(dw, rd_l, Rel, Prl, laml); /* Single-phase liquid HTC */
    double av0 = alpha_v0(dw, rd_v, Rev, Prv, lamv); /* Single-phase vapor HTC */
    double Lap = pow(sigma/(9.81*(rhol-rhov)), 0.5); /* Laplace constant */
    double Qz = q*pi*dw*L/N; /* Same heat load in each section */

    for (j=0; j<N; j++) {
        xz[j] = (j+0.5)*xout/N; /* Mean x in section j */
        azc[j] = alpha_zc(xz[j], rhol, rhov, al0, av0); /* Local convective boiling HTC */
        lz[j] = L/N; /* Start value for section length */
    }

    k = 0;
    do {
        if (k==0) {
            dL=1;
            L_it = L;
        }
        else {
            dL = 1-L_it/L;
        }
        alpham = 0;
        k += 1;
        for (j=0; j<N; j++) {
            lz[j] = lj[j]*L/L_it; /* Section length */
            qz[j] = Qj/(pi*dw*lj[j]); /* Local heat flux */
            aznb[j] = alpha_znb(dw, dc, qz[j], Ra, par[0], Lap, par[1]); /* Local nucl.
boiling HTC */
            az[j] = pow(pow(azc[j], 3.) + pow(aznb[j], 3.), 1./3.); /* Local flow-boiling HTC */
            alpham += az[j]*lz[j]/L; /* Integrated flow-boiling HTC */
        }
        L_it=0;
        for (j=0; j<N; j++) {
            lz[j] = alpham*L/(N*az[j]); /* Section length */
            L_it += lz[j];
        }
    }
}

```

```
    }  
    while (fabs(dL)>0.01 && k<10);      /* Iteration until dL<1%, loop limit of max. 10  
iterations */  
    value = alpham;  
    return value;  
}
```

```

void fcn(Int_t &npar, Double_t *gin, Double_t &f, Double_t *par, Int_t iflag)
// Sub-routine: Minimization function
{
    int i;
    double chisq = 0;
    double delta;
    for (i=0; i<nrows; i++) {
        delta = (alpha[i]-alpha_int(dw[i],dc[i],Ra[i],q[i],Re_l[i],Pr_l[i],lam_l[i],
            Re_v[i],Pr_v[i],lam_v[i],x_out[i], rho_l[i],rho_v[i],
M[i],par))/d.alpha[i];
        chisq += delta*delta;
    }
    Chi2 = chisq;
    f = chisq;
}

int Fitting()
// Sub-routine: Fitting call to Minuit
{
    TStopwatch timer;
    // Initialize TMinuit via generic fitter interface with max. 5 parameters
    TVirtualFitter *minuit = TVirtualFitter::Fitter(0,5);
    printf("Starting timer\n");
    timer.Start();
    minuit->SetFCN(fcn);

    // Set starting values and step sizes for parameters
    minuit->SetParameter(0,"CF" , 0.93, 0.001,0,0); /* Fluid factor CF in Eq. (5.29) */
    minuit->SetParameter(1,"exc", 0.45, 0.001,0,0); /* Exponent c in Eq. (5.27) */

    // Request FCN to read in data (IFLAG=1)
    double arglist[200];
    arglist[0] = 1;
    minuit->ExecuteCommand("CALL FCN", arglist, 1);

    // Fix parameters
    minuit->FixParameter(0);
    //minuit->FixParameter(1); /* Adapt comments to set number of free parameters */

    // Execute minimization
    arglist[0] = 0;
    minuit->ExecuteCommand("SET PRINT", arglist, 1);
    minuit->ExecuteCommand("MIGRAD", arglist, 0);
    minuit->ExecuteCommand("MINOS", arglist, 0);

    // Retrieve parameter values and errors
    minuit->GetParameter(0, name, v[0], verr[0], vlow[0], vhigh[0]);
    minuit->GetParameter(1, name, v[1], verr[1], vlow[1], vhigh[1]);
    printf("    NAME      VALUE      ERROR\n");
    printf("    CF        %1.5e    %1.5e\n", v[0], verr[0]);
    printf("    exc       %1.5e    %1.5e\n", v[1], verr[1]);
    printf("Time at the end of the job = %f seconds\n", timer.CpuTime());
    return 0;
}

```

}

```

int FitTwoPhase()
// Main routine
{
    // Reading data from the file
    int i = 0;
    char* file = "2phase_data.txt";
    std::ifstream in(file);
    in >> exp_l;
    in >> exp_v;
    in >> L;
    in >> ps;
    in >> Ts;
    in >> sigma;
    in >> nrows;
    while (1) {
        in >> dw[i] >> dc[i] >> Ra[i] >> M[i] >> q[i] >> x_out[i] >> alpha[i] >>
d.alpha[i]
        >> rho_l[i] >> rho_v[i] >> lam_l[i] >> lam_v[i] >> eta_l[i] >> eta_v[i] >>
cp_l[i]
        >> cp_v[i];
        if (!in.good()) break;
        i++;
    }
    in.close();

    // Calculation of Re and Pr numbers
    for (i=0; i<nrows; i++) {
        Re_l[i] = M[i]*dw[i]/eta_l[i];
        Re_v[i] = M[i]*dw[i]/eta_v[i];
        Pr_l[i] = eta_l[i]*cp_l[i]/lam_l[i];
        Pr_v[i] = eta_v[i]*cp_v[i]/lam_v[i];
    }

    // Reduced pressure for argon
    pred = ps/4905800.;

    Fitting();

    return 0;
}

```

End of the fitting routine.

0.22	0.000339	0.000283	9.00E-06	506.34	25035	0.179	11350	301	1127.6	73.93	7.943E-02	1.055E-02	1.020E-04	1.096E-05	1404.95	935.00
0.55	0.000339	0.000283	9.00E-06	519.75	26794	0.179	11511	300	1127.7	73.89	7.944E-02	1.055E-02	1.020E-04	1.096E-05	1404.75	934.76
0.03	0.000339	0.000283	9.00E-06	533.18	30506	0.196	11908	269	1127.7	73.89	7.944E-02	1.055E-02	1.020E-04	1.096E-05	1404.75	934.76
1485656	0.000339	0.000283	9.00E-06	519.15	35068	0.247	12176	248	1127.4	74.00	7.941E-02	1.055E-02	1.020E-04	1.096E-05	1405.28	935.41
4.17E-03	0.000339	0.000283	9.00E-06	517.44	39303	0.283	12635	235	1127.2	74.10	7.938E-02	1.056E-02	1.019E-04	1.097E-05	1405.76	936.01
14	0.000339	0.000283	9.00E-06	509.62	42177	0.317	12958	231	1127.1	74.15	7.936E-02	1.056E-02	1.019E-04	1.097E-05	1406.05	936.37
	0.000339	0.000283	9.00E-06	539.23	48980	0.334	13893	228	1127.1	74.13	7.937E-02	1.056E-02	1.019E-04	1.097E-05	1405.91	936.20
	0.000339	0.000283	9.00E-06	536.87	54739	0.382	14612	224	1127.1	74.16	7.936E-02	1.056E-02	1.019E-04	1.097E-05	1406.05	936.38
	0.000339	0.000283	9.00E-06	529.57	61094	0.443	15408	223	1127.0	74.19	7.936E-02	1.056E-02	1.018E-04	1.097E-05	1406.21	936.58
	0.000339	0.000283	9.00E-06	536.30	67234	0.481	16198	225	1127.0	74.19	7.935E-02	1.056E-02	1.018E-04	1.097E-05	1406.23	936.61
	0.000339	0.000283	9.00E-06	548.41	77316	0.541	17502	226	1127.0	74.21	7.935E-02	1.056E-02	1.018E-04	1.097E-05	1406.32	936.71
	0.000339	0.000283	9.00E-06	539.38	82625	0.598	18124	228	1127.0	74.20	7.935E-02	1.056E-02	1.018E-04	1.097E-05	1406.30	936.68
	0.000339	0.000283	9.00E-06	530.35	88461	0.660	19081	234	1127.1	74.17	7.936E-02	1.056E-02	1.019E-04	1.097E-05	1406.11	936.45
	0.000339	0.000283	9.00E-06	535.35	95505	0.706	20056	238	1127.1	74.13	7.937E-02	1.056E-02	1.019E-04	1.097E-05	1405.92	936.21

End of the data file.

C EXPERIMENTAL DATA OF HEAT TRANSFER MEASUREMENTS

Table C.1: Summary of Single-phase Heat Transfer Data

\dot{M} [kg/m ² s]	\bar{p}_f [Pa]	\bar{T}_f [K]	Re [-]	\dot{Q} [W]	$\Delta T_{m,w}$ [K]	$\bar{\alpha}$ [W/m ² K]	$\bar{\alpha}/k$ [%]	$\Delta\bar{\alpha}_{stat}$ [%]	$\Delta\bar{\alpha}_{sys}$ [%]	ΔRe_{stat} [%]	ΔRe_{sys} [%]
800 × 250 μm Tube, Laminar Liquid Flow.											
995	1498838	94.73	1575	0.501	6.92	2263	105.9	1.9	8.0	1.2	16.6
918	1497286	94.84	1459	0.501	7.24	2165	105.6	1.9	8.0	1.3	16.6
838	1495361	95.02	1338	0.501	7.58	2068	105.3	1.9	8.0	1.4	16.6
757	1493053	95.25	1216	0.501	7.88	1990	105.1	1.8	8.0	1.6	16.6
680	1485257	95.55	1102	0.501	8.31	1886	104.9	1.8	8.0	1.9	16.6
601	1482463	95.96	984	0.501	8.66	1811	104.7	1.8	7.9	2.1	16.6
516	1482215	96.60	860	0.501	9.14	1715	104.4	1.8	7.9	2.3	16.6
440	1481445	97.40	748	0.501	9.62	1631	104.2	1.8	7.9	2.7	16.6
357	1479755	98.67	628	0.501	10.21	1537	104.0	1.8	7.9	3.2	16.6
267	1477722	100.82	496	0.502	10.89	1441	103.7	2.0	7.9	4.0	16.6
205	1475111	103.22	406	0.502	11.53	1362	103.5	2.7	7.8	5.5	16.6
800 × 250 μm Tube, Turbulent Liquid Flow.											
5115	1222997	104.44	10473	2.007	3.12	20102	152.0	2.3	12.3	0.3	16.6
4661	1283615	103.81	9384	2.007	3.44	18289	147.3	1.9	11.8	0.2	16.6
4305	1321261	103.74	8649	2.007	3.72	16910	143.7	1.8	11.5	0.5	16.6
4035	1393244	103.49	8047	2.008	3.96	15877	141.1	2.1	11.2	0.6	16.6
3846	1367742	103.65	7705	2.008	4.13	15204	139.3	1.6	11.1	0.5	16.6
3822	1416751	103.16	7556	2.008	4.18	15048	138.9	1.6	11.0	0.4	16.6
3712	1428857	102.95	7299	2.007	4.30	14604	137.8	1.4	10.9	0.4	16.6
3530	1448472	102.80	6911	2.008	4.52	13899	135.9	1.4	10.7	0.4	16.6
3378	1412693	103.57	6748	2.008	4.69	13400	134.6	1.6	10.6	0.6	16.6
3289	1475610	102.62	6409	2.008	4.85	12961	133.5	1.3	10.5	0.4	16.6
3086	1494740	102.47	5989	2.008	5.18	12138	131.4	1.3	10.3	0.4	16.6
3020	1446007	103.60	6036	2.008	5.23	12014	131.1	2.6	10.3	1.6	16.6
2867	1513213	102.49	5564	2.008	5.58	11266	129.1	1.8	10.1	0.4	16.6
2735	1470844	103.69	5476	2.008	5.78	10872	128.1	1.1	10.0	0.5	16.6
2538	1541783	102.48	4924	2.008	6.32	9941	125.7	1.3	9.8	0.5	16.6
2291	1500279	103.96	4616	2.008	6.91	9092	123.5	3.7	9.6	2.0	16.6
2120	1582494	102.77	4140	2.009	7.63	8240	121.3	1.1	9.4	0.6	16.6
1927	1528346	104.46	3931	2.009	8.29	7590	119.6	2.3	9.2	1.2	16.6
800 × 250 μm Tube, Turbulent Vapor Flow.											
591	1315230	133.66	17406	0.197	2.91	2122	105.5	4.9	8.0	1.8	16.6
517	1355233	134.77	15086	0.197	3.01	2050	105.3	4.9	8.0	2.1	16.6

Continued on next page.

Table C.1: Continued

\dot{M} [kg/m ² s]	\bar{p}_f [Pa]	\bar{T}_f [K]	Re [-]	\dot{Q} [W]	$\Delta T_{m,w}$ [K]	$\bar{\alpha}$ [W/m ² K]	$\bar{\alpha}/\bar{k}$ [%]	$\Delta\bar{\alpha}_{stat}$ [%]	$\Delta\bar{\alpha}_{sys}$ [%]	ΔRe_{stat} [%]	ΔRe_{sys} [%]
800 × 500 μm Tube, Laminar Liquid Flow.											
434	1396427	135.99	12554	0.197	3.22	1917	105.0	4.9	8.0	2.5	16.6
377	1418551	136.91	10835	0.197	3.43	1798	104.6	5.1	7.9	2.9	16.6
275	1452157	139.00	7774	0.197	4.03	1533	104.0	5.0	7.9	4.1	16.6
210	1469100	141.22	5856	0.197	4.82	1280	103.3	5.0	7.8	5.1	16.6
800 × 500 μm Tube, Turbulent Liquid Flow.											
671	1517994	96.23	1917	0.503	5.40	1682	102.1	1.9	2.6	0.5	5.6
595	1516921	95.91	1686	0.503	5.73	1586	102.0	1.9	2.4	0.6	5.6
543	1515883	95.64	1528	0.503	5.97	1522	101.9	2.0	2.4	0.6	5.6
489	1513740	95.35	1366	0.503	6.26	1451	101.8	2.0	2.3	0.7	5.6
418	1510005	95.04	1159	0.503	6.71	1355	101.7	2.0	2.2	0.8	5.6
358	1506031	94.86	986	0.503	7.16	1270	101.6	1.9	2.1	1.1	5.6
302	1502381	94.78	832	0.503	7.62	1192	101.5	1.9	2.1	1.2	5.6
232	1498480	95.00	641	0.503	8.22	1106	101.4	1.9	2.0	1.5	5.6
800 × 500 μm Tube, Turbulent Vapor Flow.											
2098	1976807	107.68	7988	2.002	4.98	7265	109.2	1.6	9.3	0.2	5.6
1975	1916253	107.63	7517	2.002	5.28	6843	108.7	1.1	8.8	0.4	5.6
1908	1867135	107.50	7242	2.003	5.47	6613	108.4	1.2	8.5	0.5	5.6
1792	1872431	107.26	6763	2.003	5.83	6204	107.9	1.0	8.0	0.3	5.6
1675	1813041	107.00	6285	2.003	6.25	5789	107.3	1.1	7.5	0.3	5.6
1603	1801451	106.67	5969	2.003	6.55	5520	107.0	2.0	7.1	0.3	5.6
1501	1808642	106.40	5550	2.003	7.02	5151	106.5	1.4	6.7	0.3	5.6
1443	1810569	105.98	5280	2.003	7.31	4948	106.3	0.9	6.4	0.3	5.6
1369	1893054	105.63	4960	2.003	7.77	4655	105.9	0.8	6.1	0.3	5.6
1242	1921461	105.70	4506	2.003	8.56	4224	105.4	1.8	5.5	0.6	5.6
800 × 500 μm Tube, Turbulent Vapor Flow.											
399	1568454	132.52	20178	0.302	3.72	1463	101.9	3.4	2.3	0.8	5.6
375	1556656	132.84	18933	0.302	3.97	1374	101.7	3.0	2.2	1.0	5.6
341	1545090	133.05	17200	0.302	4.31	1264	101.6	3.0	2.1	1.0	5.6
317	1538133	133.17	15999	0.302	4.60	1185	101.5	2.9	2.0	1.2	5.6
286	1531208	133.32	14412	0.302	5.03	1083	101.4	2.9	2.0	1.3	5.6
260	1525872	133.48	13105	0.302	5.46	998	101.3	2.9	1.9	1.3	5.6
235	1521492	133.65	11838	0.302	5.97	913	101.2	2.9	1.8	1.5	5.6
207	1516978	133.95	10436	0.302	6.66	818	101.0	2.8	1.7	1.8	5.6
170	1511967	134.55	8549	0.302	7.89	692	100.9	2.8	1.6	2.3	5.6
148	1508350	135.08	7386	0.302	8.93	611	100.8	2.7	1.6	2.8	5.6

Table C.2: Summary of Flow-boiling Heat Transfer Data

\dot{M} [kg/m ² s]	T_0 [K]	\dot{Q} [W]	$\Delta T_{m,w}$ [K]	x_{in} [-]	x_{out} [-]	$\bar{\alpha}$ [W/m ² K]	$\bar{\alpha}/\bar{k}$ [%]	$\Delta\bar{\alpha}_{stat}$ [%]	$\Delta\bar{\alpha}_{sys}$ [%]	$\Delta x_{out,stat}$ [-]	$\Delta x_{out,sys}$ [-]
800 × 250 μm Tube, $\dot{M} = 380$ kg/m ² s.											
363.99	123.79	0.594	1.83	-0.028	0.185	10168	126.3	3.2	9.3	0.020	0.013
374.87	123.83	0.693	1.97	-0.038	0.204	11003	128.5	3.0	9.6	0.018	0.013
384.55	123.86	0.800	2.09	-0.046	0.226	11965	130.9	2.8	9.8	0.021	0.012
380.53	123.91	0.914	2.21	-0.044	0.271	12963	133.5	2.6	10.1	0.023	0.011
384.13	123.92	1.037	2.34	-0.047	0.307	13878	135.9	2.4	10.4	0.025	0.011
375.08	123.95	1.167	2.46	-0.040	0.368	14816	138.3	2.3	10.6	0.024	0.009
373.64	123.96	1.305	2.59	-0.039	0.420	15748	140.7	2.2	10.9	0.027	0.009
373.31	123.98	1.450	2.72	-0.039	0.472	16688	143.2	2.1	11.1	0.031	0.008
378.46	124.00	1.604	2.84	-0.043	0.514	17680	145.7	2.0	11.4	0.028	0.007
379.93	124.03	1.765	2.97	-0.044	0.567	18623	148.2	1.9	11.6	0.030	0.007
379.26	124.04	1.934	3.10	-0.044	0.628	19552	150.6	1.8	11.9	0.033	0.007
383.07	124.05	2.112	3.23	-0.046	0.679	20495	153.0	1.7	12.1	0.034	0.007
381.43	124.05	2.296	3.35	-0.045	0.748	21436	155.4	1.7	12.4	0.035	0.007
383.88	124.06	2.490	3.48	-0.047	0.808	22366	157.8	1.6	12.7	0.041	0.008
381.20	124.06	2.691	3.62	-0.044	0.886	23240	160.1	1.5	12.9	0.049	0.009
383.89	124.06	2.900	3.76	-0.046	0.949	24130	162.4	1.5	13.1	0.044	0.010
800 × 250 μm Tube, $\dot{M} = 530$ kg/m ² s.											
506.34	123.71	0.800	2.21	-0.027	0.179	11350	129.3	2.7	9.7	0.013	0.013
519.75	123.70	0.856	2.33	-0.035	0.179	11511	129.8	2.6	9.8	0.016	0.013
533.18	123.70	0.975	2.56	-0.043	0.196	11908	130.8	2.3	9.9	0.013	0.013
519.15	123.73	1.120	2.88	-0.035	0.247	12176	131.5	2.0	10.0	0.015	0.012
517.44	123.75	1.256	3.11	-0.034	0.283	12635	132.7	1.9	10.1	0.017	0.011
509.62	123.77	1.348	3.26	-0.029	0.317	12958	133.5	1.8	10.2	0.017	0.010
539.23	123.76	1.565	3.53	-0.045	0.334	13893	135.9	1.6	10.5	0.014	0.010
536.87	123.77	1.749	3.75	-0.044	0.382	14612	137.8	1.5	10.7	0.018	0.009
529.57	123.78	1.952	3.97	-0.040	0.443	15408	139.8	1.4	10.9	0.018	0.008
536.30	123.78	2.148	4.15	-0.043	0.481	16198	141.9	1.4	11.1	0.019	0.008
548.41	123.78	2.470	4.42	-0.049	0.541	17502	145.3	1.3	11.4	0.021	0.007
539.38	123.78	2.640	4.56	-0.044	0.598	18124	146.9	1.3	11.6	0.022	0.007
530.35	123.77	2.826	4.64	-0.038	0.660	19081	149.3	1.2	11.9	0.023	0.007
535.35	123.76	3.051	4.76	-0.041	0.706	20056	151.9	1.2	12.1	0.023	0.007
800 × 250 μm Tube, $\dot{M} = 670$ kg/m ² s.											
674.55	123.80	1.167	3.15	-0.038	0.187	11603	130.0	2.0	9.9	0.011	0.013

Continued on next page.

Table C.2: Continued

\dot{M} [kg/m ² s]	T_0 [K]	\dot{Q} [W]	$\Delta T_{m,w}$ [K]	x_{in} [-]	x_{out} [-]	$\bar{\alpha}$ [W/m ² K]	$\bar{\alpha}/\bar{k}$ [%]	$\Delta\bar{\alpha}_{stat}$ [%]	$\Delta\bar{\alpha}_{sys}$ [%]	$\Delta x_{out,stat}$ [-]	$\Delta x_{out,sys}$ [-]
676.75	123.85	1.305	3.45	-0.039	0.212	11830	130.6	1.9	10.0	0.011	0.012
671.01	123.90	1.451	3.78	-0.038	0.244	12020	131.1	1.6	10.0	0.012	0.012
663.70	123.93	1.604	4.11	-0.035	0.281	12223	131.6	1.4	10.1	0.012	0.011
671.03	123.96	1.765	4.40	-0.039	0.305	12558	132.5	1.4	10.2	0.012	0.011
668.35	124.00	1.935	4.71	-0.038	0.341	12863	133.3	1.3	10.3	0.014	0.010
665.82	124.04	2.113	5.02	-0.037	0.379	13180	134.1	1.2	10.4	0.014	0.009
665.93	124.07	2.298	5.33	-0.037	0.416	13493	134.9	1.1	10.5	0.015	0.009
676.90	124.11	2.491	5.61	-0.042	0.441	13907	136.0	1.0	10.6	0.014	0.008
670.76	124.05	2.691	5.52	-0.039	0.488	23956	161.9	1.6	13.1	0.017	0.008
665.44	124.08	2.900	3.69	-0.037	0.537	24613	163.6	1.5	13.3	0.016	0.007
672.03	124.08	3.117	3.85	-0.039	0.571	25311	165.4	1.4	13.5	0.018	0.007
667.12	124.03	3.342	4.02	-0.036	0.623	26004	167.2	1.4	13.7	0.017	0.007
673.17	124.05	3.575	4.18	-0.039	0.660	26780	169.2	1.3	13.9	0.020	0.007
667.85	124.08	3.817	4.34	-0.037	0.716	27554	171.2	1.3	14.1	0.020	0.007
666.71	124.09	4.004	4.45	-0.036	0.755	28133	172.7	1.2	14.3	0.021	0.007
664.27	124.11	4.195	4.57	-0.035	0.798	28741	174.3	1.2	14.4	0.023	0.008
668.98	124.14	4.391	4.68	-0.037	0.829	29348	175.9	1.2	14.6	0.023	0.008
677.89	124.08	4.592	4.80	-0.040	0.853	29940	177.4	1.2	14.8	0.023	0.009
685.01	124.10	4.798	4.91	-0.043	0.881	30570	179.0	1.1	14.9	0.022	0.009
681.70	124.11	5.008	5.01	-0.041	0.928	31281	180.9	1.1	15.1	0.024	0.010
679.30	124.12	5.223	5.09	-0.040	0.974	32095	183.0	1.1	15.4	0.027	0.011
800 × 250 μm Tube, $\dot{M} = 830$ kg/m ² s.											
820.66	123.88	1.529	2.63	-0.039	0.203	18215	147.1	2.1	11.5	0.010	0.013
820.89	123.86	1.687	2.79	-0.040	0.228	18896	148.9	2.0	11.7	0.010	0.012
827.38	123.85	1.852	2.96	-0.042	0.250	19611	150.7	1.9	11.9	0.010	0.012
810.36	123.86	2.026	3.14	-0.036	0.291	20201	152.2	1.8	12.1	0.011	0.011
824.70	123.86	2.207	3.30	-0.040	0.309	20964	154.2	1.7	12.3	0.011	0.010
823.44	123.86	2.397	3.47	-0.040	0.341	21654	156.0	1.6	12.5	0.011	0.010
822.85	123.88	2.594	3.63	-0.039	0.373	22396	157.9	1.5	12.7	0.012	0.009
822.32	123.87	2.800	3.79	-0.039	0.407	23126	159.8	1.5	12.9	0.011	0.009
828.83	123.85	3.013	3.95	-0.041	0.435	23897	161.8	1.4	13.1	0.012	0.008
821.04	123.87	3.235	4.11	-0.038	0.478	24613	163.6	1.4	13.3	0.013	0.008
830.00	123.83	3.465	4.27	-0.040	0.506	25390	165.7	1.3	13.5	0.013	0.007
830.83	123.86	3.702	4.43	-0.041	0.543	26153	167.6	1.3	13.7	0.013	0.007
831.99	123.76	3.948	4.59	-0.039	0.582	26893	169.5	1.2	13.9	0.014	0.007
831.61	123.79	4.201	4.75	-0.039	0.623	27678	171.6	1.2	14.1	0.016	0.007

Continued on next page.

Table C.2: Continued

\dot{M} [kg/m ² s]	T_0 [K]	\dot{Q} [W]	$\Delta T_{m,w}$ [K]	x_{in} [-]	x_{out} [-]	$\bar{\alpha}$ [W/m ² K]	$\bar{\alpha}/\bar{k}$ [%]	$\Delta\bar{\alpha}_{stat}$ [%]	$\Delta\bar{\alpha}_{sys}$ [%]	$\Delta x_{out,stat}$ [-]	$\Delta x_{out,sys}$ [-]
830.17	123.83	4.463	4.91	-0.039	0.666	28468	173.6	1.1	14.4	0.015	0.007
828.41	123.87	4.733	5.06	-0.039	0.712	29282	175.7	1.1	14.6	0.015	0.007
828.32	123.90	5.012	5.21	-0.038	0.757	30110	177.9	1.1	14.8	0.018	0.007
842.42	123.86	5.299	5.36	-0.042	0.784	30935	180.0	1.0	15.0	0.017	0.008
842.03	123.88	5.594	5.51	-0.042	0.831	31794	182.2	1.0	15.3	0.017	0.008
842.18	123.83	5.899	5.65	-0.041	0.879	32678	184.5	1.0	15.5	0.020	0.009
839.88	123.84	6.212	5.76	-0.040	0.932	33765	187.3	1.0	15.8	0.019	0.010
833.67	123.85	6.533	5.88	-0.038	0.993	34794	190.0	0.9	16.1	0.020	0.011
<hr/>											
800 × 250 μm Tube, $\dot{M} = 1025$ kg/m ² s.											
1018.16	123.70	1.167	2.00	-0.034	0.113	18239	147.2	3.1	11.4	0.008	0.014
1001.43	123.62	1.451	2.56	-0.029	0.158	17734	145.9	3.1	11.4	0.013	0.014
1060.07	123.47	1.849	3.06	-0.053	0.171	18935	149.0	2.1	11.7	0.012	0.013
1017.25	123.64	2.112	3.51	-0.044	0.225	18813	148.6	1.7	11.7	0.013	0.012
1015.17	123.66	2.392	3.85	-0.044	0.262	19428	150.2	1.5	11.9	0.015	0.011
987.38	123.67	2.639	4.15	-0.036	0.312	19904	151.5	1.4	12.1	0.019	0.010
1018.35	123.62	2.900	4.37	-0.044	0.326	20775	153.7	1.3	12.3	0.021	0.010
1040.07	123.62	3.172	4.61	-0.049	0.347	21528	155.7	1.3	12.5	0.024	0.010
1028.38	123.69	3.457	4.87	-0.045	0.393	22205	157.4	1.2	12.7	0.028	0.009
1032.66	123.70	3.694	5.05	-0.044	0.422	22900	159.2	1.1	12.9	0.029	0.009
1002.30	123.69	3.939	5.26	-0.035	0.478	23423	160.6	1.1	13.0	0.032	0.008
1027.98	123.64	4.193	5.41	-0.041	0.491	24263	162.7	1.1	13.2	0.035	0.008
1034.69	123.61	4.455	5.58	-0.042	0.520	24990	164.6	1.0	13.4	0.037	0.007
1017.80	123.60	4.725	5.74	-0.037	0.569	25748	166.6	1.0	13.7	0.040	0.007
1035.55	123.57	5.003	5.90	-0.041	0.590	26560	168.7	1.0	13.9	0.043	0.007
1030.23	123.55	5.289	6.04	-0.039	0.632	27430	170.9	1.0	14.1	0.046	0.007
1030.59	123.53	5.584	6.17	-0.038	0.669	28334	173.3	0.9	14.4	0.049	0.007
1032.67	123.53	5.889	6.30	-0.038	0.707	29272	175.7	0.9	14.6	0.051	0.007
1028.86	123.54	6.201	6.42	-0.037	0.751	30253	178.2	0.9	14.9	0.054	0.007
1008.83	123.56	6.522	6.51	-0.031	0.815	31363	181.1	0.9	15.2	0.057	0.008
1048.22	123.53	6.851	6.60	-0.041	0.814	32490	184.0	0.9	15.5	0.060	0.008
1032.01	123.55	7.189	6.70	-0.036	0.875	33605	186.9	0.8	15.8	0.063	0.009
1029.84	123.54	7.536	6.74	-0.035	0.923	34994	190.5	0.9	16.2	0.066	0.010
1031.80	123.53	7.891	6.81	-0.035	0.967	36266	193.8	0.8	16.5	0.068	0.011
<hr/>											
800 × 500 μm Tube, $\dot{M} = 320$ kg/m ² s.											
320.89	124.23	3.357	2.15	-0.046	0.320	28218	135.8	5.9	7.8	0.011	0.010

Continued on next page.

Table C.2: Continued

\dot{M} [kg/m ² s]	T_0 [K]	\dot{Q} [W]	$\Delta T_{m,w}$ [K]	x_{in} [-]	x_{out} [-]	$\bar{\alpha}$ [W/m ² K]	$\bar{\alpha}/\bar{k}$ [%]	$\Delta\bar{\alpha}_{stat}$ [%]	$\Delta\bar{\alpha}_{sys}$ [%]	$\Delta x_{out,stat}$ [-]	$\Delta x_{out,sys}$ [-]
318.97	124.22	3.765	2.32	-0.046	0.367	29312	137.1	5.1	8.0	0.012	0.009
800 \times 500 μ m Tube, \dot{M} = 420 kg/m ² s.											
421.51	122.26	4.198	3.14	-0.058	0.281	24169	130.6	4.7	7.4	0.005	0.011
419.23	122.30	4.890	3.51	-0.059	0.339	25186	131.9	4.5	7.5	0.006	0.010
422.11	122.35	5.638	3.98	-0.062	0.394	25571	132.4	4.1	7.5	0.006	0.009
800 \times 500 μ m Tube, \dot{M} = 525 kg/m ² s.											
526.04	122.32	4.654	3.29	-0.050	0.252	25513	132.3	4.9	7.5	0.004	0.012
524.65	122.35	5.383	3.66	-0.049	0.301	26539	133.6	3.8	7.6	0.005	0.011
524.23	122.41	6.167	4.11	-0.050	0.353	27095	134.3	3.1	7.7	0.004	0.010
800 \times 500 μ m Tube, \dot{M} = 630 kg/m ² s.											
629.94	124.89	6.275	3.60	-0.049	0.303	31468	139.9	3.2	8.4	0.006	0.011
634.37	123.95	5.898	3.04	-0.045	0.279	35055	144.4	3.4	9.0	0.004	0.011
635.98	123.64	5.637	2.96	-0.041	0.267	34393	143.6	3.8	8.9	0.004	0.011
632.53	123.98	5.133	2.70	-0.043	0.240	34352	143.5	4.2	8.9	0.005	0.012
634.83	123.58	4.653	2.55	-0.039	0.215	32892	141.7	5.0	8.6	0.005	0.012
630.28	124.08	4.423	2.42	-0.044	0.201	32985	141.8	5.3	8.6	0.005	0.013

BIBLIOGRAPHY

- [1] Abreu M. et al.: Recent progress in low-temperature silicon detectors. In *Nuclear Physics B (Proceedings Supplements)*, vol. 125C, pp. 169–174, 2003.
- [2] Abt. Werbung und Messen d. VEB Kombinat Pumpen und Verdichter, Halle (editor): *Technisches Handbuch Pumpen*. VEB Verlag Technik, Berlin, 7th ed., 1987.
- [3] Adams T.M., Abdel-Khalik S.I., Jeter S.M. and Qureshi Z.H.: An experimental investigation of single-phase forced convection in microchannels. *Int. J. of Heat Mass Transfer*, 41 (6–7): pp. 851–857, 1998.
- [4] Adams T.M., Dowling M.F., Abdel-Khalik S.I. and Jeter S.M.: Applicability of traditional turbulent single-phase forced convection correlations to non-circular microchannels. *Int. J. of Heat Mass Transfer*, 42: pp. 4411–4415, 1999.
- [5] Auracher H. et al.: Kritische Siedezustände. In *VDI Wärmeatlas*, chap. Hbc1–Hbc32. VDI Verlag, 6th ed., 1991.
- [6] Barber-Nichols: *Product Brochure - Cryogenic Pumps*, 2000.
- [7] Beitz W. and Küttner K.H. (editors): *Dubbel: Taschenbuch für den Maschinenbau*. Springer Verlag, 17th ed., 1998.
- [8] Bhushan B.: *Principles and Applications of Tribology*. John Wiley & Sons, 1999.
- [9] Binneberg A., Buschmann H., Neubert J. and Spörl G.: Autark, kontinuierlich arbeitender Kühler zur störarmen Kühlung von HTSL-SQUID-Sensoren. In *Statusbericht Supraleitung und Tieftemperaturtechnik*. VDI-TZ Technologiezentrum physikalische Technologien, 1996.
- [10] de Boer M.J. et al.: Micromachining of buried micro channels in silicon. *J. of Microelectromechanical Systems*, 9 (1): pp. 94–103, March 2000.
- [11] Borer K. et al.: Charge collection efficiency of irradiated silicon detector operated at cryogenic temperatures. *Nuclear Instruments and Methods*, A 440: pp. 5–16, 2000.
- [12] Borer K. et al.: RD39. Status Report CERN/LHCC 2002-004, CERN, 2002.
- [13] Bowers M.B. and Mudawar I.: High flux boiling in low flow rate, low pressure drop mini-channel and micro-channel heat sinks. *Int. J. of Heat Mass Transfer*, 37 (2): pp. 321–332, 1994.

- [14] Burger J.F.: *Cryogenic microcooling - A micromachined cold stage operating with a sorption compressor in a vapor compression cycle*. Ph.D. thesis, University of Twente, Enschede, The Netherlands, January 2001.
- [15] Cornwell K., Lin S. and Kew P.A.: Two-phase heat transfer to a refrigerant in a 1 mm diameter tube. *Int. J. of Refrigeration*, 24: pp. 51–56, 2001.
- [16] Cryodata Inc.: *GASPAK, Version 3.30*, 1999.
- [17] von Cube H., Steimle F., Lotz H. and Kunis J. (editors): *Lehrbuch der Kältetechnik*, vol. 1 and 2. C.F. Müller Verlag, Heidelberg, 4th ed., 1997.
- [18] Danguy F., Edeline E., Bonhomme C. and Dehouve J.: A coordinated program for development of low cost hydrogen turbomachinery for the vulcain rocket engine family. In *Procs. of the 19th International Cryogenic Engineering Conference (ICEC)*, pp. 541–544. Grenoble, France, July 2002.
- [19] *Dresdner Kolloquium - Bedarf und Möglichkeiten der kryotechnischen Maschinenkühlung für Erzeugnisse mit HTSL-Materialien*. Institut für Luft- und Kältetechnik gGmbH, Dresden, Germany, February 2002.
- [20] Elsner N., Dittmann A. and Huhn J.: *Grundlage der Technischen Thermodynamik*, vol. 1 and 2. Akademie Verlag GmbH, Berlin, 8th ed., 1992.
- [21] Garlock Sealing Technologies: *Product Brochure - Ultra-FlexTM Low-Load Metal Seals*, 2002.
- [22] Ghiaasiaan S.M., Triplett K.A., Abdel-Khalik S.I., LeMouel A. and McCord B.N.: Gas-liquid two-phase flow in microchannels. Part II: void fraction and pressure drop. *Int. J. of Multiphase Flow*, 25: pp. 395–410, 1999.
- [23] Ghiaasiaan S.M., Triplett K.A., Abdel-Khalik S.I. and Sadowski D.L.: Gas-liquid two-phase flow in microchannels. Part I: two-phase flow patterns. *Int. J. of Multiphase Flow*, 25: pp. 377–394, 1999.
- [24] Gnielinski V.: Neue Gleichungen für den Wärme- und Stoffübergang in turbulent durchströmten Rohren und Kanälen. *Forschung Ingenieurwesen*, 41 (1): pp. 8–16, 1975.
- [25] Gorenflo D.: Behältersieden (Sieden bei freier Konvektion). In *VDI Wärmeatlas*, chap. Ha1–Ha26. VDI Verlag, 6th ed., 1991.
- [26] Grohmann S., Herzog R., Niinikoski T.O. and Wobst E.: Kryogene Kühleinrichtung. German Patent DE 102 10 524 C1, August 2003.
- [27] Grohmann S. et al.: Detector development for TOTEM Roman pots. In *Procs. of the IXth Blois Workshop on Elastic and Diffractive Scattering*, pp. 363–374. Institute of Physics AS CR, Pruhonice near Prague, Czech Republic, June 2001.

- [28] Grohmann S. et al.: Cooling power distribution from a small cryocooler. In *Procs. of the 19th International Cryogenic Engineering Conference (ICEC)*, pp. 411–414. Grenoble, France, July 2002.
- [29] Hausen H.: Neue Gleichungen für die Wärmeübertragung bei freier oder erzwungener Strömung. *Allgemeine Wärmetechnik*, 9 (4–5): pp. 75–79, 1959.
- [30] Hetsroni G. (editor): *Handbook of Multiphase Systems*. McGraw-Hill, New York, 1982.
- [31] Hetsroni G., Peles Y.P. and Yarin L.P.: Thermohydrodynamic characteristics of two-phase flow in a heated capillary. *Int. J. of Multiphase Flow*, 26: pp. 1063–1093, 2000.
- [32] Hetsroni G., Segal Z. and Mosyak A.: Nonuniform temperature distribution in electronic devices cooled by flow in parallel microchannels. *Packaging of Electronic and Photonic Devices*, 28: pp. 1–9, 2000.
- [33] HNP Mikrosysteme GmbH: *Product Brochure - Micro Annular Gear Pumps*, April 2000.
- [34] Incropera F.P. and DeWitt D.P.: *Fundamentals of Heat and Mass Transfer*. John Wiley & Sons, 5th ed., 2002.
- [35] Jiang L., Wong M. and Zohar Y.: A micro-channel heat sink with integrated temperature sensors for phase transition study. In *Procs. of the IEEE Conference on Micro Electro Mechanical Systems (MEMS)*, pp. 159–164. 1999.
- [36] Jiang L., Wong M. and Zohar Y.: Phase change in microchannel heat sink under forced convection boiling. In *Procs. of the IEEE Conference on Micro Electro Mechanical Systems (MEMS)*, pp. 397–402. 2000.
- [37] Johnson R.W. (editor): *The Handbook of Fluid Dynamics*. CRC Press LLC, 1998.
- [38] Jungnickel H., Agsten R. and Kraus W.E.: *Grundlagen der Kältetechnik*. VEB Verlag Technik, Berlin, 1980.
- [39] Kaiser G. and Stangel R.: Miniaturisierte Kryoflüssigkeitspumpe. Tech. Rep. ILK-B-2/99-237, ILK Dresden, 1999.
- [40] Kakac S., Smirnov H. and Mila M. (editors): *Low Temperature and Cryogenic Refrigeration*, chap. Pulse Tube Cryocoolers. Kluwer Academic Publishers, Dordrecht, The Netherlands, 2003. To be published.
- [41] Kandlikar S.G.: Two-phase flow patterns, pressure drop and heat transfer during boiling in minichannel and microchannel flow passages of compact evaporators. In *Procs. of the Third Int. Conf. on Compact Heat Exchangers and Enhancement Technology for the Process Industries*. Davos, Switzerland, July 2001.

- [42] Kandlikar S.G., Shailesh J. and Shurong T.: Effect of surface roughness on heat transfer and fluid flow characteristics at low Reynolds numbers in small diameter tubes. *Heat Transfer Engineering*, 24 (3): pp. 4–16, 2003.
- [43] Kast W.: Druckverlust bei der Strömung durch Rohre. In *VDI Wärmeatlas*, chap. Lb1–Lb7. VDI Verlag, 6th ed., 1991.
- [44] Kienzle W. et al.: TOTEM: Total cross section, elastic scattering and diffraction dissociation at the LHC. Technical Proposal CERN/LHCC 99-7 LHCC/P5, CERN, 1999.
- [45] Kittel C.: *Introduction to Solid State Physics*. John Wiley & Sons, 7th ed., 1996.
- [46] Kleinert H.J. (editor): *Taschenbuch Maschinenbau*, vol. 5. VEB Verlag Technik, Berlin, 1st ed., 1989.
- [47] Lake Shore Cryotronics Inc.: *User's Manual Model 218 Temperature Monitor*, 1999.
- [48] Lake Shore Cryotronics Inc.: *User's Manual Model 331 Temperature Controller*, 2000.
- [49] Levenspiel O.: *Engineering Flow and Heat Exchange*. Plenum Press, New York, 1984.
- [50] Li Z. et al.: Electrical and transient current characterization of edgeless Si detectors diced with different methods. *IEEE Transactions on Nuclear Science*, 49 (3): pp. 1040–1046, June 2002.
- [51] Munkejord S.T. et al.: Micro technology in heat pumping systems. *AIRAH Journal*, pp. 28–31, April 2000.
- [52] Niinikoski T.O., Grohmann S. and Perea Solano B.: Conceptual design of a low-temperature radiation-hard tracker detector. In *International Symposium of Young Scholars on Mechanics and Material Engineering for Science and Experiments (ISM2E-YS)*. Changsha/Zhangjiajie, Hunan, China, August 2001.
- [53] Papula L.: Vektoranalysis, Wahrscheinlichkeitsrechnung, Mathematische Statistik, Fehler- und Ausgleichsrechnung. In *Mathematik für Ingenieure und Naturwissenschaftler*, vol. 3. Vieweg Verlag, 4th ed., 2001.
- [54] Peles Y.P. and Haber S.: A steady state, one dimensional, model for boiling two phase flow in triangular micro-channels. *Int. J. of Multiphase Flow*, 26: pp. 1095–1115, 2000.
- [55] Peles Y.P., Yarin L.P. and Hetsroni G.: Evaporating two-phase flow mechanism in micro-channels. In *Symposium on Design, Test and Microfabrication of MEMS and MOEMS*, vol. 3680, pp. 226–236. SPIE, Paris, France, March-April 1999.
- [56] Peng X.F., Hu H.Y. and Wang B.X.: Boiling nucleation during liquid flow in microchannels. *Int. J. of Heat Mass Transfer*, 41 (1): pp. 101–106, 1998.

- [57] Peng X.F. and Peterson G.P.: Convective heat transfer and flow friction of water flow in microchannel structures. *Int. J. of Heat Mass Transfer*, 39 (12): pp. 2599–2608, 1996.
- [58] Peng X.F., Peterson G.P. and Wang B.X.: Flow boiling of binary mixtures in microchanneled plates. *Int. J. of Heat Mass Transfer*, 39 (6): pp. 1257–1264, 1996.
- [59] Perea Solano B.: *Cryogenic Silicon Microstrip Detector Modules for the LHC*. Ph.D. thesis, Universitat Politècnica de Catalunya. Escola Tècnica Superior d'Enginyeria Industrial de Barcelona ETSEIB, 2004. To be published.
- [60] Perea Solano B., Grohmann S., Niinikoski T.O. and Vandoni G.: Thermo-elastic properties of fused quartz filled epoxies between 4.2 and 300 K. In *Procs. of the 19th International Cryogenic Engineering Conference (ICEC)*, pp. 705–708. Grenoble, France, July 2002.
- [61] Pettersen J.: *Flow Vaporization of CO₂ in Microchannel Tubes*. Ph.D. thesis, NTNU Trondheim, Norway, February 2002.
- [62] Pettersen J., Rieberer R. and Munkejord S.T.: Heat transfer and pressure drop for flow of supercritical CO₂ in microchannel tubes. Technical Report TR A5127, SINTEF Energy Research, 2000.
- [63] Pohlenz W. (editor): *Pumpen für Flüssigkeiten*. VEB Verlag Technik, Berlin, 4th ed., 1984.
- [64] Qu W., Mala G.M. and Li D.: Heat transfer for water flow in trapezoidal silicon microchannels. *Int. J. of Heat Mass Transfer*, 43: pp. 3925–3936, 2000.
- [65] Rahman M.M.: Measurements of heat transfer in microchannel heat sinks. *Int. J. of Heat Mass Transfer*, 27 (4): pp. 495–506, 2000.
- [66] Ravigururajan T.S.: Two-phase flow characteristics of refrigerant flows in a microchannel heat exchanger. *Enhanced Heat Transfer*, 6: pp. 419–427, 1999.
- [67] Rohde & Schwarz: *Manual Triple Power Supply NGPT 35*, 2000.
- [68] ROOT - An object-oriented data analysis framework. <http://root.cern.ch/>.
- [69] Sabry M.N.: Scale effects on fluid flow and heat transfer in microchannels. *IEEE Transactions on Components and Packaging Technologies*, 23 (3): pp. 562–567, September 2000.
- [70] Schumann B., Binneberg A. and Kaiser G.: Autarkes Kühleystem mit geschlossenem LN₂-Kreislauf. In *DKV-Tagungsbericht*, vol. 1, pp. 137–148. Deutscher Kälte- und Klimatechnischer Verein e.V., Bremen, 2000.
- [71] Shah R.K.: Compact heat exchanger surface selection methods. In *Procs. of the 6th Int. Heat Transfer Conference*, vol. 4, pp. 193–199. 1978.

- [72] Steiner D.: Zweiphasenströmung in Apparateelementen. Technical Report, Forschungs-Gesellschaft Verfahrens-Technik e.V., Düsseldorf, 1983.
- [73] Steiner D.: Wärmeübergang beim Sieden gesättigter Flüssigkeiten. In *VDI Wärmeatlas*, chap. Hbb1–Hbb35. VDI Verlag, 6th ed., 1991.
- [74] Storek H. and Brauer H.: Reibungsdruckverlust der adiabaten Gas/Flüssigkeits-Strömung in horizontalen und vertikalen Rohren. In *VDI Forschungsheft*, vol. 599/1980. VDI-Verlag, 1980.
- [75] Taitel Y. and Dukler A.E.: A model for predicting flow regime transitions in horizontal and near horizontal gas-liquid flow. *AIChE*, 22 (1): pp. 47–55, 1976.
- [76] Tso C.P. and Mahulikar S.P.: Experimental verification of the role of brinkman number in microchannels using local parameters. *Int. J. of Heat Mass Transfer*, 43: pp. 1837–1846, 2000.
- [77] VICI AG Valco International: *Valco Cheminert Catalog*, 2002.
- [78] Walker G. (editor): *Cryocoolers*. Plenum Press, New York, 1983.
- [79] Wang B.X. and Peng X.F.: Experimental investigation on liquid forced-convection heat transfer through microchannels. *Int. J. of Heat Mass Transfer*, 37: pp. 73–82, 1994.
- [80] Weisberg A. and Bau H.H.: Analysis of microchannels in integrated cooling. *Int. J. of Heat Mass Transfer*, 35 (10): pp. 2465–2474, 1992.
- [81] Weisend II J.G. (editor): *Handbook of Cryogenic Engineering*. Taylor & Francis, 1998.
- [82] Whalley P.B.: *Boiling, Condensation and Gas-Liquid Flow*. Oxford University Press, Oxford, New York, Tokyo, 1987.
- [83] Whalley P.B.: *Two-Phase Flow and Heat Transfer*. Oxford University Press, Oxford, New York, Tokyo, 1996.
- [84] Winterton R.H.S.: Where did the Dittus and Boelter equation come from? *Int. J. of Heat Mass Transfer*, 41 (4–5): pp. 809–810, 1998.
- [85] Yan Y. and Lin T.: Evaporation heat transfer and pressure drop of refrigerant R-134a in a small pipe. *Int. J. of Heat Mass Transfer*, 41: pp. 4183–4194, 1998.
- [86] Yu D., Warrington R., Barron R. and Ameel T.: An experimental investigation of fluid flow and heat transfer in microtubes. In *Procs. of the ASME/JSME Thermal Engineering Conference*, vol. 1, pp. 523–530. 1995.
- [87] Zhang L. et al.: Enhanced nucleate boiling in microchannels. In *Procs. of the IEEE Conference on Micro Electro Mechanical Systems (MEMS)*, pp. 89–92. 2002.

-
- [88] Zhao Y. et al.: Flow boiling of CO₂ in microchannels. *ASHRAE Transactions*, 106: pp. 437–445, 2000.